Results & Discussion

Chapter 4

4. Results & Discussion

4.1. Rationale behind the design of diphenylurea-amidine derivatives

ChEs inhibitors have emerged as a promising drug target for the treatment of AD. RIV is a well-known second-generation pseudocholinesterase inhibitor that can selectively cross the BBB and irreversibly inhibit BChE. RIV consists of a carbamate moiety and a basic amine side chain. Evidence from several studies shows that the carbamate fragment of RIV is the pharmacophore for ChE activity (145, 146). Several studies have reported that RIV (RIV) is a pseudo-irreversible and selectively potent inhibitor of BChE without addressing the key hallmarks of oxidative stress, Aβ and tau protein aggregation, and inflammation associated with the disease (145, 147, 148). RIV acts via carbomylation of the enzyme's active site serine residue. The covalent inhibitors suffer from several limitations (148). In AD, AChE, BChE, and aforesaid pathological hallmarks play a key role in the onset and progression of the disease. Therefore, multi-targeted ligands (MTDL) have been designed to achieve competitive inhibitors targeting not only BChE but also inhibiting AChE along with antioxidant effects, anti-Aβ aggregation, and tau protein aggregation modulation, and neuroprotective benefits.

Given the fact that the aromatic amino acid residues such as Tyr70, Tyr121, Trp279, Ser203, His447, and Glu334 play a key role in peripheral and catalytic sites of AChE. Interestingly, these features also play an important role in improving its affinity for the hydrophobic regions of Aβ.(149, 150) intriguingly, RIV lacks the balance of the aromatic hydrophobic features; thereof, we decided to replace the right-hand side carbamate amine functionality (Figure 1) of RIV with aromatic or substituted aromatic features to explore its dual role in ChEs inhibition and Aβ/tau aggregation modulation. Further, hydroxylamines (amidoximes) are well known for their antioxidant properties (151) so we replaced the left-

side amine functional group of RIV with amidoximes. It is also expected that this fragment will further balance hydrophobicity/hydrophilicity. The carbamate group of RIV was replaced with urea functionality, a stronger bond than carbamate, and less prone to attack by a serine residue. This replacement is expected to generate competitive inhibitors instead of covalent inhibitors. It is expected that this molecular design will lead to generating *in-vivo* efficacious multifunctional molecules with potent anti-ChE activity and improved antioxidant properties, able to modulate proteins ($A\beta_{1-42}$ and Tau) aggregation and inhibit NLRP3 inflammasome, thereby providing the neuroprotection in the disease. The development of potent cholinesterase (ChE) inhibitors commenced with the substituted aryl-urea pharmacophore as the foundational template. Our initial investigation focused on synthesizing and evaluating the enzyme inhibition properties of the unsubstituted aryl-urea derivative **3a-3w**. The study indicated that **3a-3w** significantly inhibited AChE and BChE.

Based on our previous observation of the well-tolerated behavior of indole and quinoline moiety toward AChE/BChE and their ability to provide multifunctional properties, we next aimed to introduce heterocyclic moieties (5-amino indolyl and 6-aminoquinolyl) to explore the role of substituents on binding interaction with the enzyme. As expected, compounds **6a**, with indolyl and **6b** carrying quinolyl ring, turned out to be potent inhibitors of the enzymes. Therefore, indole moiety was deemed a promising pharmacophore for developing potential AD agents. Building upon this rationale, we investigated the impact of linker length by introducing spacers between the urea functionality and indole moiety. To our advantage, compound **6e** bearing methoxy substitution showed the maximum enzyme inhibition activity among all the developed molecules.

Finally, we sought to investigate the impact of substituting the hydroxyamidine moiety from meta to para position in developed compounds concerning its influence on AChE/BChE activity. We selected a few lead compounds from the above-synthesized series

and rationally integrated these positional changes to investigate the impact on enzyme inhibition. Strikingly, none of the newly synthesized compounds displayed an enhanced AChE/BChE inhibitory efficacy (as indicated in Table 2) compared to the above-synthesized compounds (**3a-3w** and **6a-6e**).

In the present study, we built upon a SAR based on various substitutions connected to the phenyl ring and heterocyclic ring with a change in linker length on the right side, and we also investigated the positional changes of hydroxyamidine on the left side of the ring. Among the developed molecules, compounds **3q** and **6e** were the most potent against AChE and BChE inhibitory activity.

The lead molecules inhibited the NLRP3 inflammasome, suggesting they could effectively treat various inflammasome-related diseases such as AD. Therefore, targeting the NLRP3 inflammasome using these novel compounds further supports another avenue to develop neuroprotective molecules for AD management (159).

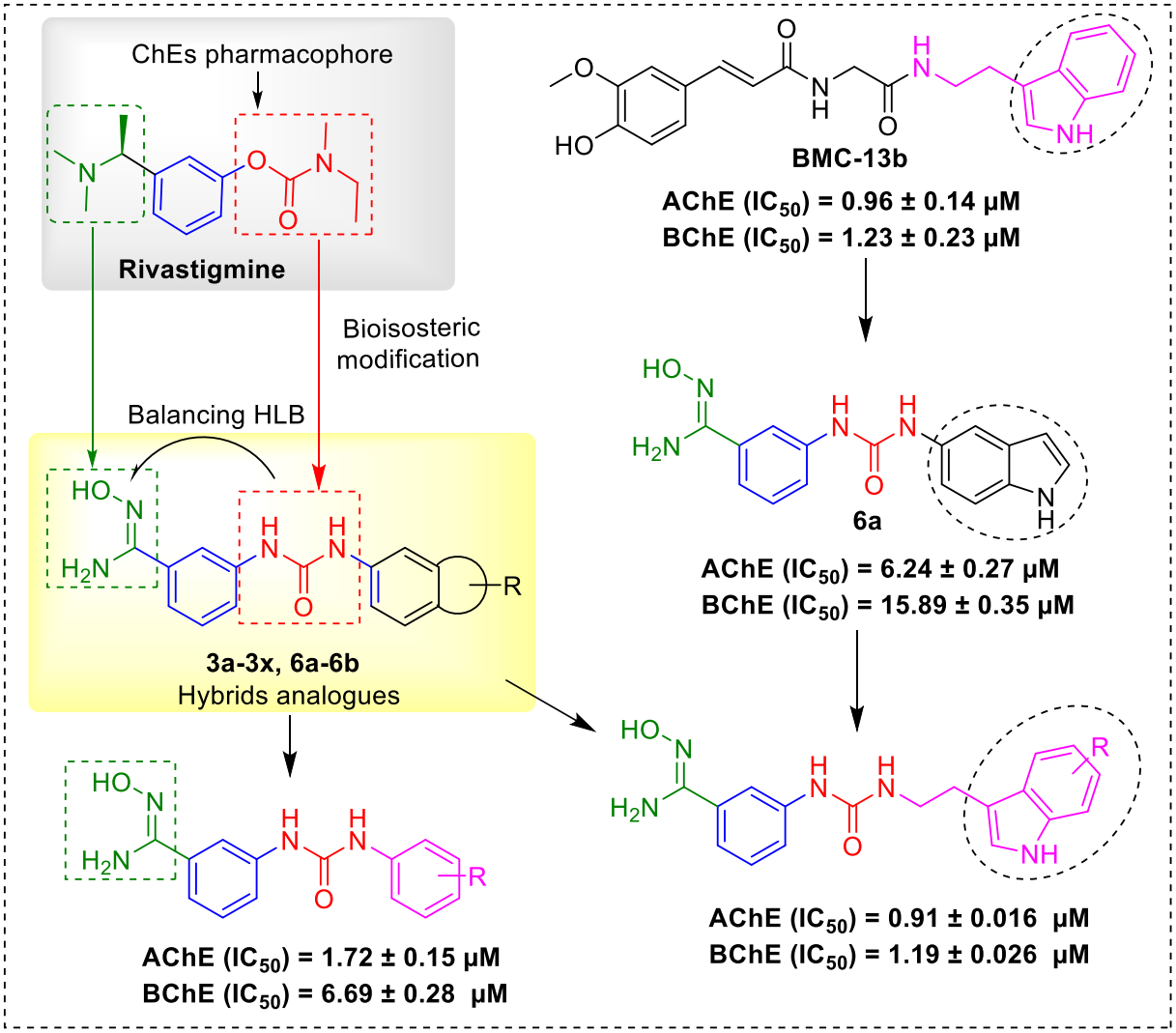

Figure 4.1: Design approach towards synthesizing diarylurea-hydroxyamidine derivatives as potential anti-AD agents.

4.2. Chemistry and synthetic schemes involved in the first series of diphenylurea-amidine derivatives

The synthetic routes for the designed compounds **3a-3w** and **6a-6b** are shown in Schemes **1** and **2**. In Scheme **1** and **2,** commercially available 3-cyanophenylisocynate was reacted with substituted aniline (**1a-1w)**, 5-amino indole or 6-aminoquinoline), using pyridine as a base in DCM to generate respective urea analogs (**2a-2w** and **5a-5b**). In the final step, reactive nitrile species underwent a nucleophilic addition reaction with hydroxylamine hydrochloride in the presence of a base in ethanol. In schemes **3** and **4,** commercially available 4-cyanophenylisocynate was reacted with substituted anilines (**8a-8e)**, 5-amino

indole, or 6-aminoquinoline), using pyridine to generate respective urea analogs (**9a**-**9e,** and **11a**-**11b**). In the final step, reactive nitrile species underwent a nucleophilic addition reaction with hydroxylamine hydrochloride in the presence of DIPEA in ethanol. All compounds were purified by column chromatography. These target compounds have not previously been reported in the literature. Structural elucidations of all compounds were done using ^{1}H, ^{13}C NMR, and HRMS.

Scheme 1. Synthesis of diphenylurea-amidine derivatives **3a**-**3w**

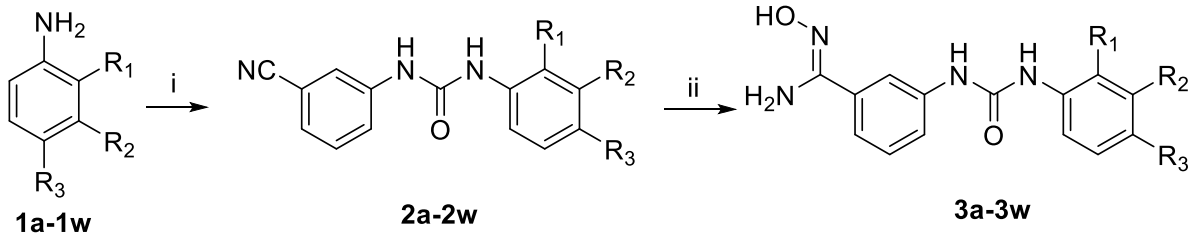

3a: R_1 = H, R_2 = H, R_3 = H,
3b: R_1 = CH_3, R_2 = H, R_3 = H,
3c: R_1 = H, R_2 = CH_3, R_3 = H,
3d: R_1 = H, R_2 = H, R_3 = CH_3
3e: R_1 = OCH_3, R_2 = H, R_3 = H,
3f: R_1 = H, R_2 = OCH_3, R_3 = H,
3g: R_1 = H, R_2 = H, R_3 = OCH_3,
3h: R_1 = H, R_2 = OH, R_3 = H,
3i: R_1 = H, R_2 = H, R_3 = OH,
3j: R_1 = Cl, R_2 = H, R_3 = H,
3k: R_1 = H, R_2 = Cl, R_3 = H,
3l: R_1 = H, R_2 = H, R_3 = Cl,
3m: R_1 = Br, R_2 = H, R_3 = H,
3n: R_1 = H, R_2 = Br, R_3 = H,
3o: R_1 = H, R_2 = H, R_3 = Br,
3p: R_1 = F, R_2 = H, R_3 = H
3q: R_1 = H, R_2 = F , R_3 = H,
3r: R_1 = H, R_2 = H, R_3 = F,
3s: R_1 = CF_3, R_2 = H, R_3 = H,
3t: R_1 = H, R_2 = CF_3, R_3 = H,
3u: R_1 = H, R_2 = H, R_3 = CF_3,
3v: R_1= H, R_2= NO_2, R_3= H,
3w: R_1= H, R_2= H, R_3= NO_2,

Reagents and conditions: (i) 3-(cyanophenyl)isocyanate, pyridine, DCM, rt, 2h, 75-85%; (ii) Hydroxylamine hydrochloride, DIPEA, Ethanol, 12h, 70-80%.

Scheme 2. Synthetic route for compounds **6a**-**6e**

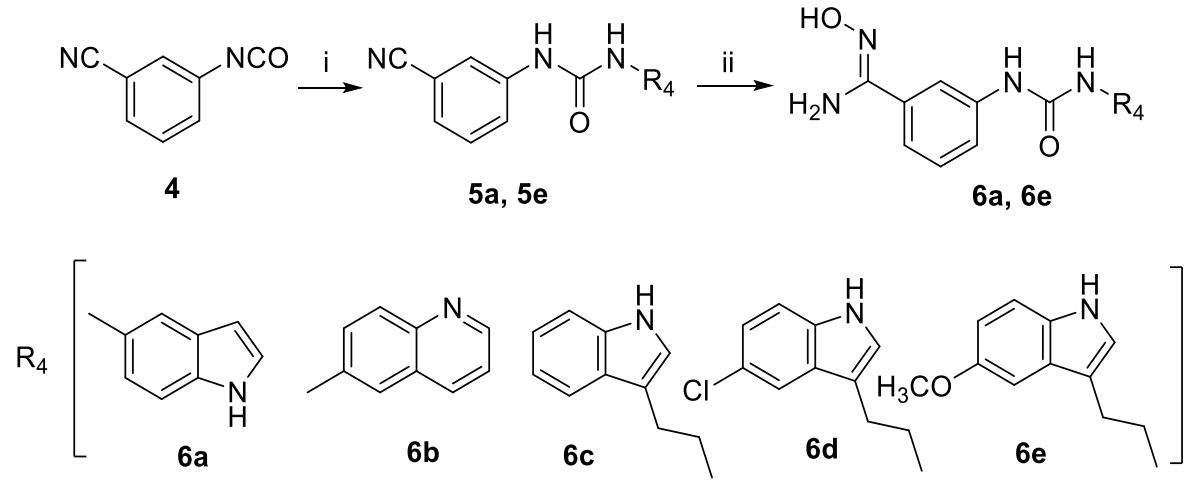

Reagents and conditions: (i) 5-aminoindole/6-aminoquinoline, pyridine, DCM, rt, 2h, 75-85%; (ii) Hydroxylamine hydrochloride, DIPEA, Ethanol, 12h, 70-80%.

Scheme 3. Synthesis of diarylurea-hydroxyamidine derivatives **9a**-**9e**.

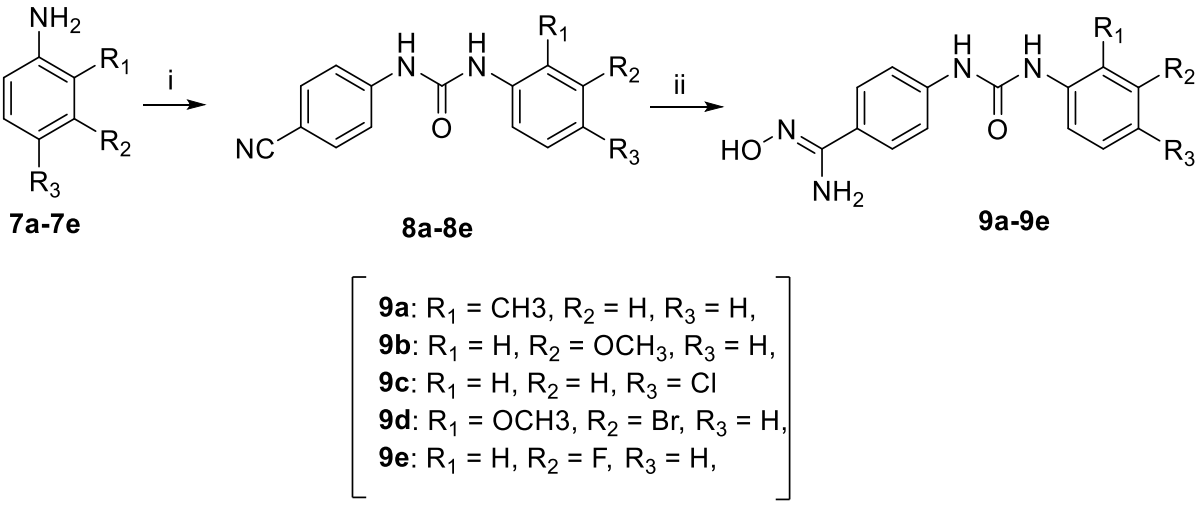

9a: R_1 = CH3, R_2 = H, R_3 = H,
9b: R_1 = H, R_2 = OCH_3, R_3 = H,
9c: R_1 = H, R_2 = H, R_3 = Cl
9d: R_1 = OCH3, R_2 = Br, R_3 = H,
9e: R_1 = H, R_2 = F, R_3 = H,

Reagents and conditions: (i) 4-(cyanophenyl)isocyanate, pyridine, DCM, rt, 2h, 75-85%; (ii) Hydroxylamine hydrochloride, DIPEA, Ethanol, 12h, 70-80%.

Scheme 4. Synthetic route of compounds **11a**-**11b**.

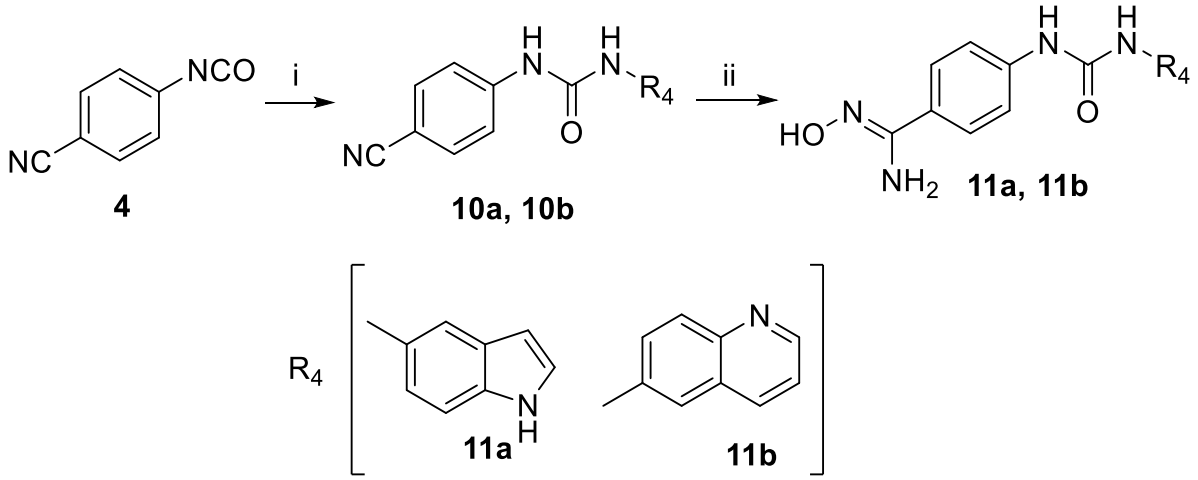

Reagents and conditions: (i) 5-aminoindole/6-aminoquinoline, pyridine, DCM, rt, 2h, 75-85%; (ii) Hydroxylamine hydrochloride, DIPEA, Ethanol, 12h, 70-75% yields.

4.3. Biological evaluation of the first series of diphenylurea-amidine derivatives

4.3.1. SAR studies of synthesized molecules against *h*AChE, *eq*BChE, hBChE

In clinical practice, it is evident from the literature that ChE inhibitors are current therapeutic strategies for improving learning memory and slowing down cognitive decline in individuals afflicted with AD.(160) Thus, inhibition of ChEs to enhance ACh is essential for AD treatment. Therefore, the Ellman spectrophotometric method evaluated the ChE inhibitory activities of the target compounds using AChE from human erythrocytes and BChE from equine serum or humans (161). DPZ and RIV were used as positive reference standards. The assay results were presented as IC_{50} (μM), i.e., the inhibitor concentration, which reduces the ChE inhibitory activity by 50%. The tested compounds displayed poor to excellent AChE/ BChE inhibitory activities (**Table 1**).

The diarylurea-hydroxyamidine pharmacophore served as the starting template for developing potent ChE inhibitors. Our investigation commenced with synthesizing and assessing the enzyme inhibition properties of the phenyl urea derivative **3a**. The enzyme inhibition study revealed that **3a** demonstrated a moderate inhibitory effect on BChE (IC_{50}, BChE = 17.50 µM), and exhibited a diminished inhibitory activity against AChE (IC_{50}, AChE

> 20 µM). Next, we introduced a methyl group onto the phenyl ring of our primary compound **3a** to investigate the impact of small electron-donating groups (EDGs) at *o*-CH_3, *m*-CH_3, and *p*-CH_3 positions, resulting in the generation of compounds **3b-3d**. Intriguingly, compound **3b**, featuring *o*-CH_3 on the phenyl ring, exhibited the most substantial inhibition of AChE compared to **3c** and **3d** (IC_{50}, AChE = 17.35 for **3b**, and >20 for **3c** and **3d**, respectively). Meanwhile, **3c**, with *m*-CH_3 on the phenyl ring, demonstrated the highest BChE inhibition among **3b** and **3d** (IC_{50}, BChE = 15.39; 10.55; 17.89 for **3b-3d**, respectively). We introduced electron-donating groups (o-CH_3, m-OCH_3, p-OCH_3, m-OH, and p-OH) onto the phenyl ring, synthesizing **3e-3i**. Intriguingly, compounds **3f,** and **3h** exhibited the highest ChE inhibition among all analogs with electron-donating groups (IC_{50}, AChE = 3e >20, **3f** = 12.91, **3g** = 16.34, **3h** = 14.51, and **3i** = 16.27; IC_{50}, BChE = **3e** = 15.21, **3f** = 12.85, **3g** = 17.95, **3h** = 15.53, and **3i** = 14.36, respectively). Additionally, it was noted that electron-donating groups at the m-position of the phenyl ring were well-tolerated at the AChE site.

Following the optimization of electron-donating groups, we proceeded to introduce various electron-withdrawing groups (EWG) onto the phenyl ring to investigate the impact of *o*-Cl, *m*-Cl, *p*-Cl, *o*-Br, *m*-Br, and *p*-Br substituents, resulting in the synthesis of compounds **3j-3o**. In the enzyme inhibition study, compounds **3l** and **3n**, featuring p-Cl and m-Br on the phenyl ring, respectively, exhibited the maximum inhibition for AChE among all analogs with electron-withdrawing groups (IC_{50}, AChE = **3j** >20, **3k** = 17.41, **3l** = 14.10, **3m** >20, **3n** = 14.53, **3o** = 16.80; IC_{50}, BChE = **3j** = 15.37, **3k** = 18.75, **3l** = 16.49, **3m** >20, **3n** = 8.63, **3o** = 14.56, respectively). Based on these results, we further introduced a few more EWGs to phenyl ring *o*-F, *m*-F, *p*-F, *o*-CF_3, *m*-CF_3, *p*-CF_3, *m*-NO_2, and *p*-NO_2 groups, resulting in the synthesis of compounds **3p-3w**. In the enzymes inhibition studies, **3q** and **3r** bearing *m*-F, *p*-F having strong EWG showed maximum enzyme inhibition (IC_{50}, AChE (μM), **3p** = 18.58, **3q**

= 1.72, **3r** = 7.51, **3s** = 18.26, **3t** = 17.01, **3u** = 12.22, **3v** = 12.15, **3w** = 16.31; IC_{50}, BChE (μM), **3p** = 11.28, **3q** = 6.69, **3r** = 17.74, **3s** = 17.12, **3t** = 10.52, **3u** = >20, **3v** = 16.34, **3w** = 17.65, respectively).

Based on our previous observation of well-tolerated behavior of indole, quinoline, and tryptamine properties toward AChE/BChE and their ability to provide multifunctional properties, we next aimed to introduce heterocyclic moieties (5-amino indolyl and 6-aminoquinolyl) to explore the role of these substituents on binding interaction with the enzyme.(162, 163) As expected, **6a**, with indolyl and **6b** carrying quinolyl ring, turned out to be potent inhibitors (IC_{50}, AChE (μM), 6.24, 5.68 μM; IC_{50}, BChE (μM), 15.89, 15.42 μM, for **6a** and **6b,** respectively.

Finally, we sought to investigate the impact of substituting the hydroxyamidine moiety from *meta* to *para* position in our above-documented compound concerning its influence on AChE/BChE activity. We selected a few lead compounds from the above-reported series and integrated these positional changes to investigate the impact on enzyme inhibition. We deliberately and discerningly produced eight compounds (**9a-9e** and **11a-11b**) as an integral facet of our systematic structure-activity relationship (SAR) investigation. Strikingly, none of the newly synthesized compounds displayed an enhanced AChE/BChE inhibitory efficacy (as indicated in Table 2) compared to the above-reported compounds (**3a-3w** and **6a-6e**).

In the next series, substituted tryptamine fragments were introduced, which led to the generation of **6c-6e**. To our advantage, compound **6e** bearing methoxy substitution showed the maximum enzyme inhibition (IC_{50}, AChE (μM) = 0.91; IC_{50}, BChE, 1.19 µM) respectively among all the developed molecules. In the present study, we built upon a SAR based on various substitutions connected to the phenyl ring (Figure 2). Among the designed

molecules, compounds **3q** and **6e** were found to be the most potent against AChE and BChE inhibitory activity.

Table 1. Cholinesterase inhibitory activities of the target compounds.

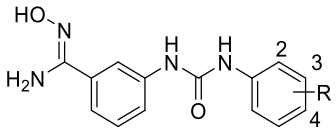

3a-3x

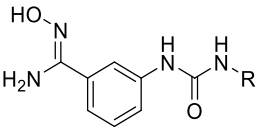

6a, 6b

Compound	**R**	**% inhibition[a]/IC_{50} (μM)[b]**		
		***h*AChE**	***eq*BChE**	***h*BChE**
3a	Hydrogen	47.91 ± 0.43%	17.50 ± 0.54	n.d.
3b	2-methyl	17.35 ± 0.77	15.39 ± 0.47	n.d.
3c	3-methyl	42.53 ± 0.22%	10.55 ± 0.39	n.d.
3d	4-methyl	39.87 ± 0.17%	17.89 ± 0.48	n.d.
3e	2-methoxy	48.95 ± 0.93%	15.21 ± 0.44	n.d.
3f	3-methoxy	12.91 ± 0.43	12.85 ± 0.43	n.d.
3g	4-methoxy	16.34 ± 0.03	17.95 ± 0.14	n.d.
3h	3-hydroxy	14.51 ± 0.45	15.53 ± 0.45	n.d.
3i	4-hydroxy	16.27 ± 0.78	14.36 ± 0.55	n.d.
3p	2-fluoro	18.58 ± 0.52	11.28 ± 0.42	n.d.
3q	3-fluoro	1.72 ± 0.15	6.69 ± 0.28	5.21 ± 0.14
3r	4-fluoro	7.51 ± 0.27	17.74 ± 0.54	n.d.
3j	2-chloro	49.23 ± 0.70%	15.37 ± 0.35	n.d.
3k	3-chloro	17.41 ± 0.54	18.75 ± 0.61	n.d.
3l	4-chloro	14.10 ± 0.34	16.49 ± 0.23	n.d.
3m	2-bromo	47.67 ± 0.65%	49.21 ± 0.25%	n.d.

3n	3-bromo	14.53 ± 0.33	8.63 ± 0.30	n.d.
3o	4-bromo	16.80 ± 0.41	14.56 ± 0.21	n.d.
3s	2-trifluoromethyl	18.26 ± 0.48	17.12 ± 0.57	n.d.
3t	3-trifluoromethyl	17.01 ± 0.54	10.52 ± 0.40	n.d.
3u	4-trifluoromethyl	12.22 ± 0.31	46.98 ± 0.81%	n.d.
3v	3-nitro	12.15 ± 0.04	16.34 ± 0.51	n.d.
3w	4-nitro	16.31 0.48	17.65 ± 0.52	n.d.
6a	5-indolyl	6.24 ± 0.27	15.89 ± 0.35	n.d.
6b	6-quinolinyl	5.68 ± 0.25	15.42 ± 0.39	n.d.
6c	Tryptamine	1.54 ± 0.038	3.91 ± 0.057	n.d.
6d	5-Cl-tryptamine	1.16 ± 0.043	3.1 ± 0.032	n.d.
6e	5-methoxytryptamine	0.91 ± 0.016	1.19 ± 0.026	1.01 ± 0.10
RIV[c]	-----	6.63 ± 0.76	0.091 ± 0.40	n.d.
DPZ[d]	-----	0.03 ± 0.007	2.89 ± 0.02	n.d.

Table 2. Cholinesterase inhibitory activities of the target compounds.

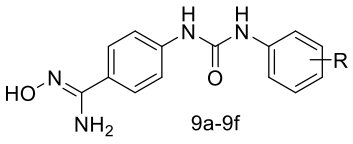

9a-9f

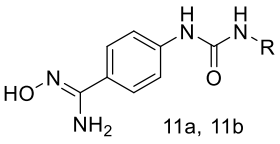

11a, 11b

Compound	**R**	**% inhibition**[a]**/IC$_{50}$ (μM)**[b]	
		***h*AChE**	***eq*BChE**
9a	2-methyl	8.57 ± 0.39	16.87 ± 0.44
9b	3-methoxy	9.15 ± 0.38	18.23 ± 0.58
9c	4-chloro	7.65 ± 0.31	14.63 ± 0.63
9d	3-fluoro	3.04 ± 0.14	8.08 ± 0.18

9e	3-bromo	6.41 ± 0.16	7.62 ± 0.26
11a	5-indolyl	7.47 ± 0.34	12.67 ± 0.38
11b	6-quinolyl	6.94 ± 0.23	13.21 ± 0.35

[a]Inhibition was assessed using a 20 μM inhibitor concentration, and the experiments were performed three times to ensure accuracy.

[b]The IC_{50} value represents the inhibitor concentration that causes 50% inhibition of the target activity. The IC_{50} value was determined by averaging the results from two to three independent experiments, and the standard deviation (SD) was calculated to measure the variability.

[c,d] RIV and DPZ were positive controls in the experiment.

4.3.2. Kinetic studies of *h*AChE and *eq*BChE inhibition

Compounds **3q** and **6e** were identified as the lead molecules based on the findings from ChE inhibition studies. Subsequently, the kinetics of their inhibitory effects on AChE and BChE were investigated. This study employed three pre-determined concentrations of **3q** and **6e** inhibitors (0.1, 1, and 5 μM) against AChE, while 1, 5, and 10 μM were used against BChE. Substrate hydrolysis velocity (V) was evaluated for each concentration at five distinct substrate concentrations (ranging from 2.5 to 0.5 mM). The inhibitory impacts of **3q** and **6e** were graphically represented in **Figure 4.2**, using Lineweaver-Burk reciprocal plots. These graphical representations unveiled that **3q** and **6e** exhibited a mixed type of inhibition pattern against *h*AChE while demonstrating competitive inhibition against *eq*BChE (162).

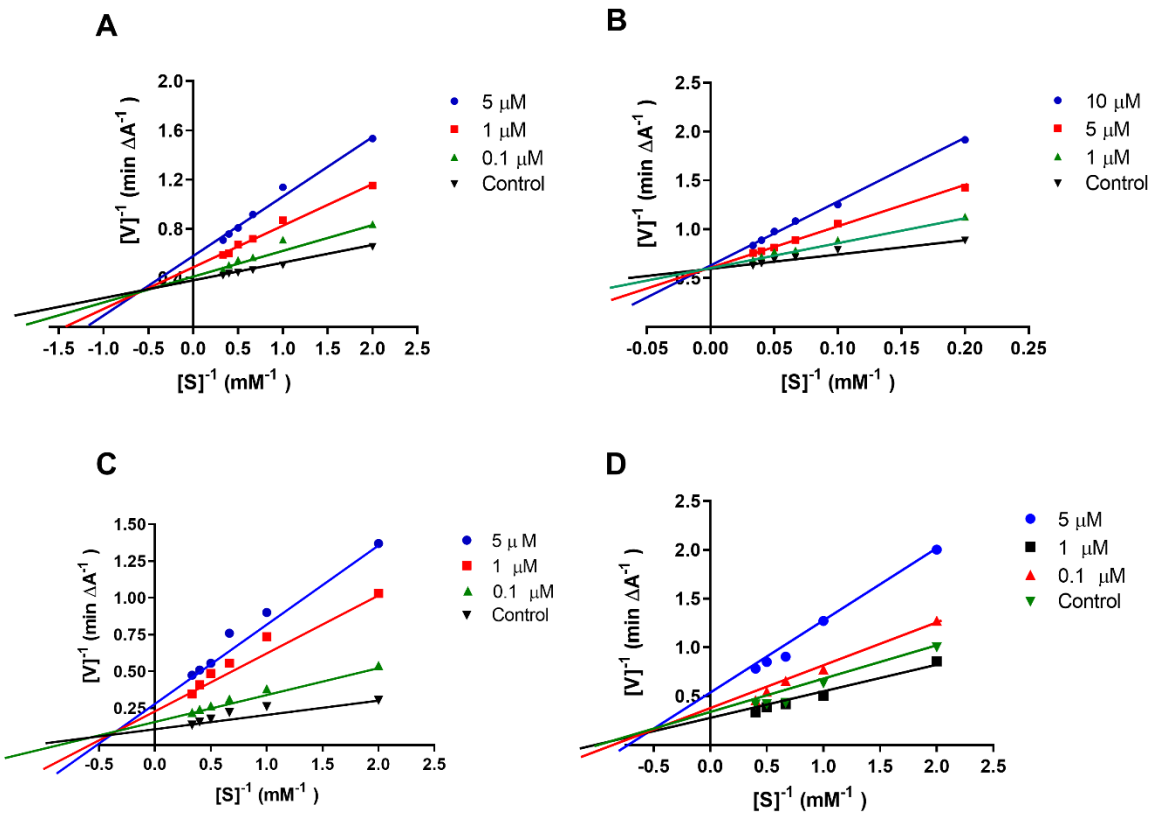

Figure 4.2: Lineweaver-Burk plots illustrate *h*AChE and *eq*BChE hydrolytic activity over a range of substrate concentrations and in the presence of different concentrations of inhibitor **3q** (**A** and **B**), and **6e** (**C** and **D**). [S] = concentration of acetylthiocholine or butyrylthiocholine; [Vmax] = velocity rate. The experimental data are the average values with standard deviation (SD) calculated from two independent experiments.

4.3.3. Quantification of propidium iodide displacement from the peripheral anionic site of AChE

In the given context, the AChE enzyme has a binding affinity for propidium iodide (PI), specifically within the PAS region, which is expected to modulate Aβ aggregation. In this situation, a particular inhibitor of the enzyme competes with PI to replace it from its binding site. (162) A decrease in the fluorescence intensity of PI is a strong measure of the competitive binding of the inhibitor at the PAS site.(164) As shown in **Table 3**, at a concentration of 50 µM, **3q,** and **6e** caused propidium iodide displacement of 16.64% and

27.53%, respectively. In comparison, **RIV** exhibited a displacement of 9.56% at the same concentration, while DPZ demonstrated a displacement of 30.88%.

Table 3. Displacement of Propidium Iodide from the PAS of *h*AChE by **3q, 6e, DPZ,** and **RIV**.

Compound	**Concentrations**			
	5 μM (%)	10 μM (%)	20 μM (%)	50 μM (%)
3q	0.23 ± 0.04	2.25 ± 0.31	4.71 ± 0.35	16.64 ± 0.17
6e	2.06 ± 0.06	11.78 ± 2.17	14.47 ± 0.16	27.53 ± 0.19
[b]DPZ	10.14 ± 0.14	13.95 ± 0.25	21.65 ± 0.28	30.88 ± 0.33
[c]RIV	0.18 ± 0.03	2.72 ± 0.10	5.34 ± 0.12	9.56 ± 0.18

The experimental data are the average values with standard deviation (SD) calculated from two independent experiments.

[b]DPZ = Donepezil.

[c]RIV = RIV.

4.3.4. Molecular docking and dynamic study of 3q and 6e

Molecular docking was performed using Glide, with the coordinates of the cocrystallized ligands (DPZ for AChE and Tacrine for BChE) being taken as the center of the grid box. Interactions that were present for the known drugs **RIV** and **DPZ** were taken as the reference interactions. The co-crystallized molecules were re-docked to check the confirmation of the docking protocol.

4.3.4.1. Exploring the binding of 3q and 6e with *h*AChE

Table 4. Docking score and interactions of the ligands with AChE

Sl. No.	Ligand	Docking Score (kcal/mol)	Interactions	Distance (Å)
1.	**6e**	-9.169	Ser293(H bond)	2.07
			Arg296 (H bond)	1.75
			Trp286 (π-π)	3.99
			Trp86 (π-π)	4.03
			Trp86 (π-π)	3.96
2.	**3q**	-8.904	Trp286 (π-π)	3.64
			Ser293 (H bond)	2.04
			Ser293 (H bond)	1.69
			Phe338 (π-π)	3.86
			Tyr124 (H bond)	1.93
3.	**RIV**	-7.947	Tyr337 (π-π)	5.17
			Phe338 (π-π)	4.09
			Phe295 (H bond)	2.06
			Asp74 (salt bridge)	4.56
			Trp86 (π-cation)	5.01
4.	**DPZ**	-	Trp286 (π-π)	3.9
			Trp86 (π-π)	4
			Trp86 (π-cation)	4.79
			Tyr337 (π-cation)	5.17
			Phe338 (π-cation)	3.86
			Phe295 (H bond)	2.05

Molecule **6e** had the best docking score of -9.17 kcal/mol **(Table 4),** followed by **3q** (docking score of -8.90 kcal/mol) and RIV (docking score of -7.95 kcal/mol). When docked into the same cavity, the co-crystallized ligand showed a docking score of -13.03 kcal/mol

and a rmsd value of 0.93 Å compared to its crystal conformation. **DPZ** showed π-π stacking interactions with Trp86 and Trp286, residues being part of the anionic subsite and the peripheral anionic site in the entry of the active site gorge, respectively. Π-cation interactions were present for the residues Tyr337 and Phe338, members of the anionic subsite. Hydrogen bonding interactions were also present between **DPZ** and the acyl pocket residue Phe295. RIV shows π-π stacking interactions with the anionic site residues Tyr337 and Phe338. The positively charged amino group interacts with the residue Trp86 via π-cation interactions and the peripheral anionic site residue Asp74 via salt bridge interactions. The molecule **6e** showed π-π interactions with Trp86 and Trp286, signifying its ability to modulate both the peripheral and anionic sites. However, hydrogen bonding was observed with the residues Ser293 and Arg296. Similarly, with molecule **3q**, Trp286 and Phe338 exhibited π-π stacking and hydrogen bonding interactions with Ser293. From these interactions, it can be seen that, like the approved drugs **DPZ** and **RIV**, the new molecules **3q** and **6e** also interact with the different sites near the active site cavity.

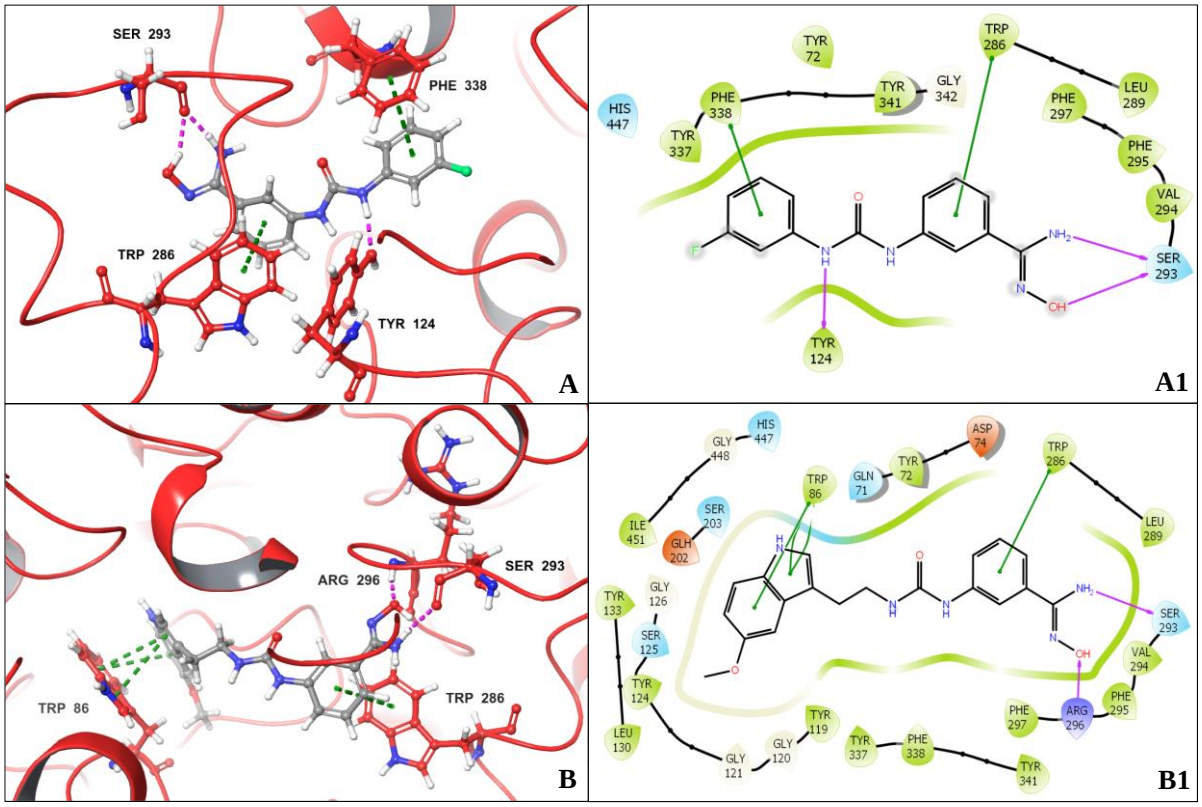

Figure 4.3: 3D docking poses of AChE with (A) **3q** (B) **6e**, and 2D interaction of AChE with (A1) **3q** (B1) **6e** where green-, red- and violet-colored arrows represent the π–π stacking, π – cation interactions and hydrogen bonds, respectively.

4.3.4.2. Exploring the binding of 3q and 6e with BChE

Table 5. Docking score and interactions of the ligands with BChE

Sl. No.	Ligands	Docking Score (kcal/mol)	Interactions	Distance (Å)
1.	**6e**	-7.005	Trp82 (π-π)	4.16
			Trp82 (π-π)	4.29
			Hip438 (H bond)	2.01
			Ser287 (H bond)	2.00
2.	**3q**	-6.489	Asn83 (H bond)	1.87
			Hip438 (H bond)	2.13
3.	**RIV**	-5.182	Asp70 (salt bridge)	3.88
4.	**Tacrine**	-	Trp82 (π-π),	3.61

			Trp82 (π-cation),	4.22
			Hip438 (H bond)	2.02

6e had the best docking score of -7.00 kcal/mol (**Table 5**), followed by **3q** (docking score of -6.49 kcal/mol) and RIV (docking score of -5.18 kcal/mol). When docked in the same cavity, the cocrystallized ligand, tacrine showed a docking score of -6.99 kcal/mol and an rmsd of 1.88 Å compared to its crystal conformation. This low docking score can be attributed to tacrine having a much more rigid structure than the other ligands. The Trp82 residue of BChE formed π-cation and π-π stacking interactions with tacrine, and also, the Hip438 formed hydrogen bonds. The Trp82 interactions were only observed in the *h*BChE-**6e** complex, but the Hip438 hydrogen bonding interactions were observed in the case of both **3q** and **6e**. Hydrogen bonding interactions were present between Ser287 and **6e** and Asn83 and **3q**. Only π-cation interactions were observed in the case of RIV with residue Asn70.

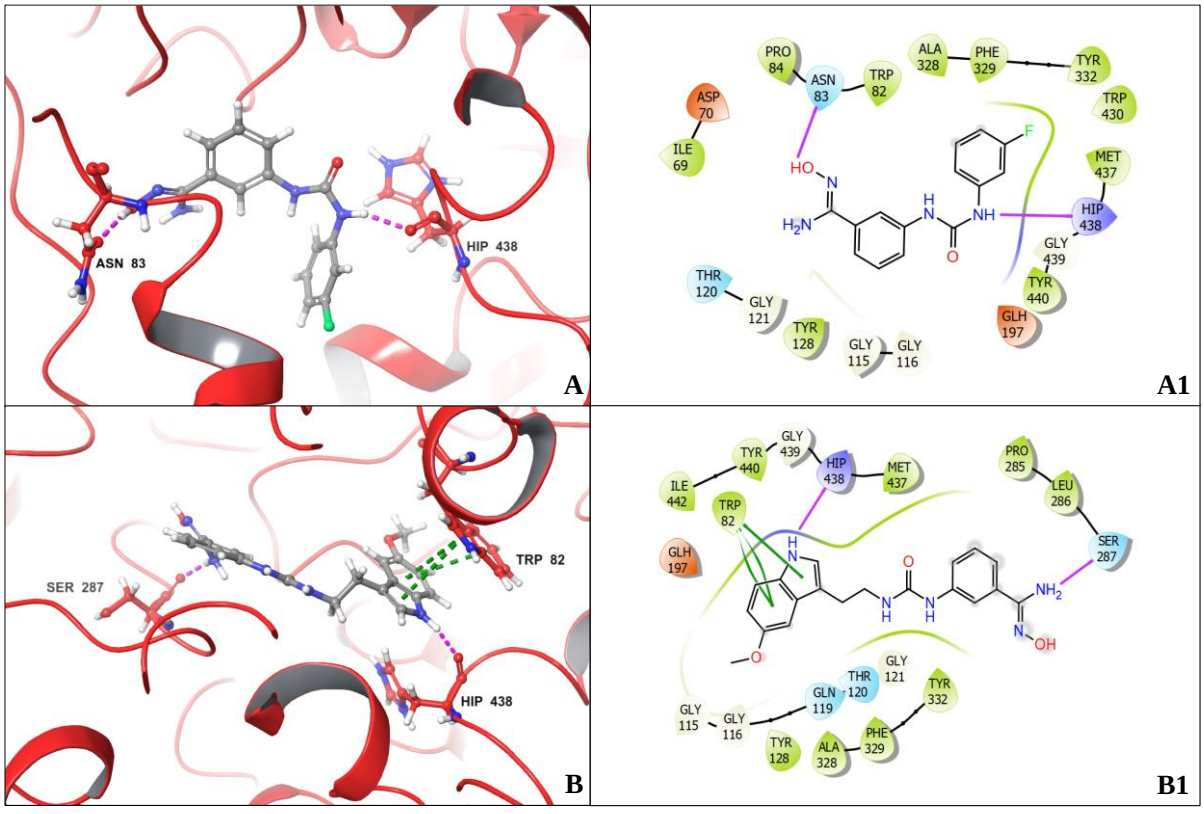

Figure 4.4: 3D docking poses of BChE with (A) **3q** (B) **6e** and 2D interaction diagram of

BChE with (A1) **3q** (B1) **6e** where green-, red- and violet-colored arrows represent the π-π stacking, π-cation interactions, and hydrogen bonds, respectively.

4.3.5. Molecular dynamics simulation

4.3.5.1. Interaction of 3q, and 6e with AChE

The interactions taking place throughout the entire simulation can be identified. The Trp286 residue interacts for 44% of the simulation time with cocrystallized DPZ via π-π interactions. It also forms hydrogen bonds with residues Phe295 and Arg296 for 91% and 36% of the simulation time. Asp74 and Tyr337 formed a salt bridge and π-cation interaction with the positively charged nitrogen of the piperidine moiety for 53% and 67% of the simulation times, respectively. The anionic subsite Trp86 interacts with the benzyl group of the **DPZ** via hydrophobic interactions. The hydrogen bonding interaction was also present for **RIV** for 84% of the simulation time. Of the other significant interactions of **RIV**, the positively charged dimethyl amino group formed π-π interaction with Trp86 and hydrogen bonding interactions with Tyr124 for 64% and 74% of the interaction time. The active site residue His447 forms hydrogen bonds with the nitrogen of the indole of the tryptamine with ligand **6e**. This interaction is significant as none of the other ligands showed this directly interacting with a catalytic triad residue. In the AChE-**6e** complex, the known π-π stacking interactions were also there for Trp86. Hydrogen bonding interactions were also seen for Gly120, Tyr124, Tyr133, Arg296 and Tyr337. For **3q** as a ligand, Trp286 and the acyl pocket residue Phe297 show π-π stacking interactions. Other hydrogen bonding interactions were with Tyr124 and Ser293 residues. Residues Phe295 and Arg296 interact via the formation of water bridges.

The average energy of the AChE-**6e** complex was the lowest (-82.01 ± 20.68 kcal/mol) for the entire simulation. The average energy of the known inhibitor **RIV** (-66.40 ±

4.31 kcal/mol) was more favorable in comparison to that of molecule **3q** (-58.49 ± 8.70 kcal/mol), but both of these were more than cocrystallized **DPZ** (-80.08 ± 6.42 kcal/mol).

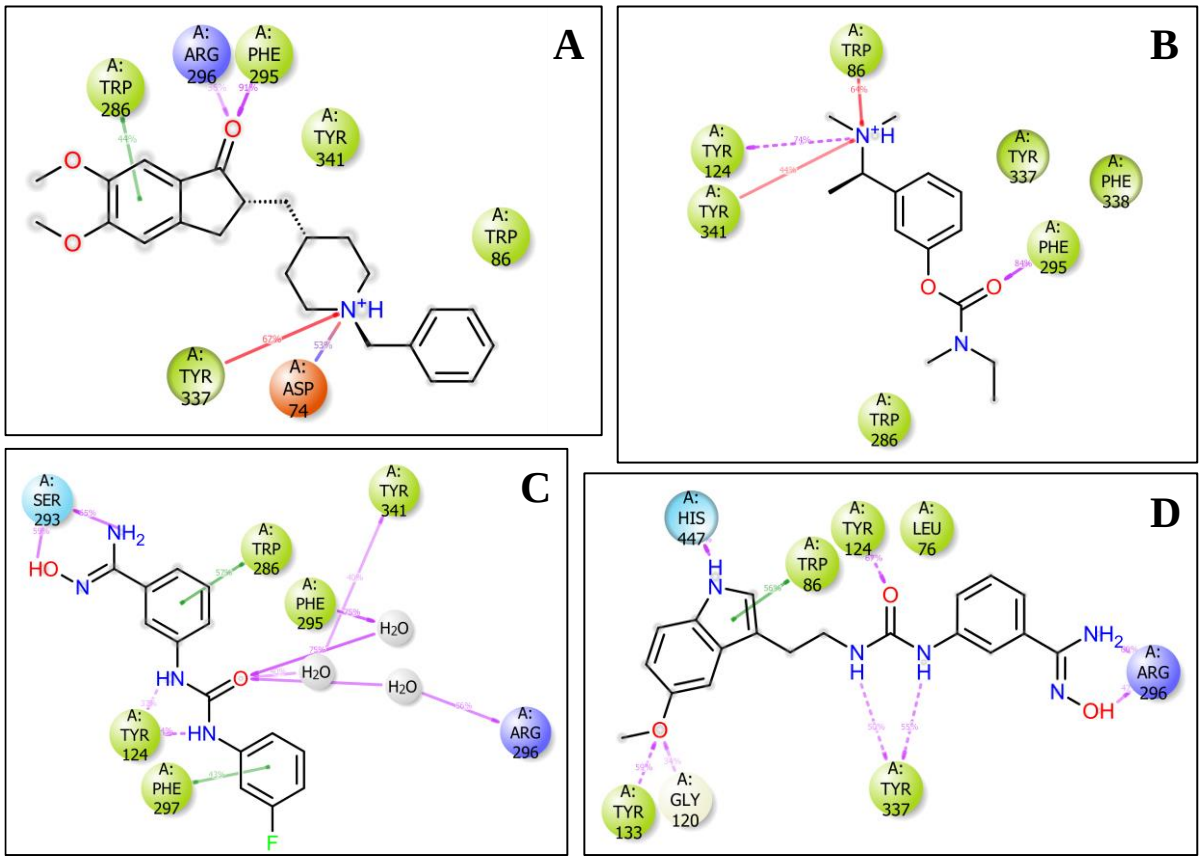

Figure 4.5: AChE-ligand interaction diagrams for the 300 ns simulation with (A) **DPZ**, (B) **RIV**, (C) **3q**, and (D) **6e** showing interaction time percentages with the residues.

4.3.5.2. Interaction of 3q and 6e with BChE

All the interactions occurring between the BChE and the ligands can be identified. The Trp82 residue of BChE interacts with both the rings of the benzopyridine of tacrine for 54% and 45% of the simulation time via π-π stacking interactions. The Trp82 forms π-cation interactions with the nitrogen of the benzopyridine for 93% of the simulation. The His438 (in Hip state) forms hydrogen bonds with the same nitrogen for the entire length of the simulation. The amine group forms 2 water bridges with the Asp70 residue for 47% and 37 % of the simulation time. The Trp82 residue interacts with all the ligands. It forms π-π stacking interactions with **3q** for 65% of the simulation time. With **RIV**, the Tyr332 residue forms π-

cation interactions for 59% of the simulation time. The Asn68 residue forms H-bonding interactions and water bridges with **3q**. For the ligand **3q**, Thr120 and Trp82 form hydrogen bonds and water bridges for a small simulation time. **6e** showed hydrogen bonding interactions with the residue Leu286.

The average energy of the cocrystallized ligand complex, tacrine with BChE, was the lowest (-53.45 ± 2.32 kcal/mol). The MM-GBSA energy of the BChE-**RIV** complex was -43.79 ± 6.45 kcal/mol. The average energy of the BChE-**6e** and BChE-**3q** complexes were nearly the same, i.e., -47.04 ± 7.02 kcal/mol and -48.01 ± 4.91 kcal/mol, respectively. The energies were stable for the entire simulation and only a few minor fluctuations were observed.

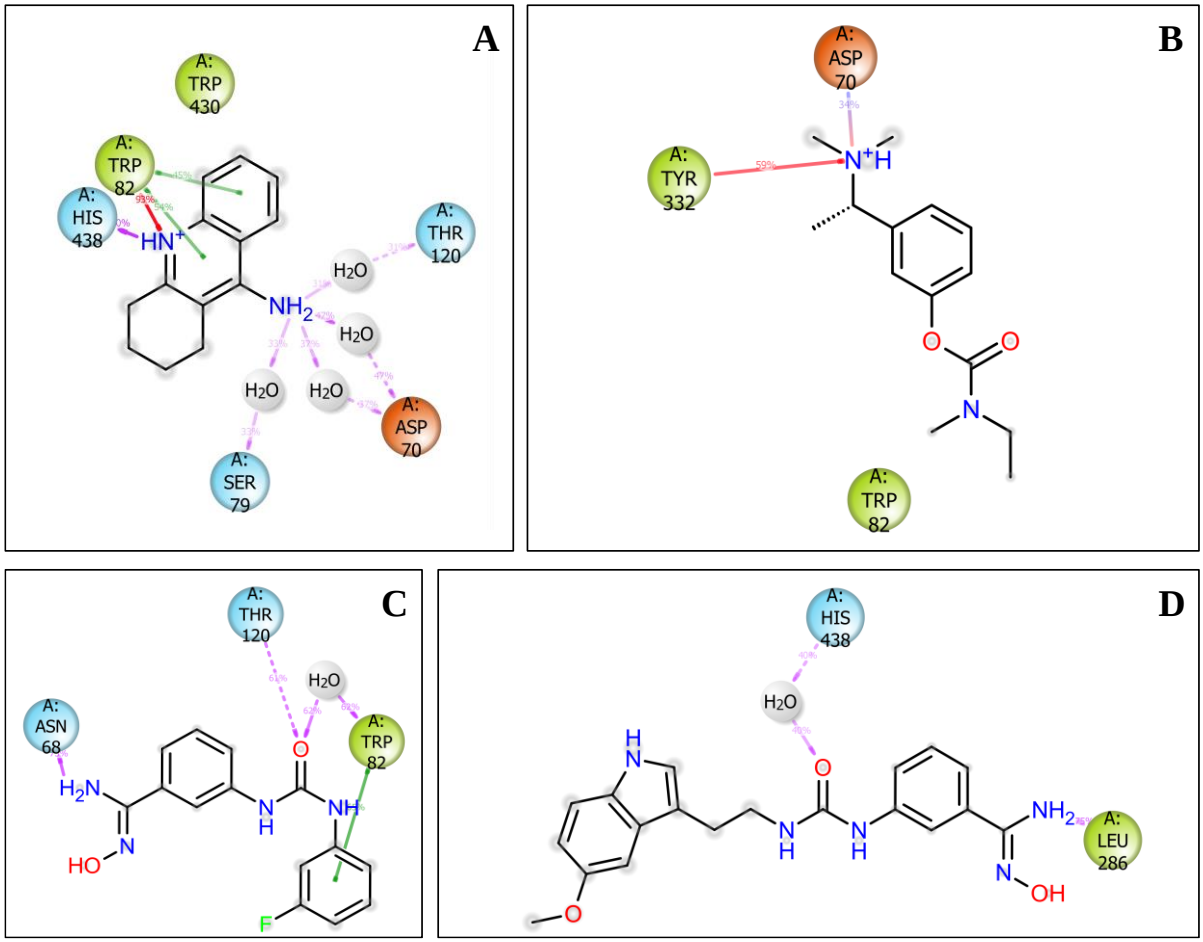

Figure 4.6: BChE-ligand interaction diagrams for the 300 ns simulation with (A) **Tacrine**, (B) **RIV**, (C) **3q**, and (D) **6e** showing interaction time percentages with the residues.

4.3.6. Antioxidant assay

The increased production of reactive oxygen species (ROS) has been proposed to be a primary culprit in AD progression (165-167). Thus, reducing oxidative stress is an important therapeutic strategy in designing a new drug candidate for AD (168, 169). DPPH (2,2-diphenyl-1-picrylhydrazyl) assay is a simple and most convenient *in-vitro* method to screen antioxidant candidates. To explore their antioxidant capacity, we performed a DPPH assay for **3q, 6a, 6b**, and **6e,** the most potent ChE inhibitors. **Quercetin** was used as a reference compound in this assay. DPPH (75 μL of 200 µM) solution was mixed with different concentrations of the compounds (200, 160, 80, 40, and 20 µM) in equal proportion, followed by incubation at 37 ºC for 25 min in a thermomixer. It monitored the % radical scavenging activity by recording the absorbance of the samples. As depicted in **Figure 4.7** and **Table 6**, compounds **3q, 6a, 6b, 6e,** and **Quercetin** significantly scavenge free radicals. On the other hand, **RIV** displayed lower antioxidant activity than that of compounds **3q, 6a, 6b,** and **6e**. The analysis revealed that the test compounds **3q** and **6e** exhibited approximately ten times more potent antioxidant activity than RIV.

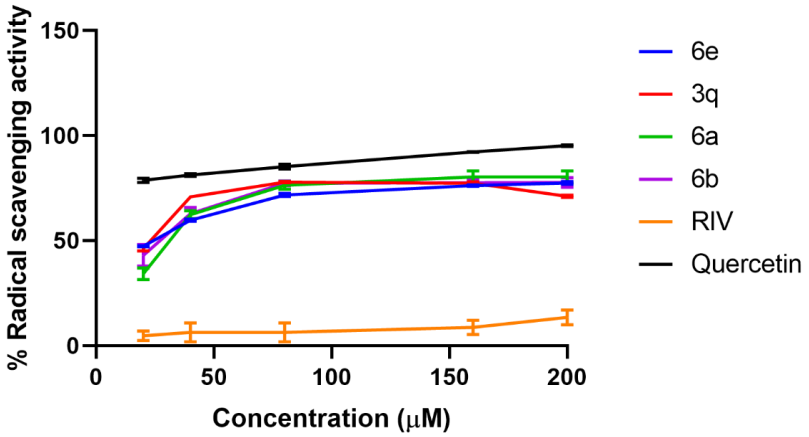

Figure 4.7: The graph represents the percent radical scavenging activity of **3q, 6a, 6b**, **6e**, Quercetin, and **RIV**. Each assay was performed in triplicate. The values are presented as the mean ± SD.

Table 6. Antioxidant activity (DPPH assay) of **3q, 6a, 6b, 6e** and **RIV**.

Compound	**DPPH assay**	
	% Radical scavenging [a]	**IC_{50} (μM) [b]**
3q	46.15 ± 0.84	16.15 ± 1.05
6a	34.24 ± 1.97	22.88 ± 0.41
6b	42.87 ± 3.70	18.40 ± 1.47
6e	47.30 ± 0.16	15.17 ± 0.07
Quercetin[c]	79.40 ± 0.88	03.23 ± 0.04
RIV[d]	4.73 ± 1.60	n.d.[e]

[a]All the values were obtained at a compound concentration of 20 μM, % Radical scavenging; means ± SD of two independent experiments

[b]IC_{50}: 50% inhibitory concentration (means ± SD of two independent experiments)

[c]Quercetin= positive control

[d]RIV = negative control

[e]n.d.: not determine

4.3.7. Inhibition of *self-mediated* $A\beta_{1-42}$ aggregation

The role of the $A\beta_{1-42}$ peptide in the pathogenesis of AD is a common cause of neurodegeneration (170). Hence, we were interested in investigating the $A\beta_{1-42}$ aggregation inhibitory potential of **3q** and **6e**. For this purpose, we carried out the Thioflavin-T (ThT) assay with the $A\beta_{1-42}$ incubated alone or in the presence of an inhibitor. The $A\beta_{1-42}$ solution (12.5 μM, final concentration) alone, or **3q**, **6e, RIV,** and **quercetin** (3.125 μM final concentration) in a ratio (4:1) at 37 °C with agitation at 1200 rpm, were incubated for three

days on a thermomixer, followed by monitoring the $A\beta_{1-42}$ aggregation by addition of ThT (25 μM). It is clear from **Figure 4.8** that compounds **3q** and **6e** effectively inhibit $A\beta_{1-42}$ aggregation, displaying substantially greater efficacy compared to RIV, which demonstrates minimal amyloid inhibition activity.

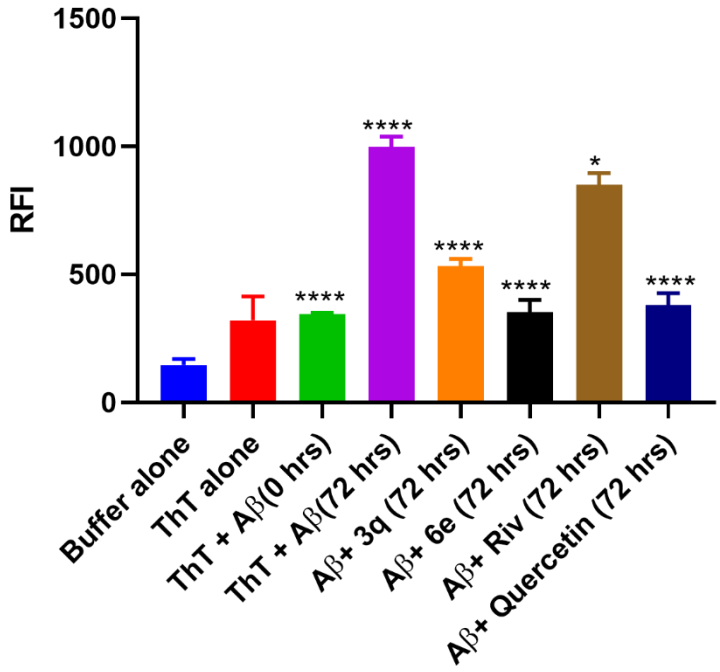

Figure 4.8: The study investigated the inhibitory effects of **3q** and **6e** on the self-induced aggregation of $A\beta_{1-42}$. $A\beta_{1-42}$ monomer. ****p < 0.0001 and *p < 0.0280 vs ThT + Aβ (72 hrs). Data are processed using One-way ANOVA followed by Dunnett's multiple comparison test (Means ± SD of two independent experiments).

4.3.8. Molecular docking and simulation against amyloid beta

4.3.8.1. Interaction of 3q and 6e with Aβ

Docking scores were obtained by running blind docking calculations (**Table 7**). The docking score **6e** was -7.9 kcal/mol and **3q** was -7.5 kcal/mol. Interestingly, the molecules with the best docking scores were redocked in the same pocket (**Figure 4.9A** and **Figure 4.9B**). Further, **3q** engages in π-π interactions with Phe19 residues of the chains A, B, and D.

From the 2D interaction diagram (**Figure 4.9A1**), hydrogen bonding was observed for **3q** with Leu17C. **6e** showed different interactions with the pentameric fibrils. The indole ring of **6e** engaged in π-cation interactions with the Leu17 residues of both B and C chains (**Figure 4.9 B1**). From these interactions, it can be concluded that these two molecules modulated the aggregation of the pentameric $A\beta_{1-42}$ protofibrils.

Table 7. Docking score and interactions of the ligands with amyloid beta fibrils

Sl. No.	Ligands	Docking Score (kcal/mol)	Interactions
1.	**6e**	-7.9	Leu17B (π-cation), Leu17C (π-cation)
2.	**3q**	-7.5	Phe19A (π-π), Phe19B (π-π), Phe19D (π-π), Leu17C (H bond)

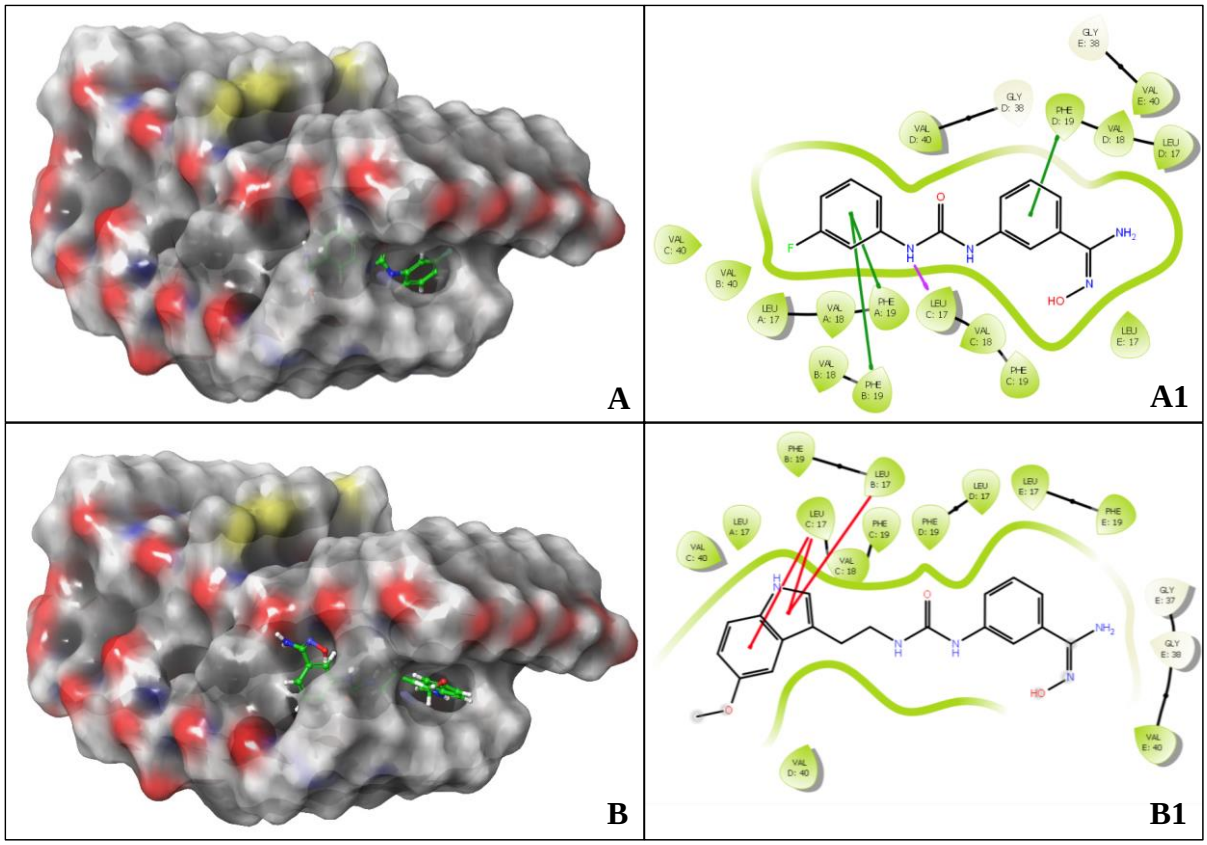

Figure 4.9: Surface representation of (A) **3q** and (B) **6e** docked into the pocket of $A\beta_{1-42}$ protofibrils and 2D interaction diagram of (A1) **3q** and (B1) **6e** of the docked complexes.

Molecular dynamics simulations were performed on the docked complexes and the protofibrils for 150 ns at 310 K and 1 atm pressure. Changes in RMSD, Rg, and SASA for the entire simulation time were analyzed to investigate the interactions and destabilizing effect of the molecules **3q** and **6e**. For the last 50 ns of the simulation, the average value of RMSD for only the protofibrils was 7.65 ± 0.28 Å, the protofibril-**3q** complex was 10.04 ± 0.36 Å, and the protofibril-**6e** complex was 8.23 ± 0.28 Å (**Figure 4.10**). Both the protofibril-molecule complexes exhibited a higher average RMSD value for the last 50 ns of the simulation than the protofibrils, signifying some destabilization. This simulation model could not confirm the results for **3q**, but **6e** showed a destabilizing effect on the amyloid beta protofibrils.

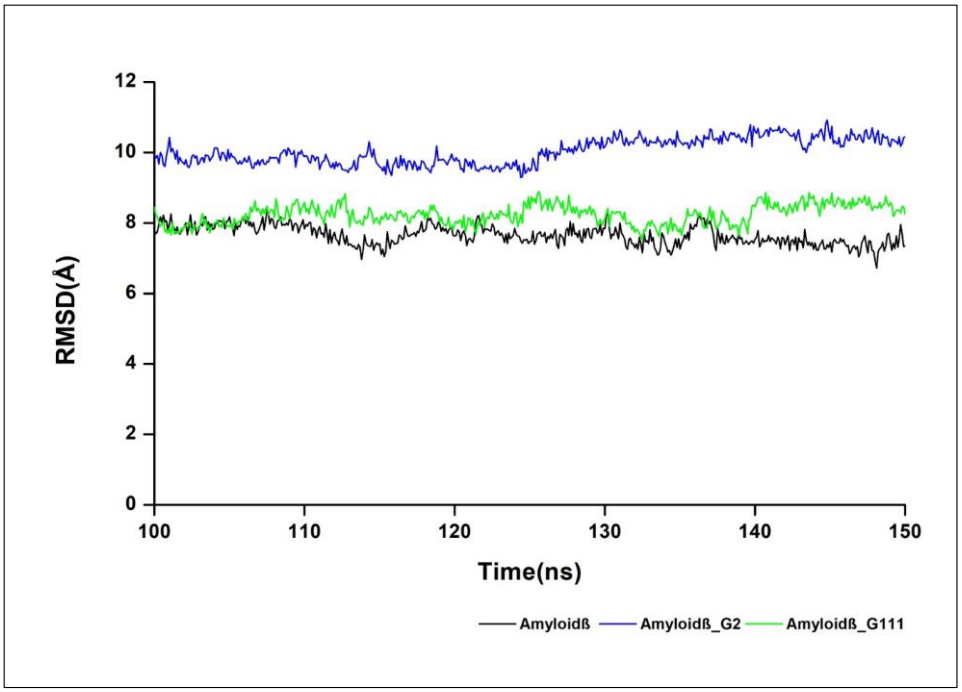

Figure 4.10: RMSD of the backbone atoms of protofibril (black), protofibril-**3q** complex (blue), and protofibril-**6e** (green) complex for the last 50 ns of the molecular dynamics simulation.

4.3.9. Tau protein aggregation inhibition

AD is mainly identified by accumulating specific proteins, known as tau protein and beta-amyloid, in the brain tissues (171, 172). The imbalance of tau proteins is linked to a change in their shape from their normal form, resulting in their separation from microtubules in a disease condition (173). Tau protein undergoes hyperphosphorylation, which causes it to accumulate and form prefibrillar oligomeric aggregates (different multimeric structures). These aggregates can further aggregate into paired helical filaments (PHFs) and neurofibrillary tangles (NFTs) (174, 175). We carried out a ThT assay to study the effect of lead molecules on tau protein aggregation. Tau protein (5 μM) with heparin (aggregate inducer) was incubated alone or with **3q**, **6e**, or **RIV** (1.125 μM) in a 4:1 ratio at 37 °C with agitation (1200 rpm) for three days. The graph of the thioflavin-T experiment (**Figure 4.11**) demonstrates that significant aggregation inhibition was achieved after three days of protein

incubation with **3q** or **6e**. These findings unequivocally demonstrate the plausible interaction between **3q** and **6e** with Tau protein, potentially hindering the formation of tau protein aggregates, a significant improvement over **RIV**, which lacks activity against tau aggregation.

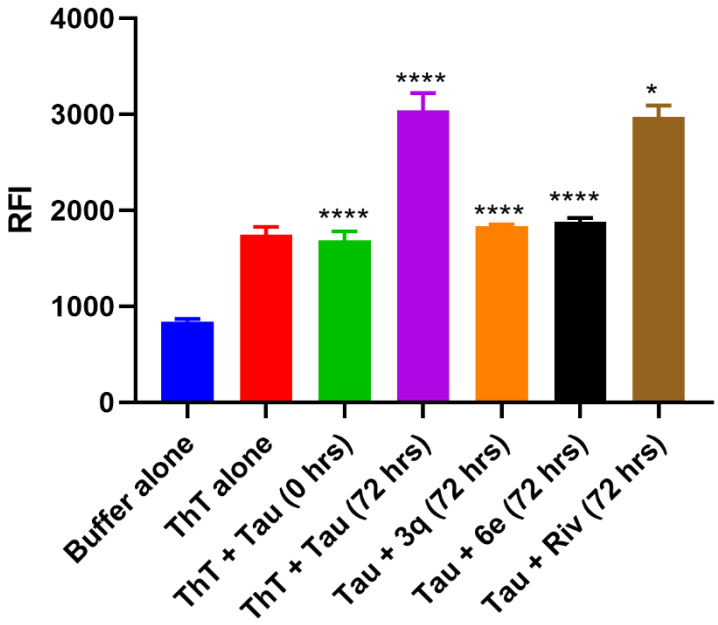

Figure 4.11: Inhibition of self-induced Tau protein aggregation in the presence of **3q** and **6e**. Tau protein monomer (5 µM) in the presence of **3q** & **6e** (1.125 µM), incubate the mixture with ThT (10 µM) at 37°C for 30 min at 300 rpm in an Eppendorf thermomixer. ****p < 0.0001, *p < 0.9064 vs ThT + Aβ (72 hrs.). The data are processed by one-way ANOVA followed by Dunnett's multiple comparison test. (Means ± SD of two independent experiments).

4.3.10. Evaluation of metal chelating and NO release property

Scientific investigations have revealed that irregularities in the levels of biometals like iron (Fe) and copper (Cu) within the brain can contribute to the onset of AD (176-178). We conducted a study to investigate the interaction between the potent ChE inhibitors **3q** and **6e**

with $FeCl_3$ through a metal chelation experiment. The main objective was to better understand how **3q** and **6e** interact with Fe (III) species. The absorbance spectra of **3q** and **6e** alone and **3q** and **6e** in combination with $FeCl_3$ using a UV spectrophotometer were measured. The recorded spectra spanned a range of 200-700 nm. The experiment's outcome indicates that the compounds **3q** and **6e** did not exhibit efficient chelation with iron.

Studies suggest that NO pathways are involved in several neurological disorders, such as AD and other forms of neurodegenerative dementias. NO pathways serve two different functions that contribute to neurodegeneration, as described by Eizo Iseki et al.(179) Firstly, NO produced by the cerebral endothelial cells affects the vascular system, leading to metabolic disorders in the brain. Secondly, NO is involved in neuroinflammation in the brain and causes neurotoxicity by inhibiting mitochondrial respiration, which leads to neuronal cell death. As a result, there is significant interest in measuring NO levels in various biological tissues and fluids. One commonly used method for measuring NO is using a Griess reagent, which detects the presence of nitrite, a stable metabolite of NO. The technique used in this assay is based on a chemical reaction known as diazotization, first reported by Griess in 1879 (180). Six concentrations of **3q** and **6e** were selected for this experiment; for each compound concentration, the absorbance was measured against the concentrations of the compound. The release potential of **3q** and **6e** was illustrated in **Figure 4.12**, which demonstrated that compounds **3q** and **6e** do not release the NO.

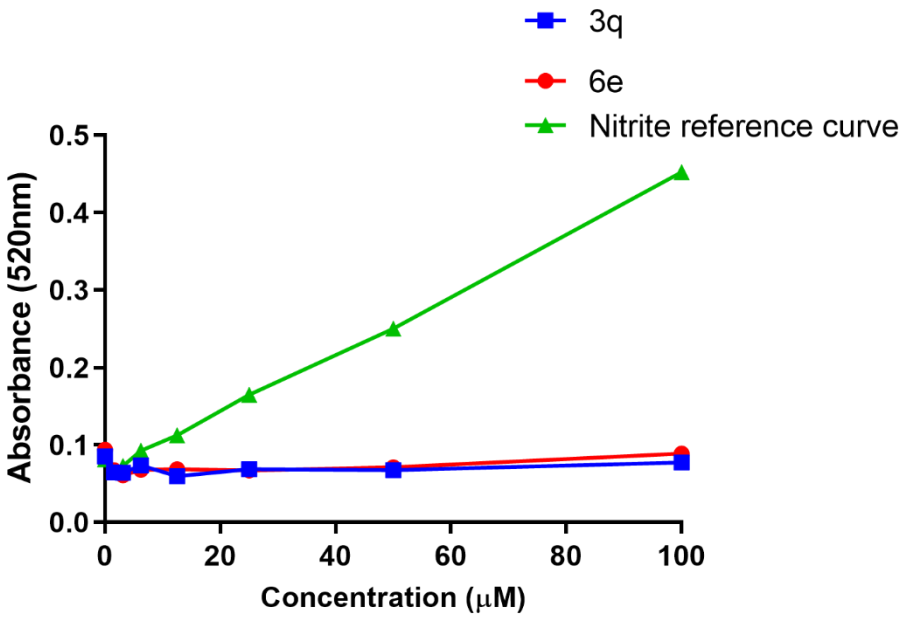

Figure 4.12: Graphical representation of **3q, 6e,** and standard reference curve of nitrite concentration measurement at 520 nm.

4.3.11. Cell cytotoxicity assessment of 3q, and 6e against PC12

Assessing cytotoxicity constitutes a fundamental stride in drug development, with preliminary *in-vitro* inquiries antedating *in-vivo* investigations (181). Molecules **3q** and **6e**, recognized for their potent inhibitory activity against AChE/BChE, coupled with antioxidant properties, underwent cytotoxicity evaluation using the PC12 cell line. PC12 cells, widely employed as an optimal cellular model for pioneering therapeutic strategies in AD, faithfully mimic neurons in morphology, physiology, and biochemical functions. Consequently, all experimental procedures in this study were conducted utilizing differentiated PC12 cells. These cells were exposed to varying concentrations (1, 2.5, 5, 7, 10, 20, and 30 µM) of **3q** and **6e** for 24 hours (**Figure 4.13**), and a quantitative appraisal of cell viability was executed utilizing the 3-(4,5-dimethylthiazol-2-yl)-2,5-diphenyltetrazolium bromide (MTT) assay. The outcomes indicated that **3q** and **6e** showed no cytotoxic effects on PC12 cells at concentrations up to 30 µM.

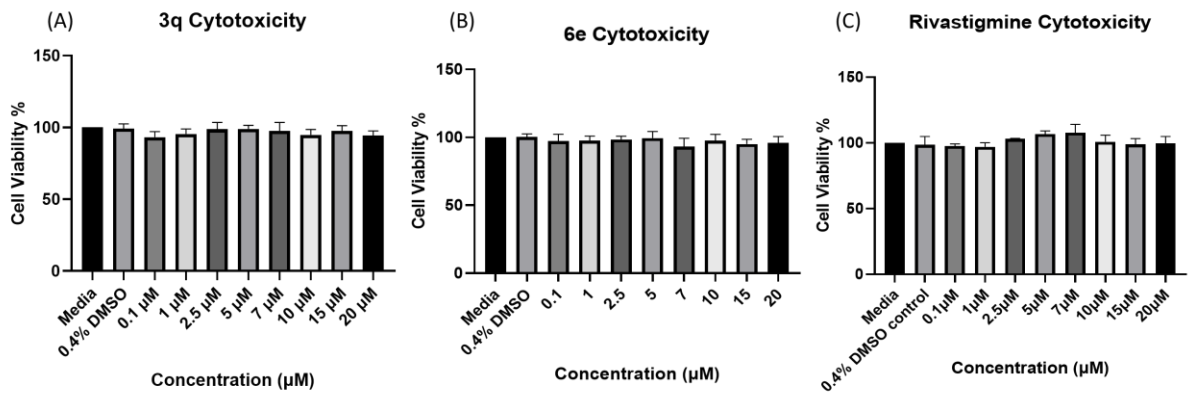

Figure 4.13: The impact of **3q** and **6e** on cellular viability. The cells were subjected to varying concentrations of **3q** and **6e** (1, 2.5, 5, 7, 10, 20, and 30 µM) for 24 hours. The MTT assay was utilized to analyze cell viability, expressed as a percentage. All assays were performed using samples in quadruplicate in three different experiments and presented as mean ± SE.

4.3.12. Evaluation of the neuroprotective effect of 3q and 6e against H_2O_2-induced cell death

Hydrogen peroxide (H_2O_2) is considered a major ROS contributor and is implicated in playing a key role in the pathogenesis of several progressive neurodegenerative diseases. Therefore, H_2O_2-induced cytotoxicity in PC12 cell lines has been adopted as a cell-cultured model of oxidative stress or insult-induced toxicity to evaluate the neuroprotective potency of tested derivatives in in-vitro experimental studies. The effect of **3q** and **6e** on the viability of the PC12 cell line was studied using pro-oxidant H_2O_2 (widely accepted neurotoxin) to induce neuronal cell death via excessive ROS production, increasing oxidative damage within neuronal cells. As we know, oxidative stress is one of the key factors that are responsible for the onset of AD and its progression; therefore, effectively preventing neurons from oxidative damage might significantly prevent disease progression in the early stages of AD and inhibit adverse consequences in AD pathology. Based on our previous publication, the concentrations of **3q**, **6e**, and **RIV** (20, 10, 5, and 2.5 µM) were used. The cells were pre-

treated with different concentrations (20, 10, 5, and 2.5 µM) of **3q, 6e,** and **RIV** for 24 hrs., followed by exposure to H_2O_2 (600 µM) for 24 hrs. As shown in **Figure 4.14**, the data from the MTT assay indicated that both **3q**, **6e**, and **RIV** significantly prevent PC12 cell death at all concentrations (2.5-20 µM) from H_2O_2-induced toxicity. Although the **3q** and **6e** show slightly less neuroprotective activity than the reference drug **RIV** (**Figure 4.14**), the study suggested that **3q** and **6e** can protect neuronal cells from oxidative damage.

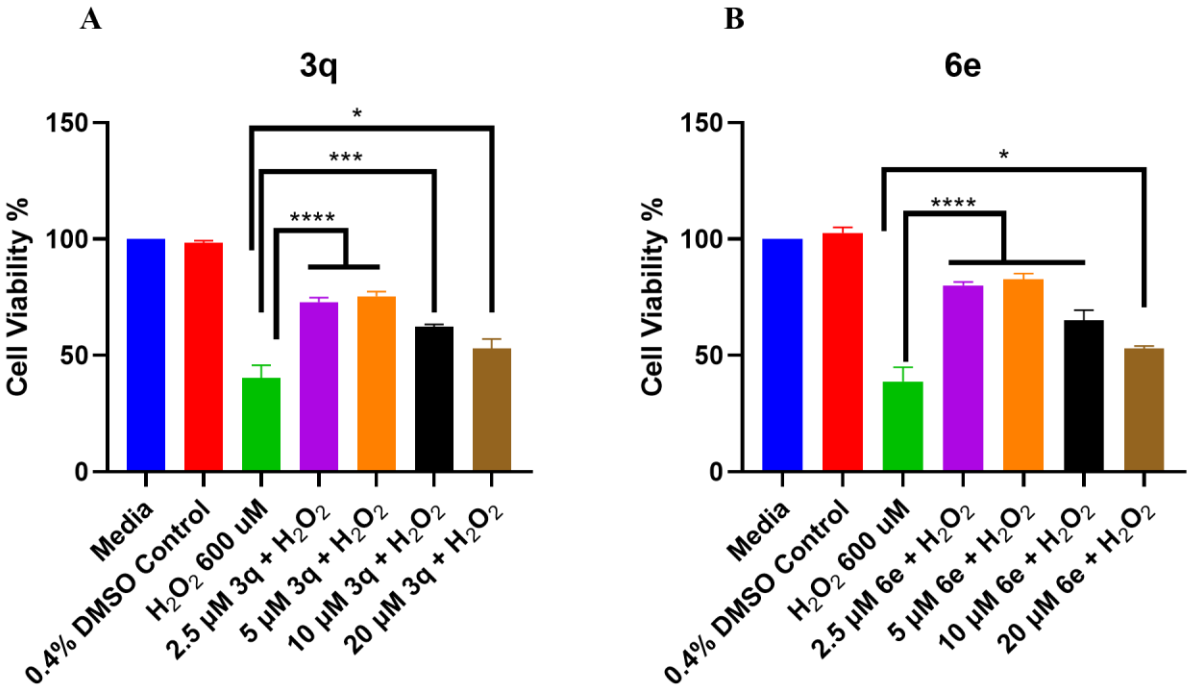

Figure 4.14: Effect of **3q** and **6e** against H_2O_2 mediated cell death. Cells were pre-incubated with **3q** (A) and **6e** (B) at 2.5, 5, 7,10, 15 and 20 µM for 24 h and then further incubated with 600 µM H_2O_2 for another 24 h. Cell death was assessed by MTT assay. All values are represented as (mean ± SD and n>3)

4.3.13. Effect of neuroprotective drug 3q and 6e on apoptosis.

Apoptosis, programmed cell death, is a crucial cellular event that plays an important role in the etiology of various neurodegenerative diseases. Apoptosis was assessed using flow

cytometry by staining the PC12 cells with propidium iodide (PI) and annexin V-FITC. Annexin V enters the cell in both the early and late stages of apoptosis whereas PI stains the cells only in the late or necrosis stage. To assess the effect of neuroprotective **3q**, **6e**, and **RIV** on PC12 cells, $1x10^5$ cells/well were grown in a 24-well plate and incubated with **3q, 6e**, and **RIV** for 24 hours at 20 µM, 10 µM, 5 µM, and 2.5 µM concentrations. Untreated control and apoptosis induction H_2O_2 control showing the different frequencies of expression of live/viable cells and cells, which lead to apoptosis/dead cells.

Viable cells and apoptosis frequency are 79.7% and 2.9%, respectively. On the other hand, we can see a~two-fold decrease in the frequency of the live cell population from 56.7% to 22.8%. The H_2O_2 induced the PC-12 cells to lead to apoptosis. Next, we incubated the PC-12 cells with **3q, 6e,** and **RIV** at 20 µM, 10 µM, 5 µM, and 2.5 µM for 24 h and followed by cells were induced with 600 uM H_2O_2. The cell viability of **3q**: 20 µM (74.8%), 10 µM (57.6%), 5 µM (69.1%), and 2.5 µM (69.1%); **6e**: 20 µM (61.2%), 10 µM (68.8%), 5 µM (72.7%), and 2.5 µM (72.5%); **RIV**: 20 µM (69.7%), 10 µM (69.8%), 5 µM (67.9%), and 2.5 µM (72%) **(Figure 4.15).**

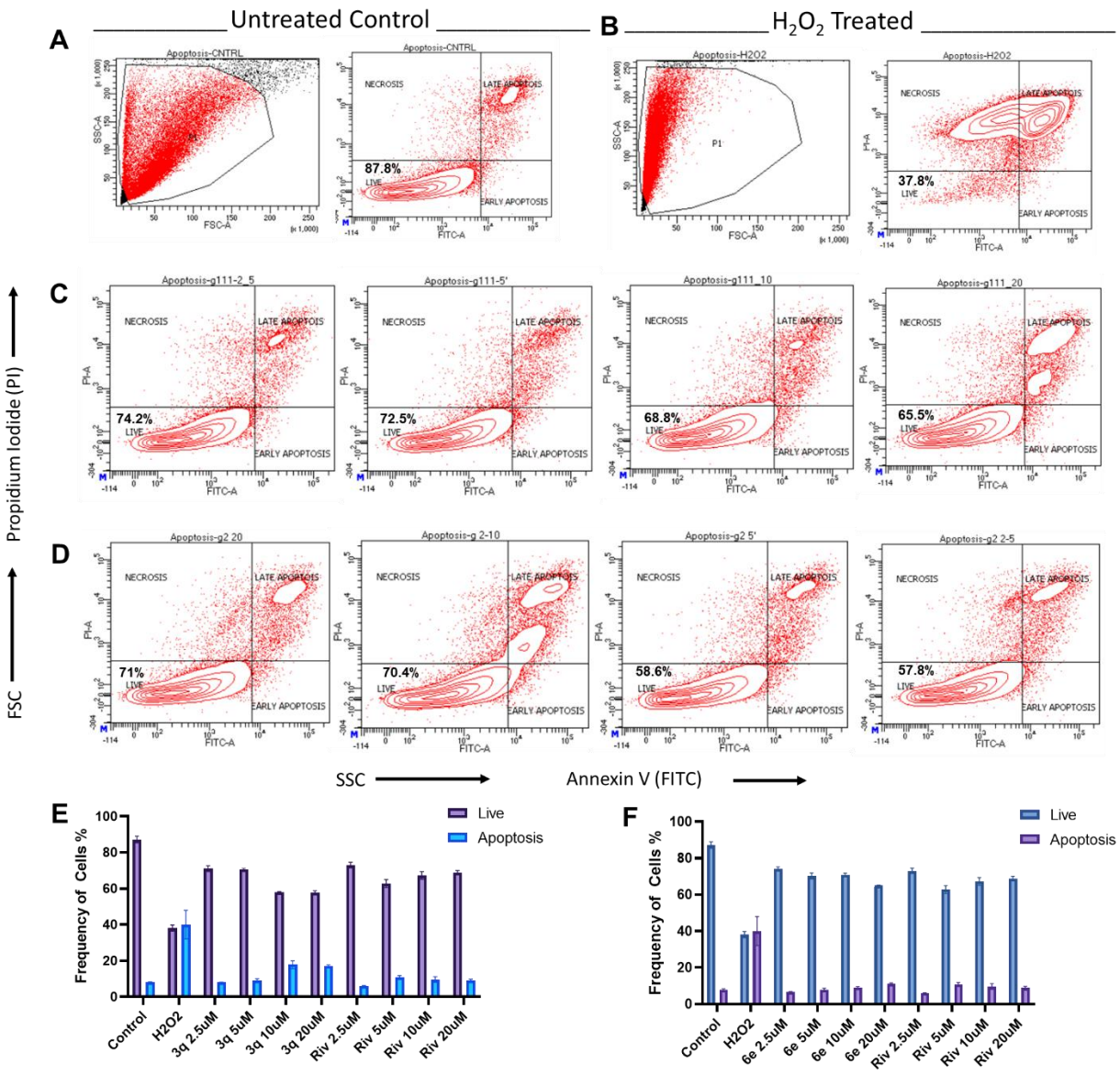

Figure 4.15: The effect of neuroprotective drugs **3q** and **6e** on apoptosis. The flow plot shows the frequency of different subpopulations of untreated control (A) and H_2O_2 control (B) the flow plot shows the frequency of different subpopulations of **3q** (C) and **6e** (D), at 20 µM, 10 µM, 5 µM, and 2.5 µM for 24 h and followed by cells were induced with 600 µM H_2O_2 graph showing the frequency of live cells and apoptosis cells in treatments groups (E-F).

4.3.14. Evaluation of NLRP3 inflammasome inhibitory property

4.3.14.1. Compounds 3q and 6e inhibited microglial activation by attenuating ROS release and mitochondrial damage

The priming and activation stages appear to lead to the NLRP3 inflammasome cascade. Through the TLR/NF-κB signaling pathway, toll-like receptor 4 (TLR4) agonists such as LPS initiate the priming process by promoting the production of precursor proteins like NLRP3, pro-IL-18, and pro-IL-1. The activation stage causes the NLRP3 inflammasome complex to assemble and is triggered by stimuli like ATP. ASC controls the activation step's recruitment of the cysteine protease pro-caspase-1, which interacts with CARD to promote the assembly of the NLRP3 inflammasome. Pro-caspase-1 cleaves to become active caspase-1, which then matures pro-IL-1 and pro-IL-18 into their respective active forms (182). Thus, our work examined the estimation of mitochondrial ROS and its membrane potential disrupted by inducing agents such as LPS+ATP and further explored the effect of **3q** and **6e** in attenuating the mitochondrial ROS and restoring the mitochondrial membrane potential, as shown in **Figure 4.16**. The *in-vitro* experimental timeline has been shown in **Figure 4.16A**. Compounds **3q** and **6e** inhibited LPS and ATP-induced cytotoxicity in HMC-3 cells. Both compounds at a dose of 12.5 µm exhibit significant proliferation of HMC-3 cells compared to the LPS and ATP-treated group (**Figure 4.16B**).

Treatment with the test compounds **3q** and **6e** showed a significant reduction in the production of mitochondrial ROS in HMC-3 cells compared to the LPS and ATP-treated group (**Figure 4 .16C, D**). Inhibiting ROS production has played a crucial role in attenuating neuroinflammation and oxidative stress-mediated neuronal death. Mitochondrial destabilization-induced NLRP3 inflammasome activation through the signal 2 step in microglial cells aggravates inflammation and neuronal death in the brain. Therefore, our study explored the role of compounds **3q** and **6e** in regulating the MMP in the microglial cells. Treatment with **3q** and **6e** at a dose of 12.5µm significantly stabilizes the MMP and

inhibits the ROS release and mitochondrial impairment compared to the LPS and ATP-treated group (**Figure 4.16E-H**). These results demonstrate the strong potential effect of the compounds in regulating ROS production and stabilizing the MMP.

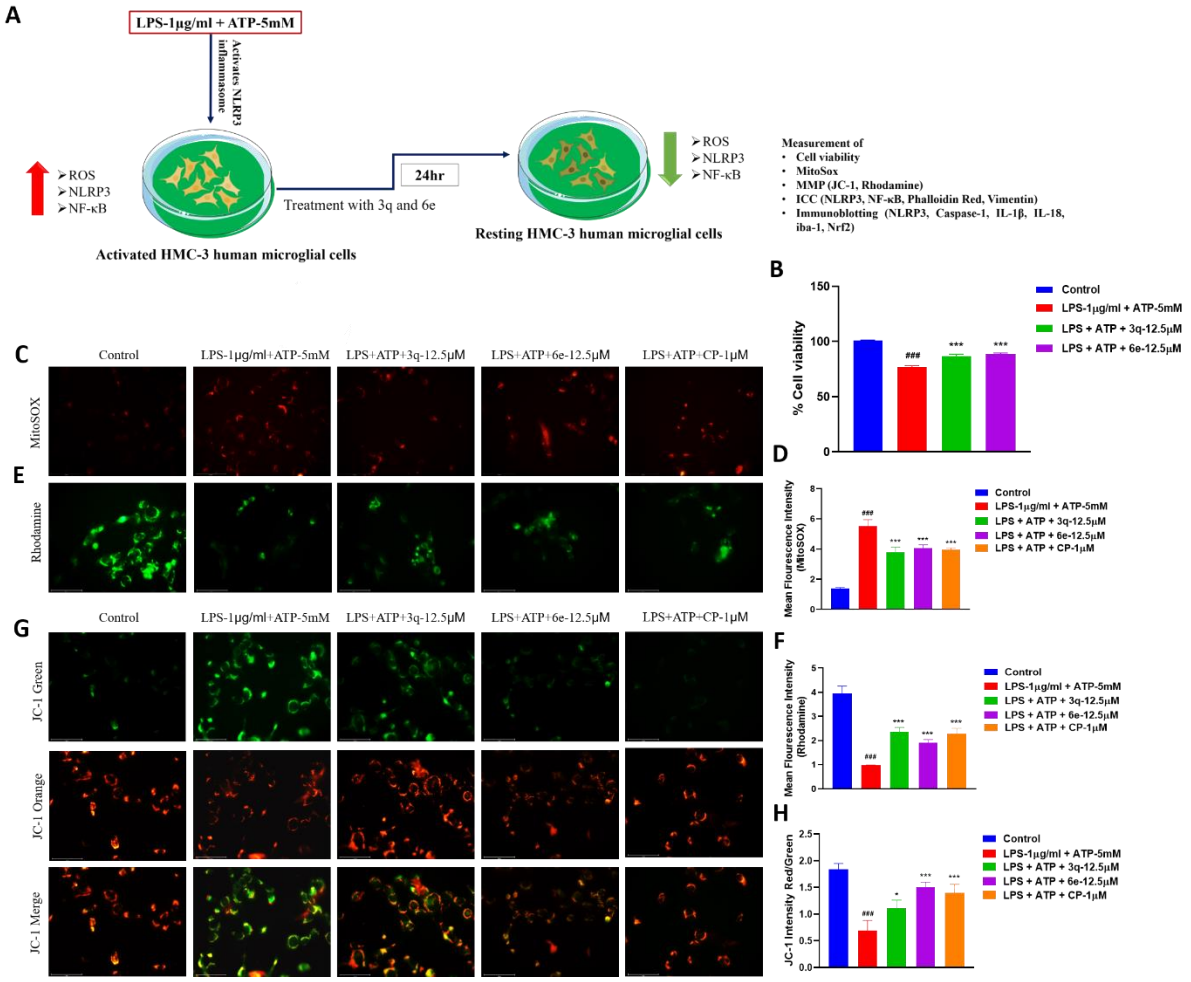

Figure 4.16: Compounds **3q** and **6e** exert microglial cell proliferation and attenuate the ROS and MMP damage caused by LPS and ATP. A) Graphical representation depicting the *in-vitro* experimental design. B) To check the proliferative effect of compounds against NLRP3 inflammasome-mediated inflammation, HMC-3 cells were primed with LPS (1µg/ml) and ATP (5 mM). Further cells were treated with the test compounds at a dose of 12.5µM. Compounds **3q** and **6e** showed a significant increase in microglial proliferation compared to the LPS+ATP-treated group. C) Representative images of MitoSOX staining in HMC-3 cells and D) Bar Graph of MitoSOX assay. E, F) Rhodamine stained HMC-3 cells and Bar graph.

G, H) JC-1 stained HMC-3 cells and Bar graph to study the MMP. All the data were analyzed as mean ± SD (n=3). The data was analyzed using one-way ANOVA followed by Tukey's test, in which the LPS+ATP group was compared with the normal control group and different treatment groups. Significant differences were denoted as $^{###}p<0.001$ vs. normal control, and $*p<0.05$, and $***p<0.001$ vs. LPS+ATP group.

4.3.14.2. Evaluation of the ability of 3q and 6e to inhibit NLRP3 inflammasome, and NF-κB expression levels in microglial cells

Recent studies have demonstrated the critical function of NLRP3 inflammasome inhibitors in managing neurodegenerative disorders. Since neuroinflammation and neurodegeneration are critically involved in the initiation and progression of AD, thus, targeting nuclear factor-kappa B (NF-κB) and NLRP3 inflammasome activation by P2X7/NLRP3/caspase 1 pathway may be a sensible tactic to combat AD pathogenesis. Treatment with compounds **3q** and **6e** at a dose of 12.5 µm showed a marked reduction in the expression levels of NF-κB and NLRP3 in the human microglial cells, suggesting its anti-inflammatory and anti-microglial activation effects (**Figure 4.17A, C**). To further correlate the anti-inflammatory effects of compounds, a decrease in the nuclear translocation of NF-κB was observed when compared to the LPS and ATP-stimulated group (**Figure 4.17B, D**). Vimentin levels were regulated in the compounds **3q** and **6e** treated group compared to the LPS and ATP stimulated group (**Figure 4.17B, E**). The results confirm the effect of compounds in regulating the ROS levels, stabilizing the MMP, and inhibiting the NLRP3 activation-mediated microglia phagocytosis and subsequently attenuating neuroinflammation.

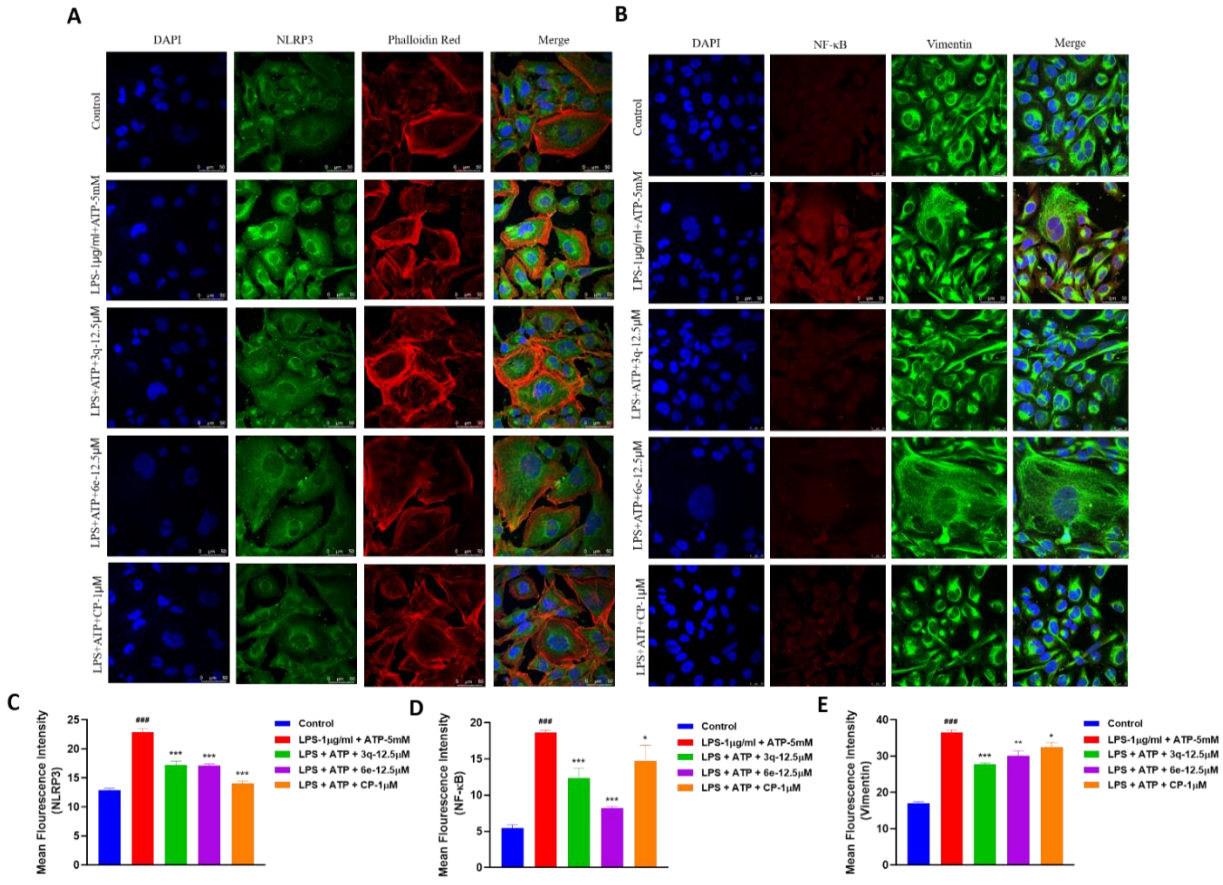

Figure 4.17: Compounds **3q** and **6e** inhibit microglial activation and subside the NF-κB and NLRP3 inflammasome activation as evidenced by Immunocytochemistry (ICC) staining of HMC-3 cells for NLRP3, NF-κB, Vimentin and Phalloidin Red. A, C) HMC-3 cells stained with DAPI (nuclear stain), NLRP3 (Green), and Phalloidin red (Red) to assess NLRP3 inflammasome expression and microglial activation and Bar graph representing the Mean Fluorescence intensity of NLRP3. B, D, and E) Confocal images and bar graph representing the HMC-3 cells stained with NF-κB and Vimentin. All the data were analyzed as mean ± SD (n=3). Statistical significance was further determined by one-way ANOVA followed by Tukey's test in which the LPS+ATP group was compared with normal control, where statistical significance was defined as $^{###}p<0.001$ vs normal control, and *p<0.05, **p<0.01, and ***p<0.001 vs LPS+ATP treatment group.

4.3.14.3. Impact of 3q and 6e on NLRP3 inflammasome signaling cascade and halting the release of pro-inflammatory cytokines in human microglial cells.

Interleukin-1β (IL-1β) and/or interleukin-18 (IL-18) are proteolytically activated due to caspase-1 activation, which causes an inflammatory response. IL-1β is regarded as a gatekeeper cytokine that plays a crucial role in numerous events connected to the activation and regulation of inflammation. An inflammatory response is triggered downstream by the active cytokines. Additionally, it breaks down Gasdermin D into its active form, causing Pyroptosis. Compounds **3q** and **6e**, when treated with LPS+ATP-activated microglial cells, showed a marked reduction in the expression levels of NLRP3, caspase-1, IL-1β, and IL-18 (**Figure 4.18A-E**). A significant decrease in the production of inflammatory cytokines was observed in the LPS and ATP-stimulated microglial cells, confirming the effect of compounds in regulating microglial activation-mediated neuroinflammation. Similarly, an increase in the levels of nrf2 was observed in the treatment group compared to LPS-stimulated glial cells (**Figure 4.18A, G**). Further, microglial activation marker iba-1 levels were significantly downregulated in the cells treated with **3q** and **6e** compared to the LPS+ATP-treated group. Overall, the immunoblotting results confirm the molecular mechanism involved in the compounds, demonstrating a significant reduction in NLRP3 expression and its downstream signaling cascade.

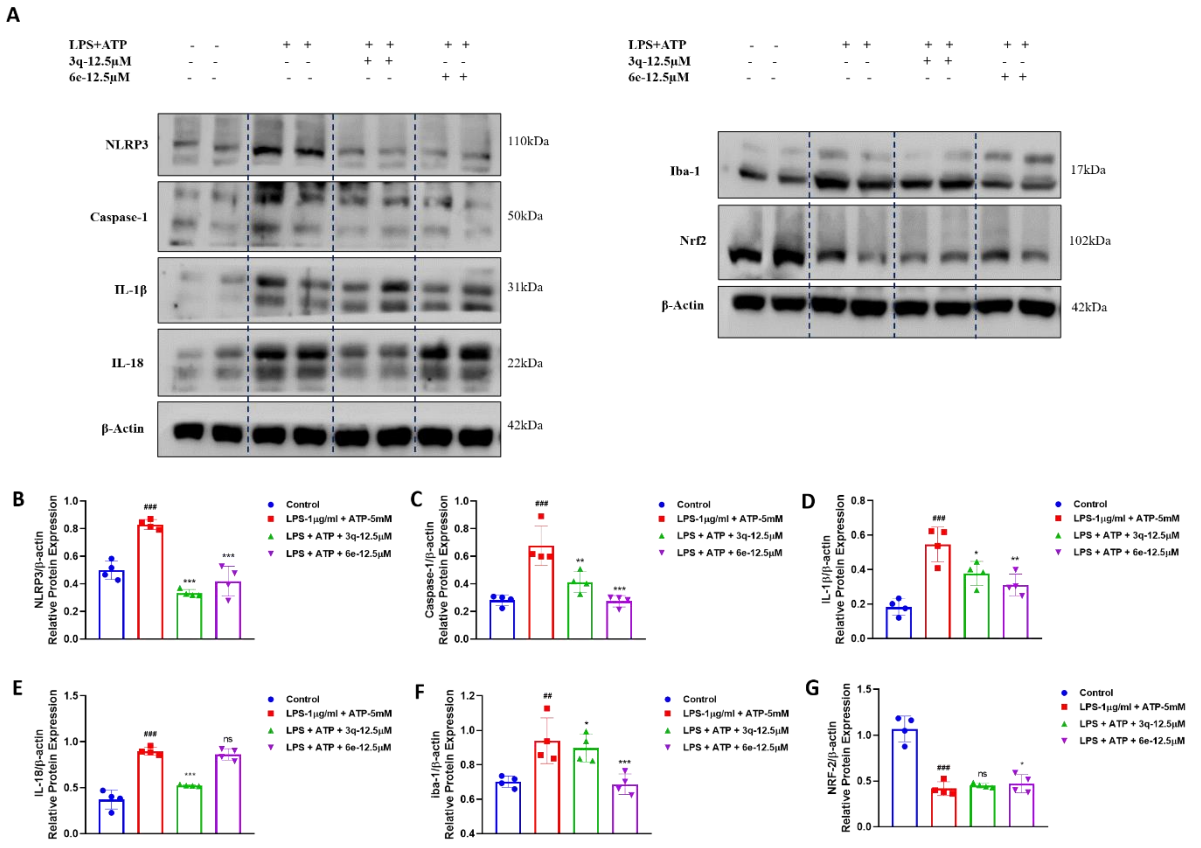

Figure 4.18: Compounds **3q** and **6e** inhibited microglia activation and NLRP3 inflammasome activation. (A) Western blot showing protein expression of NLRP3 and pro-caspase-1, pro-IL-1β, and pro-IL-18 to their active forms caspase-1p20, active IL-1β, and IL-18, iba-1 and NRF2 in the HMC-3 cells (n = 4). (B−G) Graphical depiction of Western blotting and densitometry analysis of NLRP3, active caspase-1, IL-1β, and IL-18, iba-1 and NRF2 were done by ImageJ (n = 4). All the data were analyzed as mean ± SD. Statistical significance was further determined by one-way ANOVA followed by Tukey's test in which the LPS+ATP group was compared with normal control, where statistical significance was defined as $^{\#\#}p<0.01$, and $^{\#\#\#}p<0.001$ vs normal control, and *p<0.05, **p<0.01, ***p<0.001, and ns vs LPS+ATP treated group.

4.3.15. Evaluation of neuroprotection ability of 3q, 6e and RIV in AD drosophila model

4.3.15.1. Therapeutic effects of 3q, 6e and RIV on OregonR^{+} and an AD model of drosophila

The different concentrations of **3q, 6e,** and **RIV** were administered to OregonR^{+} to determine the median lethal dose (LD_{50}). The OregonR^{+} flies grown in normal food did not show any lethality, while flies grown in **3q** (0.01 mg/ml) showed 98% eclosed flies, approximately 2% pupal death was observed, 0.05 mg/ml appeared 100% eclosed flies, 0.1 mg/ml demonstrated 61% eclosed flies and 39% progeny died at the late pupal stage. **3q** at 0.5 mg/ml and 1 mg/ml showed 17% and 12% eclosed flies, respectively, and the rest progenies died at early and late pupal stages; **3q** at 1 mg/ml was more toxic than 0.5 mg/ml. Thus, **3q** at 0.01, 0.05, and 0.1 mg/ml exhibited no significant toxicity for flies' development and were used for future application against AD [**Figure 4.19 (IA)**]**.** Similarly, **6e** at 0.01mg/ml showed 98% eclosed flies, 2% pupal lethality, 0.05 mg/ml indicated 87% eclosed flies, 13% pupal death, 0.1 and 0.5 mg/ml exhibited 76% eclosed flies, 24% pupal lethality. **6e** at 1 mg/ml and 2 mg/ml were toxic and showed only 45% and 40% eclosed flies; the rest of the progenies died at the early and late pupal stage [**Figure 4.19 (IB)**]. To evaluate the safety and effectiveness of **3q** and **6e**., **RIV** at 50 µM showed 88% eclosed flies and 12% pupal lethality, while at 100 µM demonstrated 83 % eclosed flies and 17 % pupal lethality, and 200 µM and 400 µM showed only 57% and 53% eclosed flies, and rest progenies died at the pupal stage [**Figure 4.19 (IC)**].

Further, **3q**, **6e**, and **RIV** were given to $A\beta_{1\text{-}42}$ expressing flies to examine the eye phenotypes. The OregonR^{+} flies were grown in normal food and exhibited 100% normal eye phenotype, whereas untreated AD flies exhibited 42% mild and 58% severe rough eye phenotypes [**Figure 4.19 (II, III)**]. The **3q** at 0.01 mg/ml administered to AD flies showed 48% mild, 23% severe, and 28% rescued eye phenotypes, whilst 0.05 mg/ml demonstrated 26% mild, 13% severe, and 61% rescued eye phenotypes [**Figure 4.19 (II A, III)**]. At 0.1 mg/ml AD flies exhibited only 27% mild, 44% severe, and 29% rescued eye phenotypes [**Figure 4.19 (IIA, III)**]. Likewise, **6e** at 0.01 mg/ml was fed to AD flies, demonstrating 43%

mild, 30% severe, and 0.05 mg/ml displayed 50% mild, and 23% severe; both concentrations displayed alike (27%) rescued eye phenotypes. **6e** at 0.1 mg/ml proved 60% mild, 23% severe, and uplifting concentration to 0.5 mg/ml displayed 53% mild, 30% severe, equally rescued eye phenotypes (17%) by both dosages [**Figure 4.19 (IIB, III)**]. Interestingly, **RIV** at a concentration of 50 µM established 37% mild, 33% severe, and 30% rescued eye phenotypes, whilst a concentration of 100 µM evidenced 40% mild, 33% severe, and 27% rescued eye phenotypes [**Figure 4.19 (IIC, III)**]. Thus, the study revealed that **3q** at 0.05 mg/ml, **6e** concentrations at 0.01 and 0.05 mg/ml, and **RIV** 50 µM could provide potential dosages for protecting the rough eye phenotype of AD flies. In summary, **3q, 6e,** and **RIV** were initially administered to OregonR^+ flies to execute the dose determination [**Figure 4.19 (IA, IB, IC)**]. Afterward, safe **3q, 6e,** and **RIV** dosages were applied against AD flies to examine the neuroprotective effects. The **3q** concentration of 0.05 mg/ml, **6e** concentrations of 0.01 and 0.05 mg/ml, and RIV 50 µM were more effective against the AD model of Drosophila [**Figure 4.19 (IA, IIA, III)**].

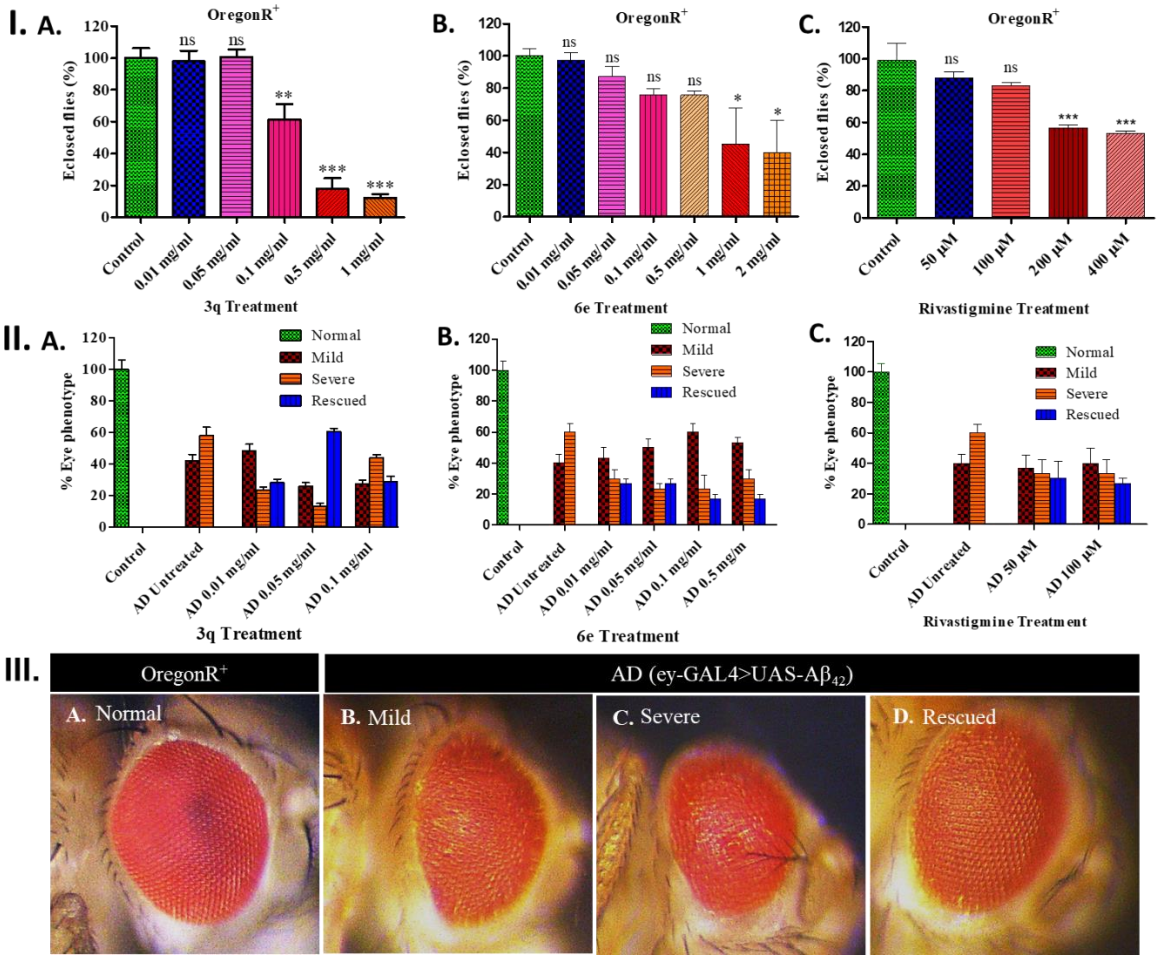

Figure 4.19: Represents the examination of **3q, 6e,** and **RIV** drugs on OregonR^{+} and AD flies. **I.** Represents the dose determination of **3q, 6e,** and **RIV** drugs using wild-type flies**.** The One-way ANOVA test ascribed as non-significance (ns) *p>0.05* and significance ***p<0.001*, ****p<0.0001*. **II.** Illustrates the quantitative examination of eye phenotype of AD flies after administration of **3q, 6e,** and **RIV** drugs. **III.** Shows the eye phenotype of control and AD flies after administration of the above-mentioned drugs.

4.3.15.2. Evaluation of 3q, 6e, and RIV on the mitochondrial and cellular oxidative stress in AD drosophila model

Mitochondrial superoxide was measured using the superoxide indicator MitoSOX^{TM} Red. In the AD, untreated 3rd instar larval eye imaginal discs increased superoxide level ranges, and 2- 4 folds were found compared to control. The superoxide level was measured

optimally in the eye imaginal discs of AD larvae treated with **3q** at 0.01 and 0.05 mg/ml, equivalent to control [**Figure 4.20I (A, C, D)**] and [**Figure 4.20I (A', C', D')**]. **3q** at 0.1 mg/ml, the superoxide level in the eye imaginal discs of AD larvae exhibited a 1.5-fold higher level than that of the control [**Figure 4.20I (A, E)**] and [**Figure 4.20I (A', E')**]. Similarly, mitochondrial superoxide levels were also evaluated in **6e**-treated AD larval eye imaginal discs. The **6e** concentrations 0.01, 0.05, and 0.1 mg/ml treated eye imaginal discs showed comparable superoxide levels to the control [**Figure 4.20II (A, C, D, E)**] and [**Figure 4.20II (A', C', D', E')**], while the concentration 0.5 mg/ml treated eye imaginal discs showed 2-fold upregulated superoxide levels compared to control [**Figure 4.20II (A, F)**] and [**Figure 4.20II (A', F')**]. To examine the effect of the reference drug RIV on AD larval eye imaginal discs to measure the superoxide level, the **RIV** concentration of 50 µM exhibited a superoxide level reduction closer to the control [**Figure 4.20III (A, C)**] and [**Figure 4.20III (A', C')**]. The **RIV** concentration 100 µM treated eye imaginal discs showed >2 fold upregulated superoxide levels as compared to control [**Figure 4.20III (A, D)**] and [**Figure 4.20III (A', D')**]. To check the effects of **3q, 6e,** and **RIV** drugs on oxidative stress, Mitochondrial superoxide was examined in eye imaginal discs of OregonR^+ and AD larvae using the mitochondrial superoxide-sensitive MitoSOX^{TM} Red. The superoxide indicator is a derivative of dihydroethidium (DHE) that contains a cationic triphenylphosphonium group (TPP+), which aids in transport to the mitochondrial matrix of living cells (183). In the presence of mitochondrial superoxide, MitoSOX^{TM} Red oxidizes and generates red fluorescence that helps quantify the mitochondrial superoxide (ROS) level (184, 185).

Likewise, total cellular ROS level was also examined using H2DCFDA in OregonR^+ and **3q, 6e, RIV**-treated and untreated AD larval eye imaginal discs. The eye imaginal discs of untreated AD larvae showed 2.8 to 3.8-fold higher cellular ROS levels than the control [**Figure 4.21I (A, B)**] and [**Figure 4.21I (A', B')**]. The **3q** at 0.01 and 0.1 mg/ml treated AD

larval eye imaginal discs exhibited 1.7-fold upregulation of cellular ROS level compared to the control [**Figure 4.21I (A, C, E)**] and [**Figure 4.21I (A', C', E')**]. Whereas the **3q** at a dose of 0.05 mg/ml demonstrated the optimum level of ROS compared to the control [**Figure 4.21I (A, D)**] and [**Figure 4.21I (A', D')**]. Similarly, **6e** at 0.01, 0.05, and 0.1 mg/ml displayed a reduction in cellular ROS levels almost closer to control [**Figure 4.21II (A, C, D, E)**] and [**Figure 4.21IIA', C,' D,' E'**)]. The **6e** (0.5 mg/ml) has proven to be more toxic, with approximately 2-fold ROS level than the control [**Figure 4.21II (A, F)**] and [**Figure 4.21II (A', F')**]. Next, the reference drug **RIV** at a concentration of 50 µM demonstrated the drop in ROS level as comparable to the control. In comparison, the dosage of 100 µM was considered to be lethal and exhibited approximately 1.5-fold upregulated cellular ROS level when compared with the control. Thus, consequences show that **3q** concentrations at 0.01, 0.05 mg/ml, **6e** at 0.01, 0.05, and 0.1 mg/ml, and **RIV** 50 µM can effectively protect against oxidative stress in the AD model of drosophila.

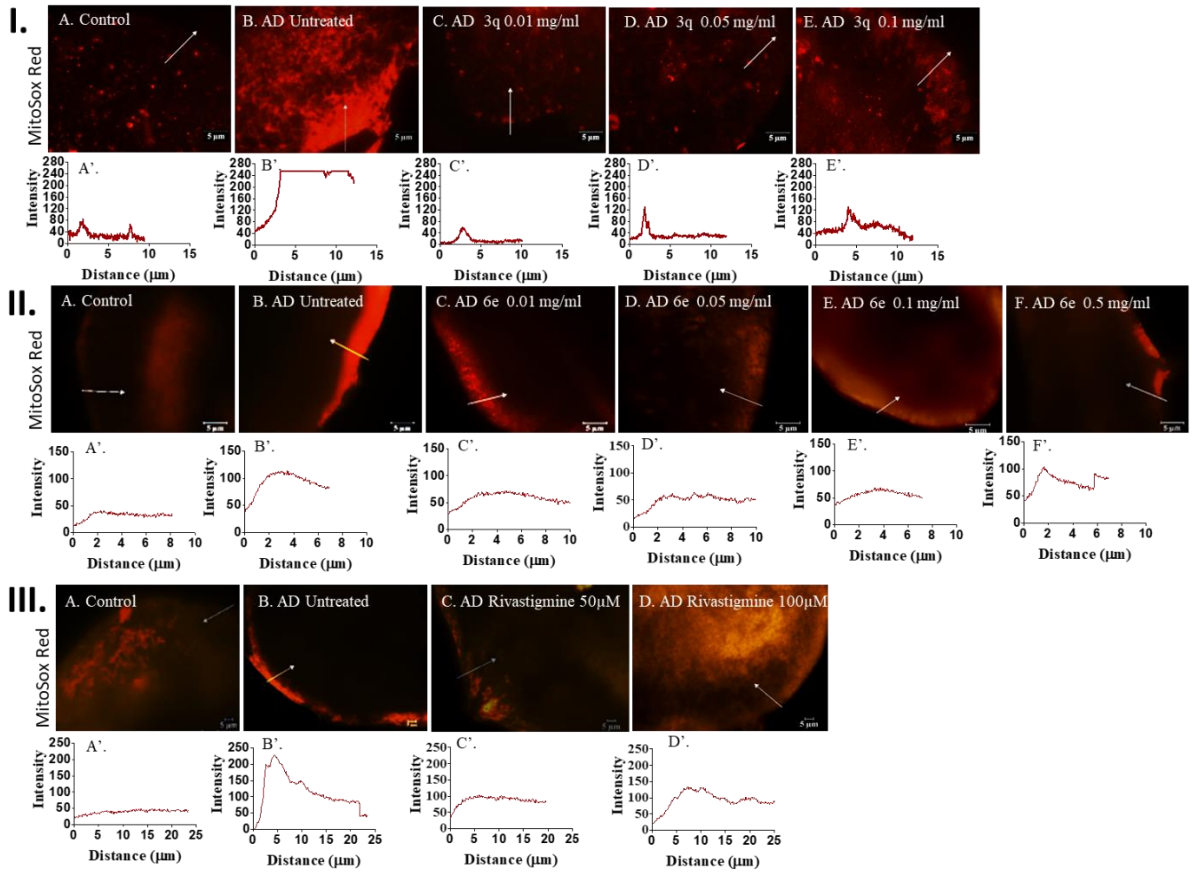

Figure 4.20: Mitochondrial superoxide (ROS) level measurement in Oregon^{+} and Aβ_{42} expressing eye imaginal discs of Drosophila. Fluorescence images of 3rd instar larval eye imaginal discs showing MitoSOX^{TM} Red staining. **I. (A)** Control, **(B)** AD untreated, **(C)** AD treated with **3q** 0.01 mg/ml, D. **3q** 0.05 mg/ml, E. **3q** 0.1 mg/ml. **II.** A. Control, B. AD untreated, **C**. AD treated with **6e** 0.01 mg/ml, **D**. **6e** 0.05 mg/ml, **E**. **6e** 0.1 mg/ml, **F**. **6e** 0.5mg/ml. **III.** A. Control, B. AD untreated, C. AD treated with **RIV** 50 µM, D. **RIV** 100 µM. Respective line graphs showing the MitoSOX^{TM} Red fluorescence intensity in each group's 3rd instar larval eye imaginal discs.

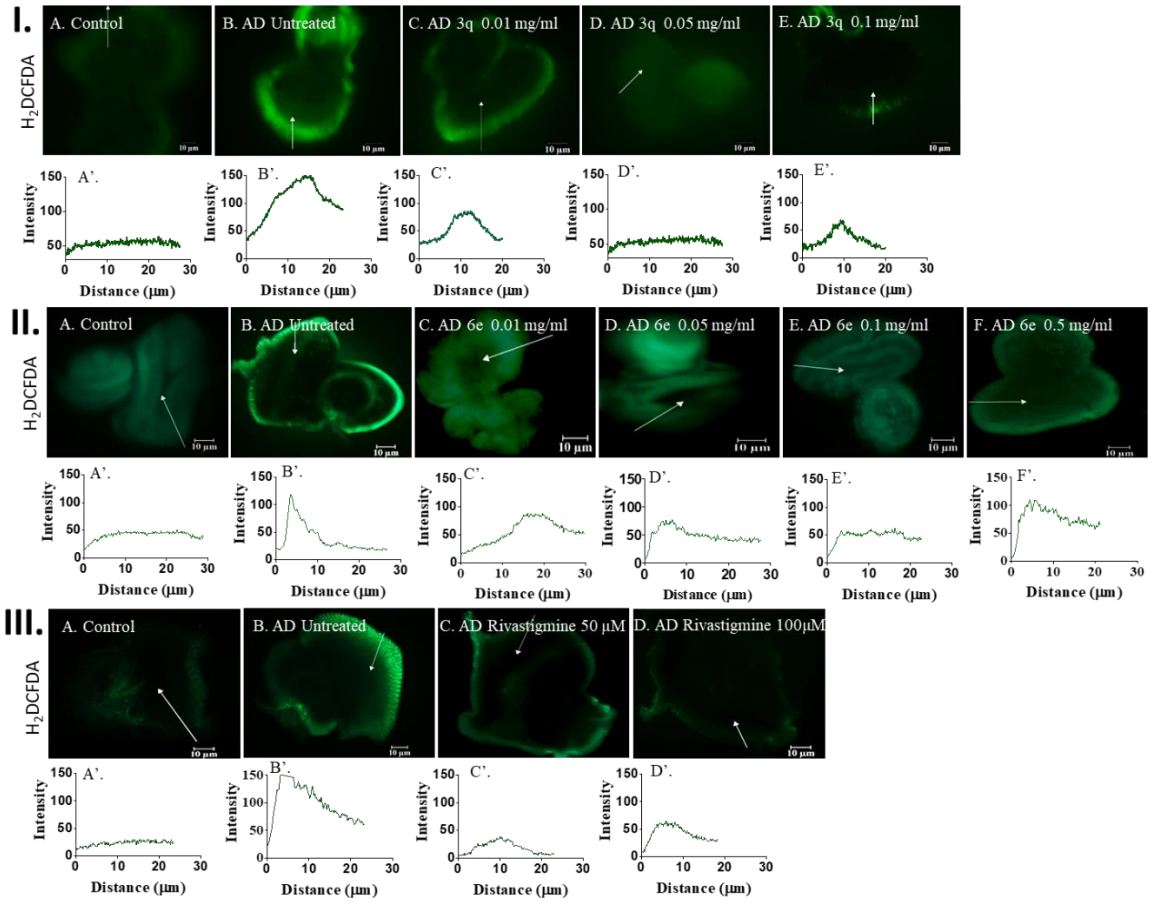

Figure 4.21: Measurement of total cellular ROS level in OregonR^{+} and Aβ_{42} expressing eye imaginal discs of Drosophila. Fluorescence images of 3rd instar larval eye imaginal discs showing H2DCFDA staining. **I.** A. Control, B. AD untreated, C. AD treated with **3q** 0.01 mg/ml, D. **3q** 0.05 mg/ml, E. **3q** 0.1 mg/ml. **II.** A. Control, B. AD untreated, C. AD treated with **6e** 0.01 mg/ml, D. **6e** 0.05 mg/ml, E. **6e** 0.1 mg/ml, F. **6e** 0.5mg/ml. **III.** A. Control, B. AD untreated, C. AD treated with **RIV** 50 µM, D. **RIV** 100 µM. Respective line graphs show the H2DCFDA fluorescence intensity in each group's 3rd instar larval eye imaginal discs.

4.3.16. *In-vitro* blood-brain barrier permeation assay

This study was conducted to assess the brain permeability of test compounds to aid in the development of potential anti-Alzheimer medications. (186) Norfloxacin and testosterone were used as reference standards to validate the experiment. According to the findings, compounds with a permeability value (*Pe*) higher than four had high blood-brain barrier

(BBB) permeability. In contrast, those with a Pe value lower than two were classified as having low BBB permeability (187, 188). The analysis revealed that the test compounds **3q** and **6e** exhibited a permeability value (*Pe*) exceeding 4, suggesting their ability to traverse the BBB and reach their intended targets within the brain.

Table 8. The permeability (*Pe*) of **3q**, **6e**, testosterone, and norfloxacin was determined in the PAMPA assay were expressed in Pe = 10^{-6} cm s^{-1}.

S.No.	**compound**	***P_e* (exp)[a]**	**Reference value [b]**	**Prediction [c]**
1.	**Testosterone**	18.43 ± 0.6	17.0	CNS (+)
2.	**Norfloxacin**	0.12 ± 0.01	0.1	CNS (-)
3.	**3q**	10.67 ± 0.3	------	CNS (+)
4.	**6e**	12.34 ± 0.2	------	CNS (+)

Reference values were obtained from a study by Di Li et al.(187)

Their study classified compounds as CNS (+) if their Pe value was greater than 4.0, indicating high permeability to the central nervous system (CNS). Conversely, compounds were classified as CNS (-) if their Pe value was less than 2.0, indicating low permeability to the CNS. For compounds with Pe values between 2.0 and 4.0, the permeability to the CNS was uncertain and categorized as CNS (±).

4.3.17. Acute toxicity and hepatotoxicity studies

The safety profile is an essential parameter in the development of new drugs. Compounds 3q and 6e, identified as the most potent multifunctional anti-Alzheimer's agents in our study, were evaluated in Swiss albino mice to assess acute toxicity. Following OECD guidelines, a single oral dose of 2000 mg/kg was administered to each animal (n = 3 per group). The animals were carefully observed for any signs of toxicity, behavioral changes, or mortality over a defined observation period. The absence of observable adverse effects at this

high dose indicates a favorable preliminary safety profile for both compounds, supporting their potential for further preclinical development (**Figure 4.22**).

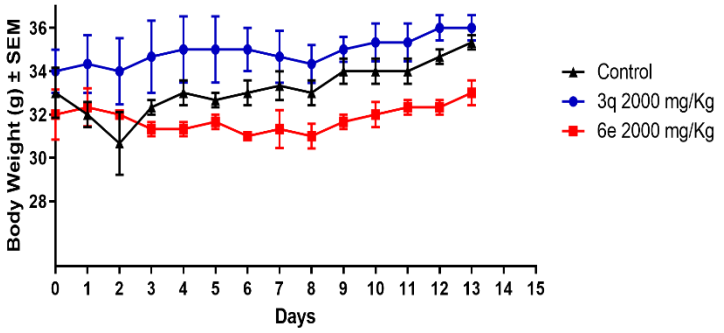

Figure 4.22: The graph represents the average daily body weight of each group of mice over a 14-day period of drug administration with a dosage of **3q** and **6e** at 2000 mg/kg.

4.3.18. Evaluation of *in-vivo* efficacy of 3q & 6e in scopolamine-induced AD mice model

A Y-maze experiment was conducted to evaluate the potential improvement in learning and memory, involving the daily oral administration of compounds **3q** and **6e** to mice afflicted with learning and memory impairments. The scopolamine-induced inhibition of the muscarinic cholinergic receptor nerve terminals, a well-established animal model for AD, induced learning and memory deficit in mice. The test compounds, **3q** and **6e**, were systematically administered to healthy male Swiss albino mice in doses of 5.25 and 10.5 mg/kg, *i.p.*, over 7 days, with subsequent analysis of their body weights (**Figure 4.23A**).

On the 7th day, a Y maze experiment was executed to evaluate the spatial working memory in mice after the intraperitoneal administration of **scopolamine** at a 1.4 mg/kg dosage. The animals were subjected to pre-treatments of **3q/6e/Riv/DPZ**, administered 30 minutes before the introduction of **scopolamine**. The quantification of spontaneous alterations was performed 15 minutes after the administration of **scopolamine**. A noteworthy decline in spontaneous alternation was noted in the group subjected to scopolamine hydrochloride treatment (1.4 mg/kg, *i.p.*), in contrast to the control group receiving the

vehicle. This discrepancy strongly suggested the emergence of amnesia in the mice under observation (**Figure 4.23B**). The group treated with **DPZ** (5.0 mg/kg, *p.o.*) exhibited heightened levels of spontaneous alternations when compared with the group subjected to **scopolamine** treatment. A comparable outcome emerged in the case of **3q** and **6e** (at doses of 5.25, and 10.5 mg/kg), revealing a meaningful disparity in the percentage of spontaneous alterations when juxtaposed with both the scopolamine-treated and DPZ-treated groups. The augmentation of spontaneous alternation in the scopolamine model appears to be facilitated through the anti-AChE function of compounds **3q** and **6e**. This implies that **3q** and **6e** are robust cholinesterase inhibitors, displaying the capacity to traverse the blood-brain barrier effectively. The comprehensive findings from the scopolamine-induced amnesia model imply that compounds **3q** and **6e** hold substantial promise in enhancing both spatial and immediate memory in mice.

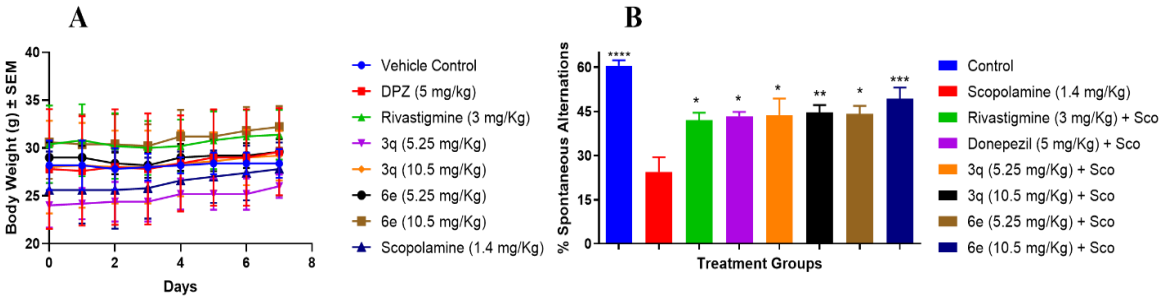

Figure 4.23: The study examined the impact of **3q** and **6e** on memory deficits induced by scopolamine in the Y-maze test. **3q and 6e** were administered intraperitoneal (*i.p.*) at 5.25 mg/kg and 10.5 mg/kg. DPZ was given at a 5 mg/kg *i.p.* dose for 7 consecutive days. The data are presented as the mean ± SEM (n = 6). Data are expressed as mean ± SEM (n = 5), ****p < 0.0001; ***p < 0.0002, **p < 0.0021 vs. scopolamine group. (One-way ANOVA followed by multiple Dunnett comparison test).

4.3.19. Neurochemical Profiling and Antioxidant Property Assessment

Ex-vivo investigations were conducted using the above-treated subjects to delve into the AChE, BChE, and antioxidant impacts of **3q** and **6e**. The quantification of AChE and BChE levels in the brain was accomplished through a modified method of Ellman's

colorimetric technique. As illustrated in **Figures 4.24A** and **4.24B**, the administration of scopolamine markedly increases the levels of AChE and BChE compared to the control group receiving the vehicle. However, compounds **3q, 6e, Riv** and **DPZ** groups substantially decreased the escalated AChE and BChE levels. These observations indicate that **3q** and **6e** effectively mitigate cholinesterase levels within the brain.

The ex-vivo antioxidant capacity of **3q** and **6e** was evaluated through diverse biochemical markers, encompassing superoxide dismutase (SOD), catalase (CAT), and malondialdehyde (MDA). SOD, functioning as an enzyme, serves to safeguard cellular constituents against oxidative stress induced by ROS, ultimately curtailing cellular harm. It facilitates the conversion of the superoxide (O_2^-) radical into molecular oxygen (O_2) and hydrogen peroxide (H_2O_2).

CAT is a prevalent enzyme that facilitates the breakdown of hydrogen peroxide (H_2O_2) into water and oxygen. MDA, which arises as a byproduct of lipid peroxidation, serves as an indicator of oxidative stress. MDA is subject to condensation with thiobarbituric acid, resulting in the emission of red fluorescence. As depicted in **Figure 4.24C**, the group of mice treated with **scopolamine** displayed a notable decline in SOD levels. Intriguingly, the administration of **DPZ** resulted in a significant elevation of SOD levels in the treated animals. Notably, the administration of the lead compounds **3q** and **6e** effectively countered the diminished SOD levels observed in the scopolamine-treated animals.

Moreover, noteworthy enhancements in catalase (CAT) activity within the brain supernatant were discernible in the **DPZ** treatment group (depicted in **Figures 4.24D**) and the **3q** and **6e** treatment groups. Conversely, the contents of MDA demonstrated a corresponding reduction in the **DPZ**, **3q**, and **6e** (shown in **Figure 4.24E**), compared to the **scopolamine**-treated group. These observations imply the robust in-vivo potential of **3q** and **6e** as an inhibitor of ChE and an agent with antioxidant activities.

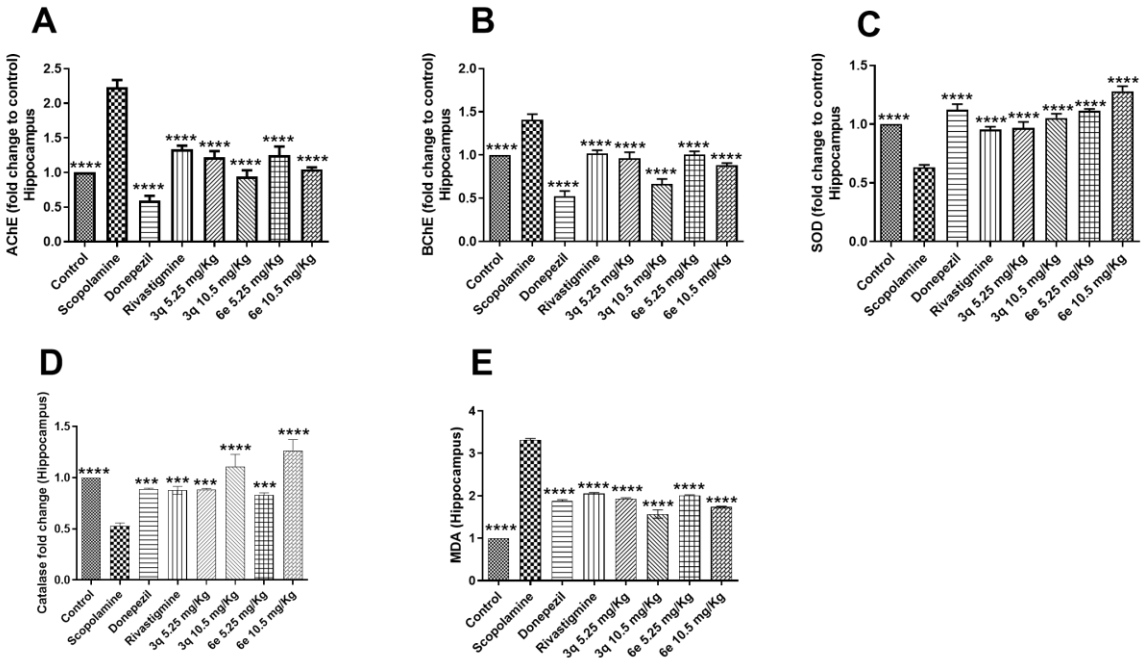

Figure 4.24: The ex-vivo analysis of mice hippocampus with AChE, BChE, SOD Catalase, and MDA levels by the scopolamine-treated group with various treatment groups of **3q** and **6e**, respectively. (A) Elevated AChE. (B) Elevated BChE level. (C) SOD (Fold change to control). (D) Catalase (CAT) (fold change to control). (E) MDA (fold change to control). Data are expressed as mean ± SEM (n = 5), ****p < 0.0001; ***p < 0.0002, **p < 0.0021 vs. scopolamine group. (One-way ANOVA followed by multiple dunnet comparison test).

4.3.20. Evaluating *in-vivo* efficacy of 3q and 6e in reversing scopolamine-induced cognitive deficits in the Morris water maze test

4.3.20.1. Behavioral measurements

The successful development of an effective therapeutic agent for AD is anticipated to ameliorate cognitive impairment in affected patients significantly. The Morris Water Maze (MWM) experiment is a comprehensive tool that captures diverse behavioral changes encompassing spatial and working memories, cognitive maps, and place learning. This test is widely recognized as a robust gold standard for evaluating the therapeutic potential of anti-AD compounds (189).To further substantiate the potential of **3q** and **6e** as a viable

therapeutic candidate for AD, we examined its efficacy in the MWM at 10 mg/kg (*i.p.*). Morris water maze test was performed to measure spatial memory and learning in the milieu of scopolamine-induced dementia in mice. After ten days of scopolamine treatment, animals were trained for 5 days, and the escape latency (time to reach the platform) was plotted against the training days (**Figure 4.25A**). The disease control group mice took more time to find the platform than control animals. Animals treated with **3q, 6e,** and **RIV** (standard control) were gradually trained over five days, and their escape latency was significantly decreased compared to disease control groups (**Figure 4.25B**). On the 6^{th} day, the platform was removed, and the probe test was performed. The time spent in the platform quadrant was measured, signifying memory retention (**Figure 4.25C**). The test and standard group animals showed an increased percentage of time in the platform quadrant compared to disease control groups. The distance traveled to reach the platform (target) was measured, which indicated that the animals took shorter routes with more training to escape swimming. The distance traveled was significantly reduced in test groups **3q** and **6e** compared to the scopolamine-treated group (**Figure 4.25D**). The entry of animals in the quadrant where the platform was formerly placed denotes the ability to retain the spatial memory of the target of trained mice. The animals treated with **3q** and **6e** test compounds showed a significantly enhanced number of entries in the target quadrant (**Figure 4.25E**).

Passive avoidance was performed after 14 days of scopolamine treatment to check the mice's learning and memory impairments. **Figure 4.26A** shows the escape latency for the animals in different groups to enter the blank chamber after 24 hours of electric shock. It was observed that disease-control animals had significantly less latency than control animals, denoting that they developed memory deficits after scopolamine treatment. Additionally, **RIV**, **3q,** and **6e** showed a significant increase in latency period when compared to only the

scopolamine-treated group. Therefore, it can be interpreted that test drugs **3q** and **6e** showed protection against scopolamine-associated dementia.

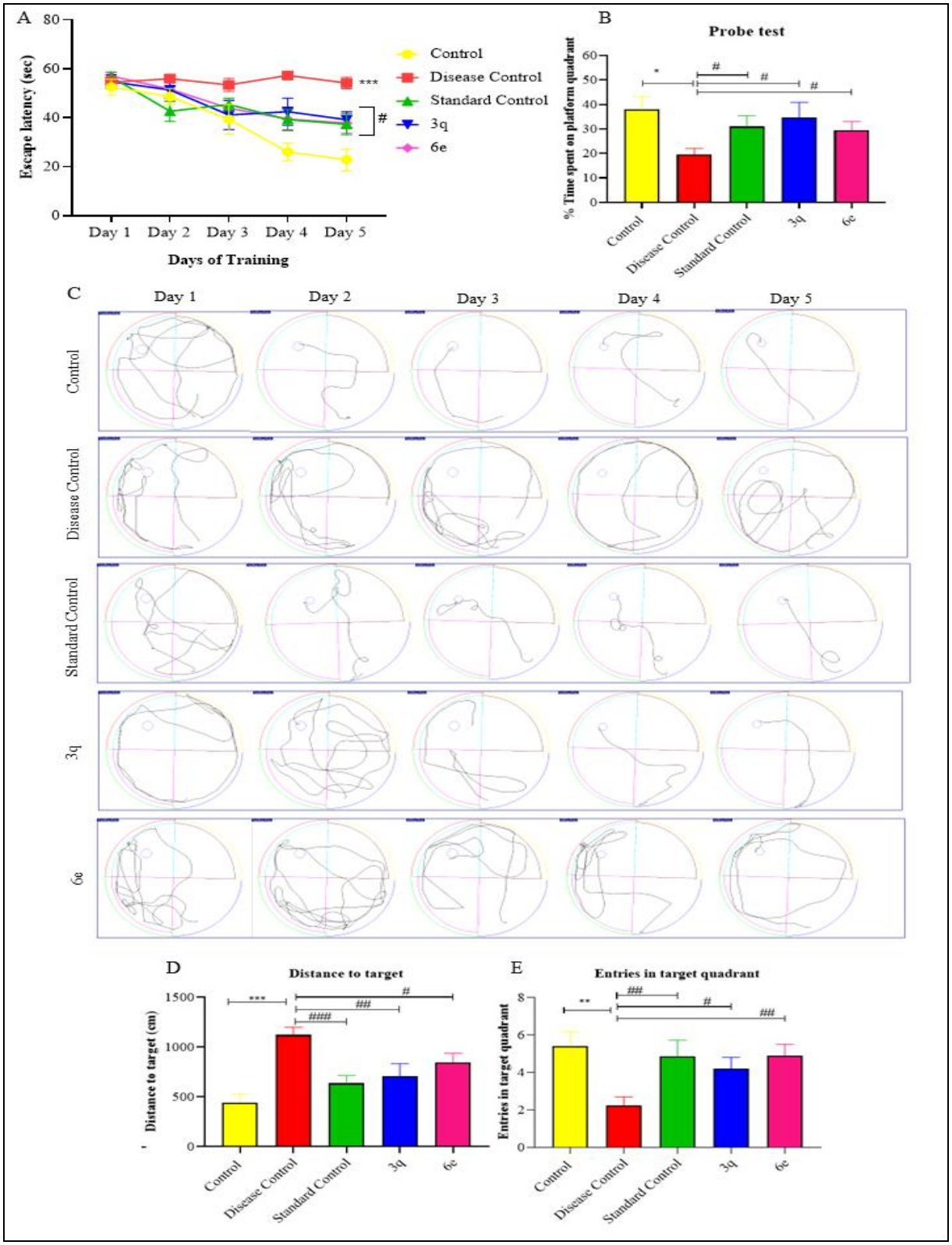

Figure 4.25: Performance of mice in Morris water maze. **A.** Escape latency of mice in control, disease control, standard control, **3q** and **6e** (10 mg/kg) groups upon the training of 5 days in MWM; **B.** Representative swimming paths of the mice in different treatment groups; **C.** Probe test; **D.** Graph represents the distance to reach the platform in cm by mice in different treatment groups **E**. Graph represents the number of entries in the platform quadrant by mice in different treatment groups. All data are expressed as the mean ± SEM (n = 10), *** $p < 0.001$, **$0.001 < p < 0.01$, *$0.01 < p < 0.05$ denotes control vs. disease control; ### $p < 0.001$, ## $0.001 < p < 0.01$, # < 0.05, denotes disease control vs. standard control or **3q** and **6e**. (One-way ANOVA followed by Tukey's multiple comparison test).

4.3.20.2. Additional neuroprotective activities

RT-PCR results were observed using various memory-related markers such as BDNF, TRKB, CREB1, PSD 95, c-FOS, PKA, Nr4a2, and GAP 43 (**Figure 4.26B**). BDNF is one of the important molecules involved in plastic changes related to learning and memory. TRKB is the receptor at which BDNF binds, and the cascading downstream pathways occur. Both BDNF and TRKB genes have been observed to be downregulated with 14 days of scopolamine treatment compared to the control group, whereas in standard drug and test drugs **3q** and **6e**, the markers were significantly overexpressed compared to the disease control group. CREB1, Nr4a2, c-FOS, and PKA are other markers important for memory, especially long-term memory formation. The expression of these genes was reduced effectively in animals receiving scopolamine for two weeks compared to the control group of animals.

Furthermore, the animals receiving **3q** and **6e** followed by scopolamine injection showed improved gene expression of these memory markers compared to the group with only scopolamine administration. PSD 95, also known as DLG4, is a member of the membrane-

associated guanylate kinase family functioning as a scaffolding protein at excitatory synapses. GAP 43 is a marker of neuronal growth and plasticity. Both these markers were also significantly overexpressed in test drug-administered groups compared to disease control group animals.

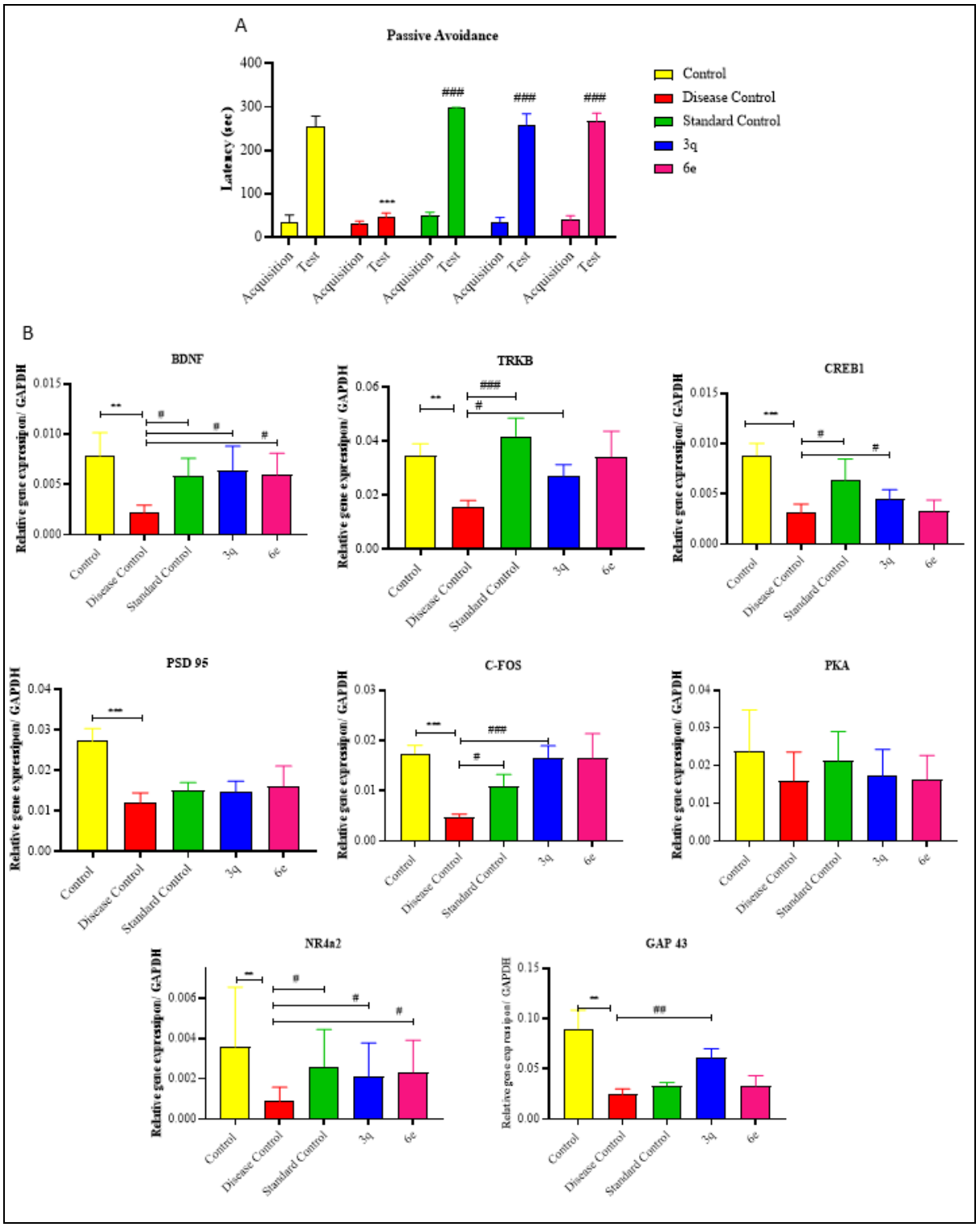

Figure 4.26: A. Graph represents latency of mice in control, disease control, standard control, **3q** and **6e** (10 mg/kg) groups in Passive avoidance; **B.** Graph represents relative gene expression/ GAPDH of mice in different treatment groups: BDNF, TRKB, CREB1, PSD 95, C-FOS, PKA, NR4a2, GAP 43. All data are expressed as the mean ± SEM (n = 10), *** $p < 0.001$, **$0.001 < p < 0.01$, *$0.01 < p < 0.05$ denotes control vs. disease control; ### $p < 0.001$, ## $0.001 < p < 0.01$, # < 0.05, denotes disease control vs. standard control or **3q** and **6e** (One-way ANOVA followed by Tukey's multiple comparison test).

4.4. Rationale behind the design of the second series of carbamate-based tryptamine derivatives

Given the significant roles of AChE and BChE in AD's pathogenesis, there is an urgent need for compounds capable of precisely inhibiting both enzymes rather than targeting a single enzyme. Additionally, it is imperative for newly developed molecules to target AD's pathological hallmarks, such as oxidative stress, protein aggregation (Aβ), and cell apoptosis. However, the marketed RIV is a potent inhibitor of BChE and a weak inhibitor of AChE and also suffers from several limitations, including weak antioxidant properties and the absence of Aβ aggregation inhibition. Several carbamate analogs have been reported in the literature (117, 156), Intriguingly, there are only a few mechanism-based multifunctional molecules reported in the literature, including the development of new carbamate-based selective *h*BChE inhibitors (JMC-3c) with two components:(i) the part of the carbamate that is transferred to the catalytically active Ser198 of *h*BChE and is, therefore, mainly responsible for the duration of action in case of additional interaction with an allosteric site, and (ii) the part also referred to as “carrier” on which the high selectivity over *h*AChE by Michael Decker et al. Also, the carbamate and its hydrolysis product have shown an antioxidant effect.(27, 155)

We aim to generate novel multifunctional potent ChEI that targets key AChE and BChE responsible for the neurotransmitter ACh's metabolic breakdown. Additionally, these compounds are intended to exhibit potent antioxidant properties, modulate the formation of Aβ aggregation, and confer neuroprotective effects, thus serving as disease-modifying therapeutic interventions in managing AD.

RIV is a pseudo-irreversible inhibitor of BChE (IC_{50}= 91 ± 0.40 nM) and a weak inhibitor of AChE (IC_{50}= 6630 ± 0.76 nM), providing only symptomatic relief.(154) Given the key role played by both AChE and BChE in AD pathogenesis, however, RIV is a potent

inhibitor of only BChE. Along with this, oxidative stress, inflammation, and Aβ play a significant role in AD neurodegeneration, while RIV is unable to target these critical hallmarks of AD. Therefore, to address the drawbacks of RIV, we have developed mechanism-based multifunctional cholinesterase inhibitors.

Our previous study reported BMC-13b (**Figure 4.27**), a tryptamine template-based series of molecules that exhibit favorable tolerance towards AChE/BChE and can confer capacity antioxidant properties (156, 157). Literature evidence has shown that the indole moiety of tryptamine exhibits considerable promise as a fragment for advancing targeted anti-amyloid agents (117). In our current design of the series of novel molecules, we have replaced the carbamoyl moiety of RIV with substituted tryptamine to investigate the impact of substituents on binding interactions with the enzyme and multifunctional property (158).

In our present study, we further explored the effects of the chirality of dimethylaminoethylphenol fragments on enzyme inhibition activity. We started with the racemic version, 3-(1-(dimethylamino)ethyl)phenol fragment of RIV. Among the fragments mentioned above, chloro and hydroxy tryptamine analogs, i.e., **14d** and **14e**, exhibited the most potent inhibition of the target enzyme. Further, selected compounds were synthesized utilizing the S-configuration of the RIV fragment ((*S*)-3-(1-(dimethylamino)ethyl)phenol), resulting in the production of compounds **15a-15e**. Among the developed molecules, the 5-hydroxy (5-OH) and 5-chloro (5-Cl) analogs exhibited the highest potency, displaying approximately a two-fold activity enhancement, further confirming our earlier observation. Based on the enzyme inhibition studies, we selected lead compound **15e** and synthesized the corresponding *R*-configuration-generating of **16e**. As anticipated, all the compounds demonstrated significant inhibitory activity against the enzymes.

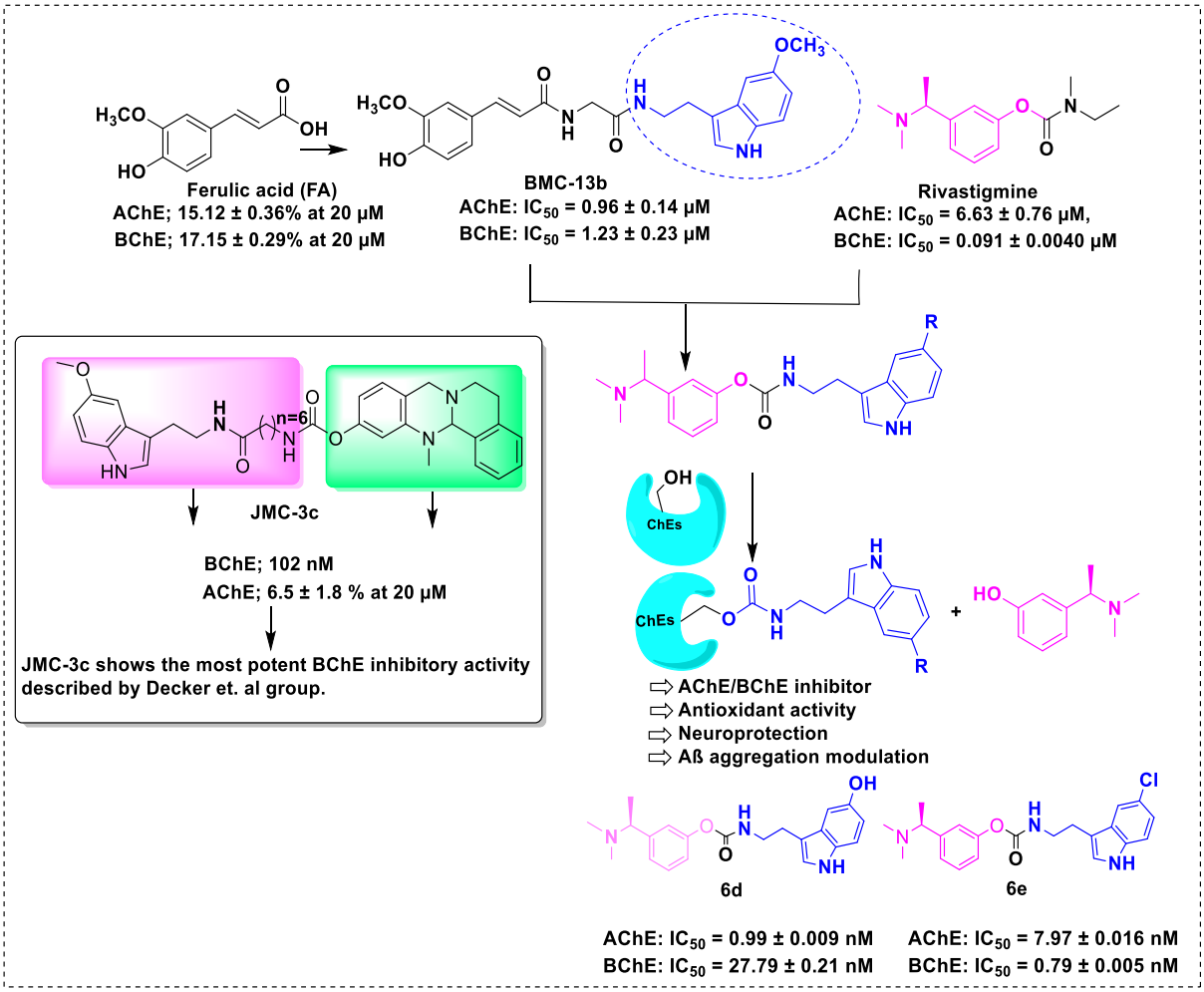

Figure 4.27: Design approach towards synthesizing tryptamine derivatives and role of RIV fragment that can also serve as a template to fine-tune physicochemical properties of the parent compound.

4.5. Chemistry and synthetic schemes involved in the second series of carbamate-based tryptamine derivatives

The synthetic routes for the designed compounds **14a-14e, 15a-15e**, and **16e** are shown in Schemes **5, 6,** and **7**. In **Scheme 5, 6,** and **7**, commercially available 4-nitrophenol chloroformate was reacted with substituted tryptamine (**12a-12e**), using pyridine, as a base in DCM to generate respective carbamate analogs (**13a-13e**) which were utilized in the next step without column purification due to stability issues. In the final step, (**Scheme 5)** reactive carbamate species underwent a nucleophilic substitution reaction with

dimethylaminoethylphenol in the presence of a base in acetonitrile to generate **14a**-**14e**. In **Scheme 6,** intermediates **12a-12e** were reacted with *S*-dimethylaminoethylphenol, using pyridine to generate respective carbamate analogs (**15a**-**15e**). Compound **16e** was synthesized by reacting intermediate **12e** with *R*-dimethylaminoethylphenol in the presence of pyridine as a base. All compounds were purified by column chromatography and characterized using ^{1}H, ^{13}C NMR, and HRMS.

Scheme 5. Synthetic route of compounds **12a**-**14e**

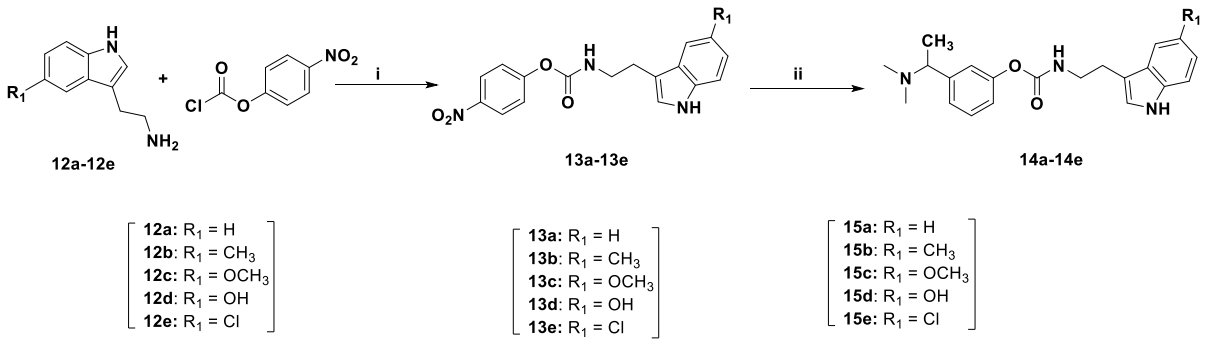

Reagents and conditions: (i) 4-nitrophenol chloroformate, Pyridine, DCM, rt, 2h; (ii) dimethylaminoethylphenol, triethylamine, acetonitrile, 80 ^{o}C, 2h; 60-65%.

Scheme 6. Synthetic route of compounds **15a**-**15e**

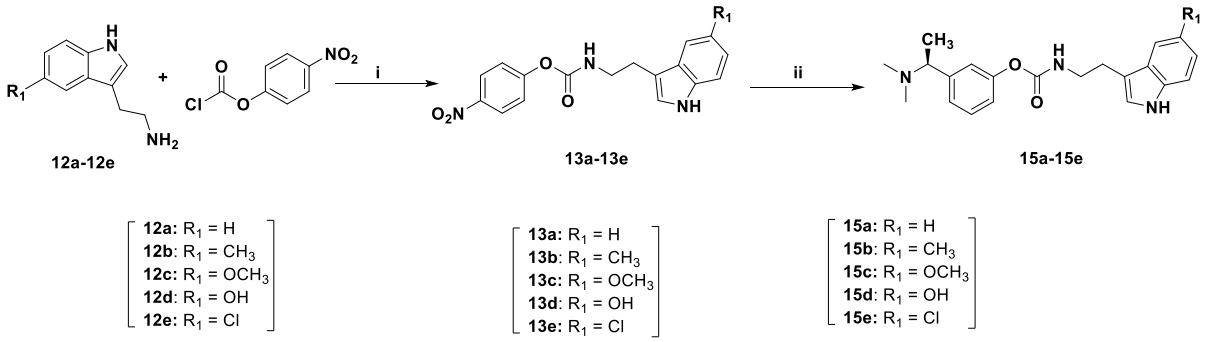

Reagents and conditions: (i) 4-nitrophenol chloroformate, Pyridine, DCM, rt, 2h; (ii) *S*-dimethylaminoethylphenol, triethylamine, Acetonitrile, 80 ^{o}C, 2h; 60-65%.

Scheme 7. Synthetic route of compound **16e**

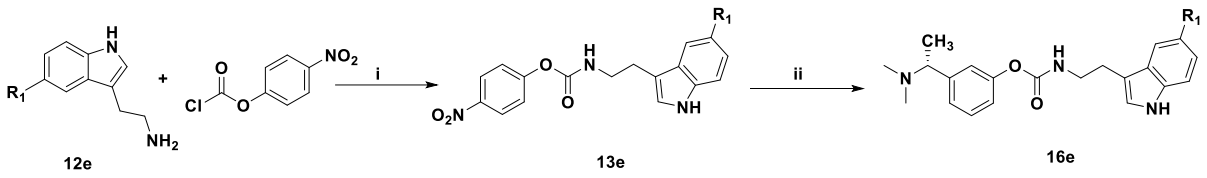

Reagents and conditions: (i) 4-nitrophenol chloroformate, pyridine, DCM, rt, 2h; (ii) *R*-dimethylaminoethylphenol, triethylamine, acetonitrile, 80 ^{o}C, 2h; 60-65%.

4.6. Biological evaluation of the second series of compounds

4.6.1. Cholinesterase Inhibition Studies

In clinical applications, it is established ChE inhibitors represent an efficacious therapeutic approach for enhancing learning and memory and mitigating cognitive decline in AD patients. Therefore, inhibiting ChEs to elevate ACh levels is vital for AD treatment. Consequently, the AChE and BChE inhibitory activities were assessed using the Ellman spectrophotometric method, employing AChE from humans and BChE from equine serum. Positive reference standards, such as RIV (RIV), a well-recognized ChE inhibitor, were used. The assay results are expressed as IC_{50} values (nM), representing the inhibitor concentration that reduces ChE inhibitory activity by 50% (148).

The development of potent cholinesterase (ChE) inhibitors commenced with the substituted tryptamine pharmacophore as the foundational template. We started with the racemic derivative, 3-(1-(dimethylamino)ethyl)phenol fragment of RIV. Our initial investigation focused on synthesizing and evaluating enzyme inhibition properties of the unsubstituted tryptamine derivative **14a**. Interestingly, **14a** exhibited a significant inhibitory effect on BChE with an IC_{50} of 14.82 ± 0.12 nM and AChE with an IC_{50} of 24.47 ± 0.21 nM. Next, we explored the impact of small electron donating groups (EDG) $–CH_3$, $-OCH_3$, and -OH by introducing these on the 5th position of the tryptamine ring, generating compounds **3b-**

14d. Interestingly, compound **14d**, featuring 5-OH, exhibited the most substantial inhibition of AChE and BChE, compared to **14a** (IC_{50}, nM, AChE = 2.31 ± 0.24, BChE = 55.76 ± 1.01, respectively). Furthermore, we introduced the electron-withdrawing group (EWG), chloro, on the 5^{th} position of the tryptamine ring, generating compound **14e**. Among the compounds above, chloro tryptamine analog, i.e. **14e**, exhibited the most potent inhibition of the target enzymes (IC_{50}, nM, AChE = 13.79 ± 0.13, BChE = 2.14 ± 0.17, respectively).

In the next series (Scheme 2), five compounds were synthesized with the help of the S-form of the RIV fragment ((*S*)-3-(1-(dimethylamino)ethyl)phenol), leading to the generation of compounds **15a-15e**. It is noteworthy to observe that 5-OH and 5-Cl analogs were found to be most potent with a relatively two-fold increase in the activity (IC_{50}, AChE, nM: **15d**= 0.99 ± 0.009, **15e** = 7.97 ± 0.016), and BChE (IC_{50}, nM: **15d** = 27.79 ± 0.21, **15e** = 0.79 ± 0.005), respectively. Based on enzyme inhibition studies, we identified lead compound **15e** from the aforementioned series, bearing the R-configuration of the RIV fragment ((*R*)-3-(1-(dimethylamino)ethyl)phenol), to evaluate its impact on enzyme inhibition. The synthesized compound **16e** significantly demonstrated comparable AChE/BChE inhibitory potency to the racemic fragments. Compounds **15d** and **15e** were found to be potent AChE/BChE inhibition over the standard marketed RIV. These results collectively suggested that both EWG and EDG on tryptamine moiety are well tolerated on enzymes. The SAR on this series of all developed molecules is represented in **Table 9**.

Table 9. AChE and BChE inhibition studies of the synthesized compounds

Compound code			**IC_{50} (nM)[a]**	
	Structure	**Stereochemistry**	***h*AChE**	***eq*BChE**
14a	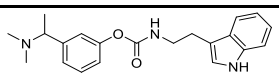	Racemic	24.47 ± 0.21	14.82 ± 0.12

14b	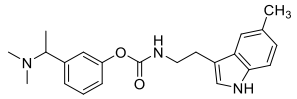	Racemic	73.28 ± 2.03	38.73 ± 0.85
14c	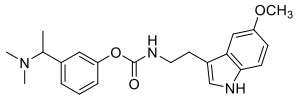	Racemic	48.32 ± 1.70	13.6 ± 0.11
14d	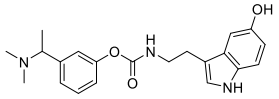	Racemic	2.31 ± 0.24	55.76 ± 1.01
14e	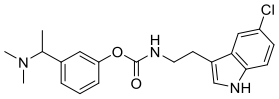	Racemic	13.79 ± 0.13	2.14 ± 0.17
15a	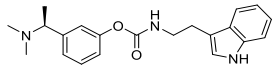	*S*-form	22.16 ± 0.50	11.06 ± 0.14
15b	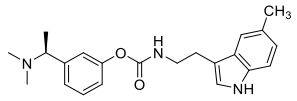	*S*-form	54.73 ± 0.81	26.45 ± 0.29
15c	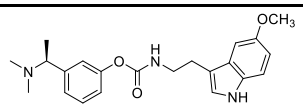	*S*-form	21.44 ± 0.33	3.15 ± 0.23
15d	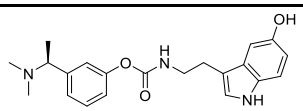	*S*-form	0.99 ± 0.009	27.79 ± 0.21
15e	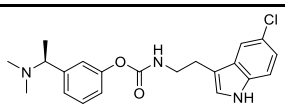	*S*-form	7.97 ± 0.016	0.79 ± 0.005
16a	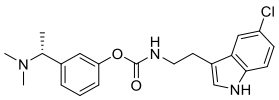	*R*-form	8.38 ± 0.72	7.66 ± 0.56
[b]Riv	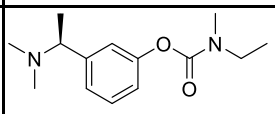	*S*-form	6.63 ± 0.76	0.091 ± 0.40

[a]IC_{50}: 50% inhibitory concentration (mean ± SD of two to three independent experiments).

[b]Riv (RIV) = reference standard.

4.6.2. Enzyme Kinetic studies of *h*AChE and *eq*BChE inhibition

As carbamate-based inhibitors exhibit pseudo-irreversible binding, their IC_{50} values reflect a cumulative parameter influenced by two distinct chemical processes: the transfer of the carbamate group to the enzyme and its subsequent hydrolysis from the enzyme. Therefore, the equilibrium constant for reversible binding (Kc) and the rate constants (k_3) were analyzed for several representative compounds. The mechanism of enzyme inhibition occurs in three distinct steps: Initially, before reaching equilibrium, the carbamate-based inhibitor (C−X) binds reversibly to the enzyme (E), forming a complex (EC−X) that is characterized by the equilibrium constant (Kc). Following this, the carbamate group (C) is transferred onto the enzyme (E), forming a covalent bond to create the E−C complex with a rate constant (k_3), while the carrier moiety (X) is released. To determine K_c and k_3, a comparable experimental approach to the IC_{50} evaluation was employed, where enzyme activity was monitored at different time intervals following the inhibitor's addition.

Table 10. Kinetic Values for Carbamoylation on *h*AChE and *eq*BChE of lead compound **15e**

Compound	**R**	**K_C (nM) & k_3(min^{-1}) against AChE**	**K_C (nM) & k_3(min^{-1}) against BChE**
15e	5-chloro	0.196 ± 0.07; 0.0416 ± 0.002	0.13 ± 0.08; 0.035 ± 0.05

4.6.3. Inhibition of the peripheral anionic site (PAS) of AChE

The AChE enzyme exhibits an affinity for propidium iodide (PI), specifically within the PAS region, with an anticipated impact on modulating Aβ aggregation.(190) In this context, a specific inhibitor of the enzyme competes with PI to displace it from its binding site. The reduction in fluorescence intensity of PI is a robust indicator of the competitive binding of the inhibitor at the PAS site.(191) As illustrated in **Table 11**, at a concentration of 5 µM, **15d** and **15e** caused propidium iodide displacement of 26.25% and 21.87%,

respectively. In comparison, RIV displayed a displacement of 8.74% at the same concentration.

Table 11. Displacement of Propidium Iodide from the PAS of *h*AChE by **15d, 15e,** and **RIV**

Compound	**Concentrations**			
	5 μM (%)	1 μM (%)	0.1 μM (%)	0.01 μM (%)
15d	26.25 ± 0.71	18.29 ± 0.11	5.56 ± 0.61	3.54 ± 0.34
15e	21.87 ± 1.38	20.42 ± 0.10	3.56 ± 0.37	1.37 ± 0.32
[b]RIV	8.74 ± 0.05	6.30 ± 1.59	2.96 ± 0.80	1.61 ± 0.68

The experimental data are the average values with standard deviation (SD) calculated from two independent experiments.

[b]RIV = RIV.

4.6.4. Molecular docking studies

The AChE protein has the PAS & CAS regions as main pockets, and binding in the same pocket justifies the compound's affinity. The binding energies shown by the **15d** and **15e** are -9.95 and -9.58 kcal/mol, higher than the standard RIV -7.92 kcal/mol.

Table 12. Important interactions of compound **15d** & **15e** along with the reference standard **RIV**, with AChE protein (PDB ID: 4EY7).

Compound code	**Binding energies kcal mol^{-1}**	**Interacting residues within 3 Å distance of the binding site**	**Polar interactions**
15d	-9.58	**Pi-PI T shaped:** PHE337(5.13 Å), PHE337(5.30 Å) **Pi-sigma:** TYR340(3.75 Å), TYR336(3.85 Å) **Pi-Pi stacked:** TRP285(4.21 Å), TYR340(5.47 Å) **Pi-alky:** TRP285(4.18 Å), TYR71 (4.40 Å), TRP85 (4.43 Å), HIS446(5.22 Å)	SER292, VAL293, PHE294, PHE337, PHE296, GLY121, SER202, GLY120, TYR123, ARG295, ASP73

15e	-9.95	**Pi-PI T shaped:** TYR123 (5.77 Å), TYR336 (5.13 Å) **Pi-sigma:** TRP85 (3.39 Å) **Pi-Pi stacked:** TRP285 (4.04 Å), TRP285 (4.80 Å), TRP285 (5.17 Å), TYR340 (4.67Å), TYR340 (4.86 Å) **Pi-alky:** TRP85 (4.93 Å) **Pi cation:** HIS446 (4.76 Å) **Hydrogen bond:** TYR123 (1.77 Å)	SER202, GLY120, GLY121, PHE296, PHE337, PHE294, ARG295, VAL293, SER292, TYR71
RIV	-7.92	**Pi-sigma:** TRP285 (3.57 Å) **Pi-Pi stacked:** TYR340 (3.76 Å) **Pi-alky:** TYR340 (4.78), TYR123 (5.01 Å), TYR71 (5.15 Å), TRP285 (4.66 Å), VAL293 (4.71 Å) **Hydrogen bond:** ARG295 (2.13 Å)	PHE337, LEU288, PHE294, SER292, TYR336, ASP73, PHE296

This suggests better occupancy of the pocket of AChE and can lead to potent *in-vitro* activity. The *in-vitro* results substantiate the computational studies. The detailed interactions are mentioned in **Table 12** and **Figure 4.28,** indicating different poses in a 2D & 3D manner. The interactions with amino acids like TYR71, having π–π interactions with the fused ring in the compound, indicate a strong bond with the protein**,** as these differ from conventional hydrogen bonding and van der Waals forces. Based on the docking data, it is evident that the compounds can interact with substantial amino acid residues and fit well in the active site of the AChE. The compounds also occupied the acyl binding pocket & oxyanion hole of the protein, as the interactions are seen with PHE296 & PHE297 and GLY120 & GLY121, respectively. This indicates that the compound may occupy the cavity, presenting PAS & CAS sites.

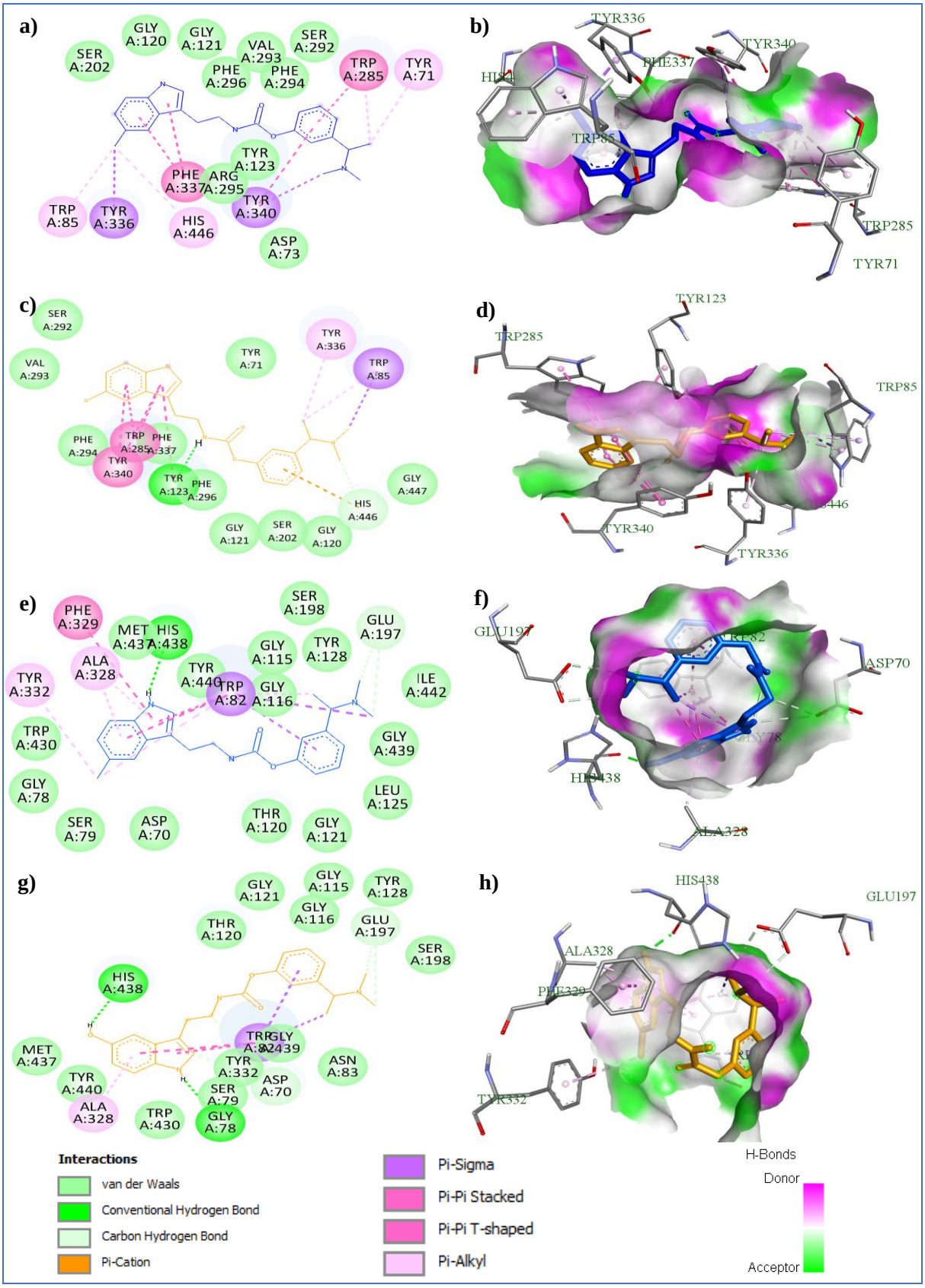

Figure 4.28: 2D and 3D docking interactions of **15d** and **15e** against AChE and BChE protein.

Like the AChE protein, the BChE docking study also suggests better binding energies of **15d** and **15e** (-8.91 and -9.04 kcal/mol) than the standard RIV (-6.84 kcal/mol).

Table 13. Important interactions of compound **15d** & **15e** along with the reference standard **RIV,** with BChE protein (PDB ID: 4BDS).

Compound code	Binding energies kcal mol^{-1}	Interacting residues within 3 Å distance of the binding site	Polar interactions
15d	-9.04	**Pi-PI T shaped:** PHE329 (5.62 Å), TRP82 (4.15 Å), TRP82 (5.57 Å) **Pi-sigma:** TRP82 (3.67 Å), TRP82 (3.78 Å) **Pi-alky:** TRP82 (4.91 Å), TRP82 (4.52 Å), TYR332 (5.44 Å), ALA328 (4.44 Å), ALA328 (3.59 Å) **Hydrogen bond:** HIS438 (2.11 Å)	ASP70, SER79, GLY78, TRP430, MET437, TYR440, GLY116, GLY115, SER198, TYR128, GLU197, ILE442, GLY439, LEU125, GLY121, THR120
15e	-8.91	**Pi-PI T-shaped:** TRP82 (4.31 Å) , TRP82 (4.18 Å) **Pi-sigma:** TRP82 (3.90 Å), TRP82 (3.94 Å) **Pi-alky:** ALA328 (4.13 Å) **Hydrogen bond:** HIS438 (1.84 Å), GLY78(2.37 Å)	MET437, TYR440, SER79, TYR332, ASP70, ASN83, GLY439, SER198, GLY116, GLU197, GLY115, TYR128, GLY121, THR120, TRP430
RIV	-6.84	**Pi-PI T shaped:** HIS438 (4.81 Å), TRP82 (5.24 Å) **Pi-alky:** TRP82 (4.55 Å), TRP82 (4.73 Å), ALA328 (5.18 Å), TYR332 (4.87 Å), TRP430 (4.30 Å) **Pi cation:** HIS438 (4.61 Å) **Hydrogen bond:** TRP82 (1.92 Å), TRP430 (2.33 Å), TYR440 (1.88 Å)	TYR128, GLY115, ILE442, GLU197, GLY439, GLY116, TYR440, ASP70, GLY78, SER79, PHE329, MET437

The detailed interactions are shown in **Table 13** and **Figure 4.28,** indicating the 2D & 3D interactions of the compounds and standard drug with the protein. The interactions of both compounds are similar to those of important amino acid residues like ALA328 & TRP82, which show the π–π T-shaped and π-sigma bond interactions. These are known for hydrophobic interactions and can bond strongly with the protein. Other H-bond and polar

interactions are also observed compared to the standard **RIV**, which suggests better binding of the compounds and produces better binding energies than **RIV**.

4.6.4.1. Covalent docking

This study employed a covalent docking approach to elucidate the binding mechanisms of **RIV, 6d** and **6e**. All three molecules docked at their respective binding sites in the AChE and BChE proteins. The binding energies of compounds **15d** and **15e** in AChE were -6.713 and -3.270 kcal/mol, respectively, whereas the binding energy for the standard **RIV** was -6.490 kcal/mol. Additionally, the BChE docking studies revealed that **15d** and **15e** exhibited superior binding energies of -9.051 and -8.460 kcal/mol, respectively, compared to the standard RIV (-5.769 kcal/mol).

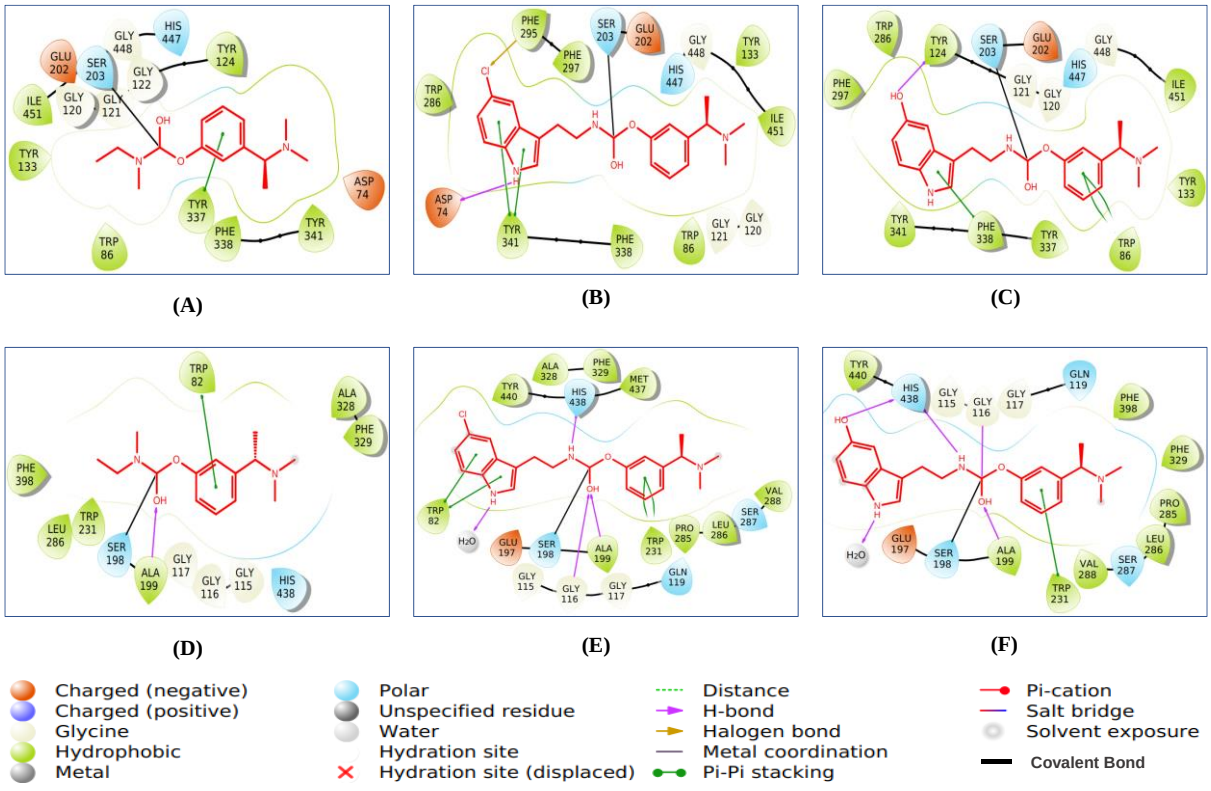

Figure 4.29: 2D interaction diagrams showing the binding of RIV, **15d** and **15e** with AChE and BChE: (A) **RIV** with AChE, (B) Compound **15d** with AChE, (C) Compound **15e** with AChE, (D) **RIV** with BChE, (E) Compound **15d** with BChE, and (F) Compound **15e** with

BChE; The green line denotes π–π stacking interactions, magenta arrow indicates hydrogen bonds, the black line represents covalent bonds, and the yellow arrow depicts halogen bonds.

Figures 4.29 and **4.30** indicate the 2D and 3D interactions of the compounds **15d**, **15e** and standard **RIV** with the protein. Each molecule formed both non-covalent and covalent interactions with AChE and BChE proteins. However, primary emphasis was given to the covalent interactions. RIV was observed to form π–π stacking interactions with Tyr337 and a covalent bond with SER203 in AChE (**Figure 4.30A**). In BChE, RIV exhibited π–π stacking interactions with Trp82, a hydrogen bond with ALA199, and a covalent bond with SER198 (**Figure 4.30D**). Similarly, compounds **15d** and **15e** formed covalent bonds with SER203 in AChE (**Figure 4.30B, C**) and SER198 in BChE (**Figure 4.30E, F**). This study demonstrates that all three molecules, including RIV, exhibit covalent binding to AChE and BChE proteins.

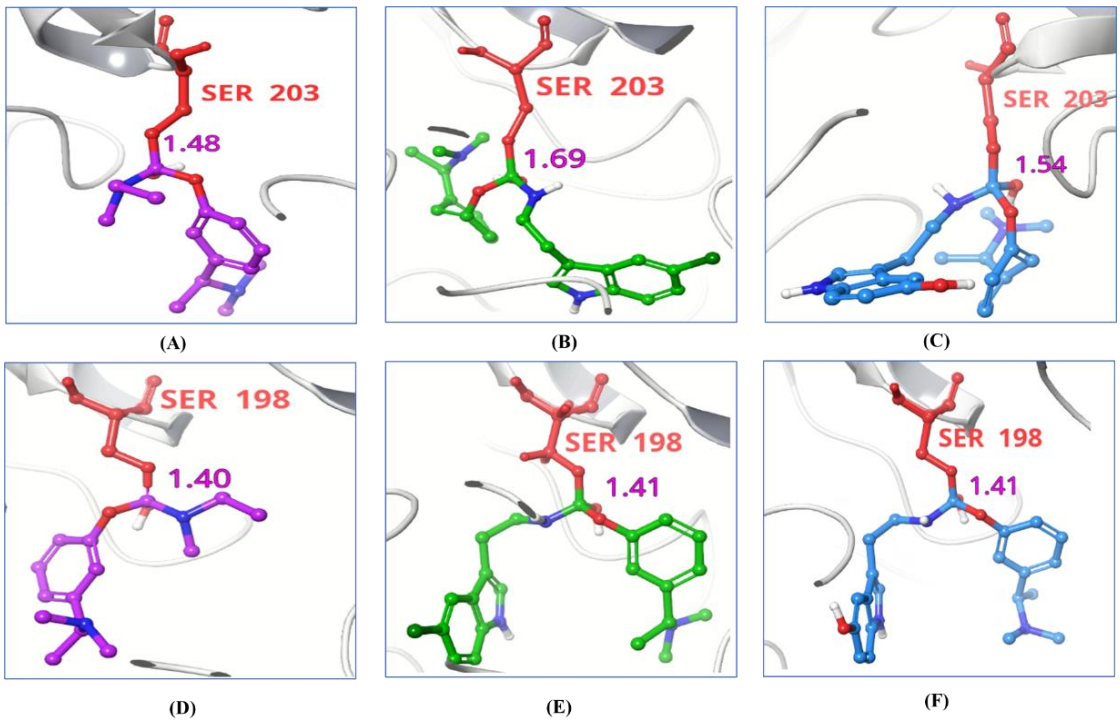

Figure 4.30: 3D interaction diagrams showing the binding of **RIV**, **15d** and **15e** with AChE and BChE: (A) **RIV** with AChE, (B) Compound **15d** with AChE, (C) Compound **15e** with

AChE, (D) **RIV** with BChE, (E) Compound **15d** with BChE, and (F) Compound **15e** with BChE; The distance is given in Angstroms highlighted in magenta color.

4.6.5. Molecular dynamics studies

4.6.5.1. Molecular dynamics trajectory analysis of 15d and 15e against AChE and BChE complex

We performed an MD simulation for 200 ns using the GROMACS software to understand the protein and ligand interactions better. In MD simulations, RMSD (Root Mean Square Deviation) is a commonly used metric to assess the structural deviation of a simulated molecular system from a reference structure over time. Molecular dynamics simulations involve numerically solving the classical equations of motion for a set of interacting atoms or particles, allowing the study of the dynamic behavior of molecular systems. The ligand's root mean square deviation (RMSD) is illustrated in **Figure 4.31A**, which exhibits fluctuations within the range of 0.3 to 0.6 nm. These fluctuations initially demonstrated the transient variations in the first few nanoseconds, followed by sustained stability for the remainder of the 200-ns simulation period. The RMSD of the ligand, as illustrated in **Figure 4.31B**, exhibited fluctuations within the range of 0.4 to 0.7 nm. These fluctuations initially demonstrated transient variations in the first few nanoseconds, followed by sustained stability for the remainder of the 200-ns simulation period. The RMSD of protein in (**Figure 4.31C**) fluctuates between 0.3 to 0.6 nm, showing initial flotations for the first few nanoseconds, then remaining stable for the rest of the simulation period. The Root Mean Square Deviation (RMSD) of the protein, as depicted in **Figure 4.31D**, exhibited fluctuation within the range of 0.3 to 0.7 nanometers. Notably, initial fluctuations are observed in the first few nanoseconds, followed by sustained stability for the remaining duration of the simulation period. This behavior suggests transient variations in the initial phase, stabilizing the protein conformation throughout the simulation.

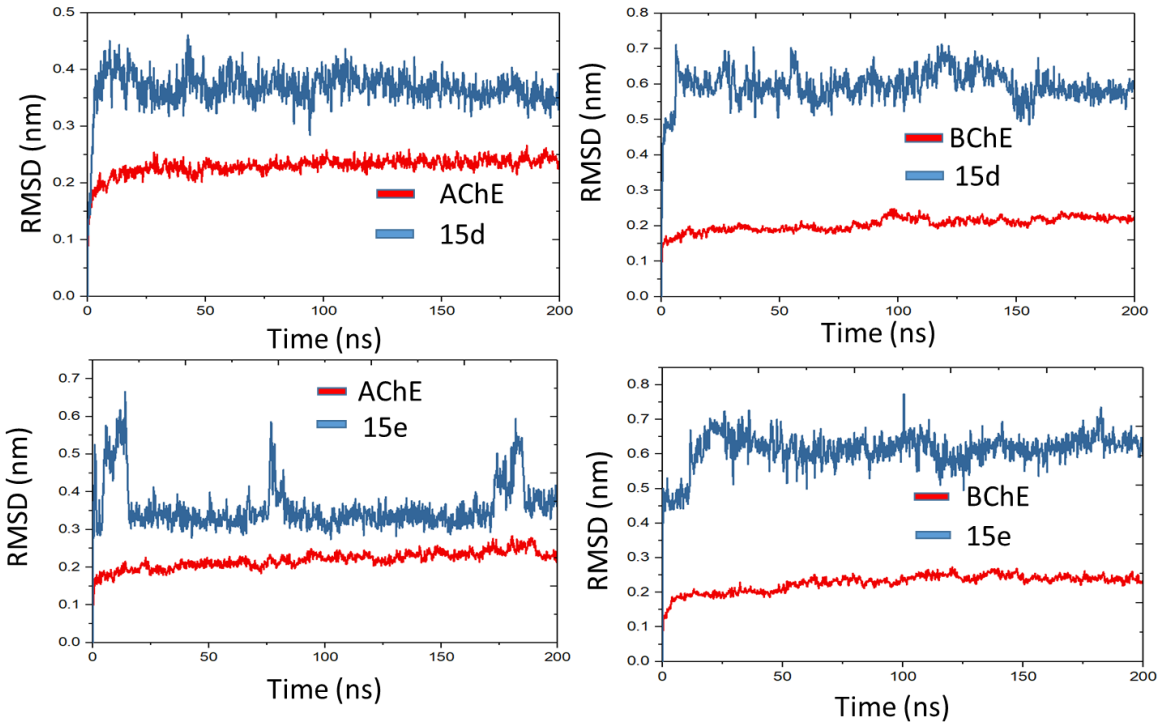

Figure 4.31: Molecular dynamics trajectory analysis of compounds **15d** and **15e** with AChE and BChE complex.

4.6.6. Evaluation of the antioxidant property

The existing literature has greatly emphasized the pivotal role of oxidative stress (OS) in advancing AD.(192) Hence, a more efficacious approach for AD treatment would involve not only the inhibition of ChEs but also the ability to alleviate oxidative stress.(193) The antioxidant capacity of the synthesized molecules was assessed through the 2,2-Diphenyl-1-(2,4,6-trinitrophenyl) hydrazine (DPPH) assay.(194) Seven newly developed compounds were chosen based on their cholinesterase inhibition activity. All tested compounds demonstrated a range of moderate to significant antioxidant activity, with the percentage of radical scavenging activity spanning from 88.32% to 19.81% (**Table 14** and **Figure 4.32**). Compound **15d** manifested superior radical scavenging activity, reaching 93.05%, surpassing all other molecules examined in this series. Our investigation underscores a substantial amplification in the antioxidant efficacy of the compounds in contrast to RIV, a commercially available drug exhibiting a modest activity of 3.71%.

Table 14. Antioxidant activity (DPPH assay) of **14e, 14c, 15d, 15e,** ascorbic acid and **RIV**.

Compound	Racemic or S-form	R	IC_{50}[a] (µM)/ % Radical scavenging[b]
14e	Racemic	5-chloro	33.33 ± 0.73
14c	S-form	5-methoxy	19.81 ± 2.80
15d	S-form	5-hydroxy	22.91 ± 1.73 µM
15e	S-form	5-chloro	38.93 ± 2.16
Ascorbic acid[c]	------	------	3.51 ± 0.35 µM
RIV	S-form	------	3.71 ± 0.09

All the values were obtained at a concentration of 200 μM,

[a]IC_{50}: 50% inhibitory concentration (mean ± SD of three independent experiments).

[b]% Radical scavenging activity

[c]**RIV** = used as standard drug for comparison.

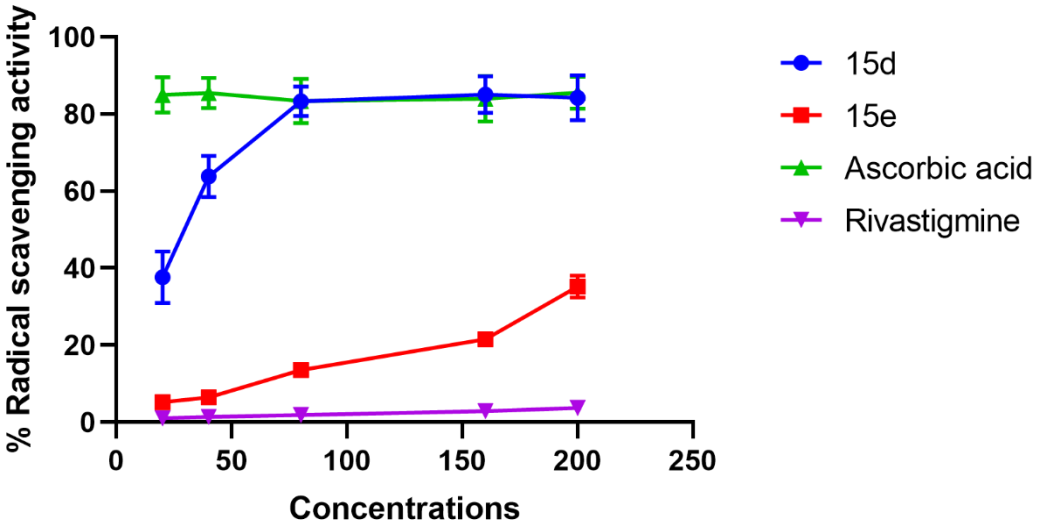

Figure 4.32: Graphical representation of % Radical scavenging activity of lead compound **15d, 15e** and marketed drug **RIV**.

4.6.7. *In-vitro* cytotoxicity assessment

4.6.7.1. Cell cytotoxicity assessment of 15d and 15e in PC-12 cell line

Assessing cytotoxicity constitutes a fundamental stride in drug development, with preliminary *in-vitro* inquiries antedating *in-vivo* investigations.(195) Compounds **15d** and **15e** were selected based on the potent inhibitory activity against AChE/BChE and antioxidant properties. PC12 cells are widely employed as an optimal cellular model for pioneering therapeutic strategies in AD (196).

Phenotypically, undifferentiated PC12 cells have a polygonal shape; however, when incubated with a differentiating medium with nerve growth factor (NGF), PC12 cells differentiate into sympathetic neuron-like cells, extending neurites and forming a neural network. Differentiated PC12 is a cell line characterized by its sympathetic neuronal cell properties- morphologically, physiologically, and biochemically. Additionally, differentiated PC12 exhibits increased expression of cholinergic receptors, choline acetyltransferase, and AChE activity. Consequently, differentiated PC12 cells have been used as a standard cellular model for AD research. In this study, we have extensively used differentiated PC12 cells to study the neuroprotective effect of novel compounds for AD therapeutics

Consequently, all experimental procedures in this study were conducted utilizing differentiated PC12 cells. For assessing the cytotoxicity of compounds **15d** and **15e**, PC12 cells were exposed to varying concentrations (0.1, 1, 2.5, 5, 7, 10, 15, and 20 µM) of **15d** and **15e** for 24 hours (**Figure 4.33**) and cell viability was calculated using the 3-(4,5-dimethylthiazol-2-yl)-2,5-diphenyltetrazolium bromide (MTT) assay. The outcomes revealed that **15d** and **15e** exhibited no sign of cytotoxicity in PC-12 cells at concentrations up to 20 µM.

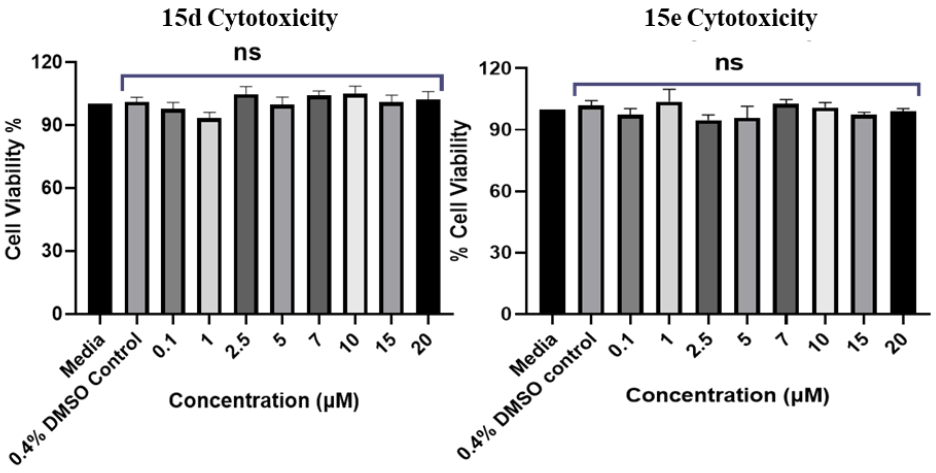

Figure 4.33: The impact of **15d** and **15e** on cellular viability. The cells were subjected to varying concentrations of **15d** and **15e** (0.1, 1, 2.5, 5, 7, 10, 15 and 20 μM) for 24 hours. The MTT assay was utilized to analyze cell viability, expressed as a percentage. ns = nonsignificant vs 0.4% DMSO Control. The data are processed by one-way ANOVA followed by Dunnett's multiple comparison test. All assays were performed using samples in quadruplicate in three independent experiments and presented as mean ± SE.

4.6.7.2. Assessment of neuroprotective effects against H_2O_2-induced neurotoxicity in PC-12 cell

Hydrogen peroxide (H_2O_2) has been reported to be an important cause of reactive oxygen species (ROS) and has been linked to several neurodegenerative diseases that exacerbate over time.(196) Therefore, to assess the neuroprotective potential of investigated compounds in *in-vitro* experimental research, H_2O_2-induced cytotoxicity in PC12 cell lines was used as an in vitro oxidative stress model. The different concentrations (20, 15, 10, 7, 5, 2.5, and 1 μM) of **15d** and **15e** were used based on our previous publication, and cells were pre-treated with these concentrations for 24 hrs. After 24 hours, cells were subjected to oxidative stress using H_2O_2 (600 μM). **Figure 4.34A-B** indicates that **15d** and **15e** can ameliorate the PC12 cell viability at all tested concentrations (1-20 μM) of H_2O_2.

Furthermore, compounds **15d** and **15e** demonstrated neuroprotective effects, highlighting compounds **15d** and **15e** anti-oxidative properties.

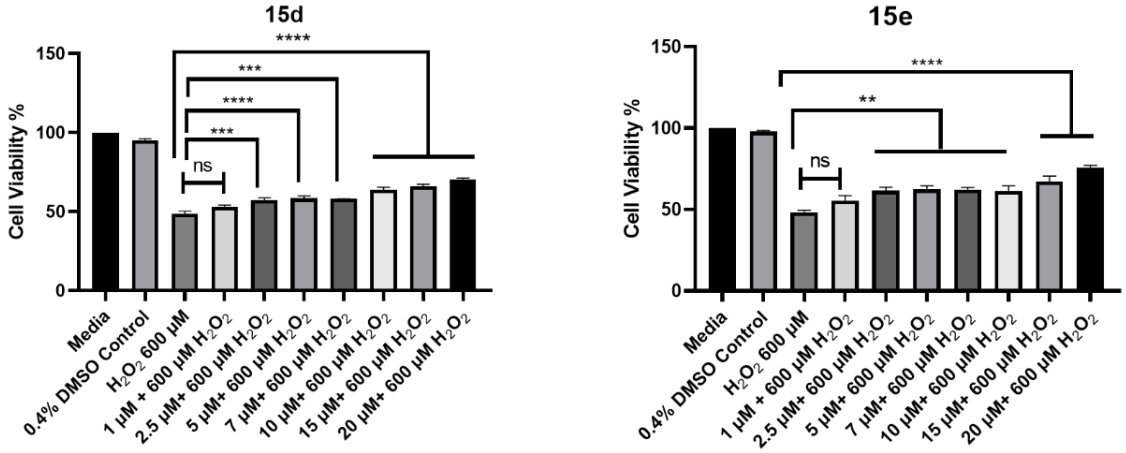

Figure 4.34: Cells were pre-incubated with **15d** (A) and **15e** (B) at 1, 2.5, 5, 7,10, 15, or 20 µM for 24 h and then further incubated with 600 µM H_2O_2 for another 24 h. Cell death was assessed by MTT assay. The data are processed by one-way ANOVA followed by Dunnett's multiple comparison test. All assays were performed using samples in quadruplicate in three independent experiments and presented as mean ± SE.

4.6.7.3. Exploring the impact of neuroprotective compounds 6d and 6e on apoptosis.

Programmed cell death, or apoptosis, is a fundamental biological process whose dysregulation contributes to the development of several neurological diseases.(197) Propidium iodide (PI) and annexin V-FITC staining of PC12 cells were used to assess apoptosis using flow cytometry. Apoptotic cell detection is commonly achieved by measuring the externalization of phosphatidylserine from the plasma membrane using fluorescently labeled annexin V. While PI stains cells during the late or necrotic stage of apoptosis, annexin V stains cells in both the early and late phases of apoptosis (198).

To evaluate the impact of the neuroprotective **15d** and **15e** on PC12 cells, cells were seeded at a density of 1x10^5 cells/well in a 6-well plate. Subsequently, the cells were treated with **15d** and **15e** at concentrations of 20 µM, 10 µM, 5 µM, and 1 µM for a 24-hour incubation period. A set of apoptosis-inducing H_2O_2 controls and untreated controls were used for the experiment. **Figure 4.35A-D** illustrates distinct frequencies of live/viable cells and apoptotic or necrotic cells. In the untreated control plot **Figure 4.35A**, the frequency of viable cells and those undergoing apoptosis is 82.8%. The apoptosis control treated with H_2O_2 exhibited only 42.9% live cells, an approximately two-fold decrease in the frequency of the live cell population in comparison to the untreated control **Figure 4.35B**. The induction of H_2O_2 in PC12 cells prompted apoptosis. Subsequently, PC12 cells were subjected to incubation with varying concentrations of **15d** and **15e** (20 µM, 10 µM, 5 µM, and 2.5 µM) for 24 hours, followed by the apoptosis induction using 600 µM H_2O_2. An increase in cell viability was observed in the group treated with the **15d**, and the percentages for live cells were recorded as 81.5% (20 µM), 53.3% (10 µM), 81.1%(5µM), and 6.82% (2.5 µM) **Figure 4.35C**. Similarly, frequencies of viable cells treated with **15e** were 80.7% (20 µM), 63.3% (10 µM), 71.3% (5µM) and 65.9 (2.5µM) **Figure 4.35D**. Based on observations, it has been determined that increasing the concentration of **15d** and **15e** beyond 20 µM elicits a significant augmentation in neuroprotective efficacy.

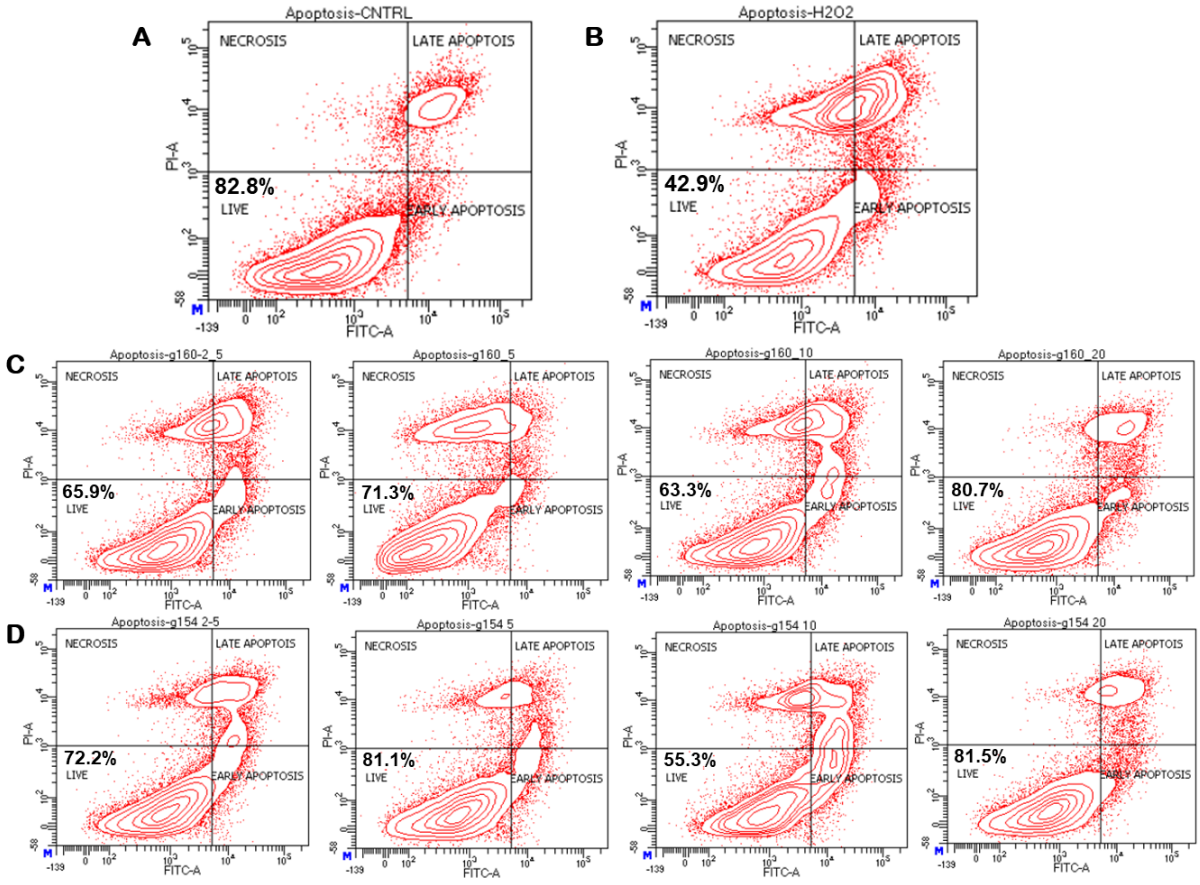

Figure 4.35: The effect of neuroprotective compounds **15d** and **15e** on apoptosis (A) the flow plot showing the frequency of different subpopulations of untreated control and H_2O_2 control, (B) the flow plot showing the frequency of different subpopulations of **15d** (C) and **15e** (D) at 20 µM, 10 µM, 5 µM, and 1 µM for 24 h and followed by cells were induced with 600 uM H_2O_2.

4.6.8. Evaluation of the metal chelation property

Research has indicated that imbalances in brain biometals such as iron (Fe) and copper (Cu) can play a role in AD development (199). To delve into the interaction between the potent cholinesterase inhibitors **15d**, **15e** and Fe (III) species, we conducted a metal chelation study with $FeCl_3$ and $CuSO_4$. The absorbance spectra of **15d**, **15e** alone, and **15d, 15e** with $FeCl_3$ and $CuSO_4$ were recorded using a UV spectrophotometer across a 200-700 nm range. The findings are depicted in **Figure 4.36.** It is evident that upon incubation with

one equivalent of $FeCl_3$ and $CuSO_4$ at a concentration of 300 µM, there was no noticeable enhancement in absorption intensity nor the emergence of any additional peaks throughout the spectral range. This outcome suggests that the compounds **15d** and **15e** did not effectively chelate iron and copper.

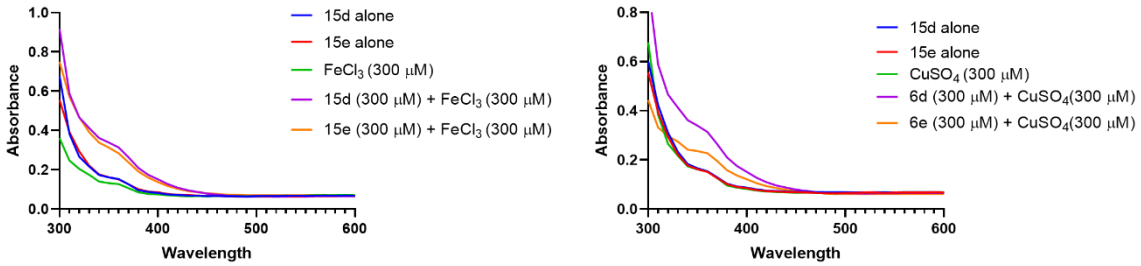

Figure 4.36: UV-visible spectroscopic scanning of a solution containing 300 µM of **15d** and **15e** alone in methanol or combined with 300 µM of $FeCl_3$ and $CuSO_4$ at pH 7.4, covering the 300-550 nm range. The experiment was carried out with two independent experiments.

4.6.9. *In-vitro* blood-brain barrier permeation assay

When developing drugs for AD, it is crucial to consider the drug compounds' ability to take into account the ability of the drug compounds to pass through the BBB. The BBB acts as a protective barrier, restricting the entry of substances into the brain. A PAMPA assay was performed to evaluate the potential permeability of compounds **15d** and **15e** across the BBB. This assay is specifically designed to assess the ability of compounds to cross the BBB and enter the brain (200). This assay provides important insights into the BBB permeability of these compounds, providing valuable information for further assessment. We initially compared the permeability of two commercially available drugs with their reported values to validate the experiment. The outcomes are illustrated in **Table 13**, which showcases the permeability values (*Pe*) of compounds **15d** and **15e**. Based on the criterion set by Di et al., compounds with a permeability value (*Pe*) exceeding 4.0 can be categorized as having high BBB permeability (CNS+). In contrast, compounds with *Pe* values below 2 are anticipated to

have low BBB permeability (CNS) (201). The evaluation of the newly synthesized compounds using the PAMPA-BBB assay revealed that compounds **15d** and **15e** had a permeability value (*Pe*) exceeding 4.0, and exhibited the same characteristic (as indicated in **Table 15**). These results suggest that both compounds can traverse the blood-brain barrier within the brain.

Table 15. The permeability (Pe) of **15d**, **15e**, **Testosterone**, and **Norfloxacin** was determined in the PAMPA assay and was expressed in $Pe = 10^{-6}$ cm s^{-1}.

S.No.	compound	P_e (exp)	Reference values	Prediction
1.	**Testosterone**	17.40 ± 0.22	17.0	CNS (+)
2.	**Norfloxacin**	0.12 ± 0.02	0.1	CNS (-)
3.	**15d**	11.53 ± 1.16	------	CNS (+)
4.	**15e**	12.97 ± 0.38	------	CNS (+)

Reference values were taken from Di Li *et al* (187, 200). CNS (+), $P_e > 4.0$, high permeability; CNS (-), Pe < 2.0, low permeability; CNS (±), $4.0 > P_e > 2.0$, uncertain permeability. The experiment was carried out in duplicate, and data are presented as mean ± SD.

4.6.10. Evaluation of $A\beta_{1-42}$ aggregation inhibition property

$A\beta_{1–42}$ represents an amphipathic peptide with a propensity for self-association, forming oligomers that exhibit cytotoxicity. This peptide's aggregation culminates in the generation of amyloid fibrils, known for their affinity to Congo red and thioflavin-T (ThT) dyes. ThT is a prevalent histological dye for tracking beta-structures' emergence within proteins. This dye selectively engages with cross-β structures, undergoing secondary structural conversions into β-structures (202). The assessment of ThT fluorescence proves to be a valuable technique for probing the kinetics of amyloid aggregation formation in proteins.

The involvement of the $A\beta_{1-42}$ peptide in the development of AD is well-established, and inhibiting its aggregation can alter the course of the disease. Consequently, we were keen to investigate the aggregation inhibitory potential of **15d** and **15e**, the most potent compound in this series, against the aggregation of $A\beta_{1-42}$. Understanding its effectiveness could shed light on its potential therapeutic benefits in AD. To investigate the inhibitory effects of **15d** and **15e** on the aggregation of $A\beta_{1-42}$, we carried out ThT assay. $A\beta_{1-42}$ peptide solution, at a final concentration of 6.25 µM, was incubated alone or in a 4:1 ratio with **15d** and **15e** (final concentration of 1.562 µM). The incubation was carried out at 37 °C with agitation at 1200 rpm for 3 days. The aggregation of $A\beta_{1-42}$ was monitored using the ThT experiment. The results obtained from the ThT assay provide clear evidence that **15d** and **15e** can fully inhibit the aggregation of $A\beta_{1-42}$ protein following a 3-day incubation period **(Figure 4.37).**

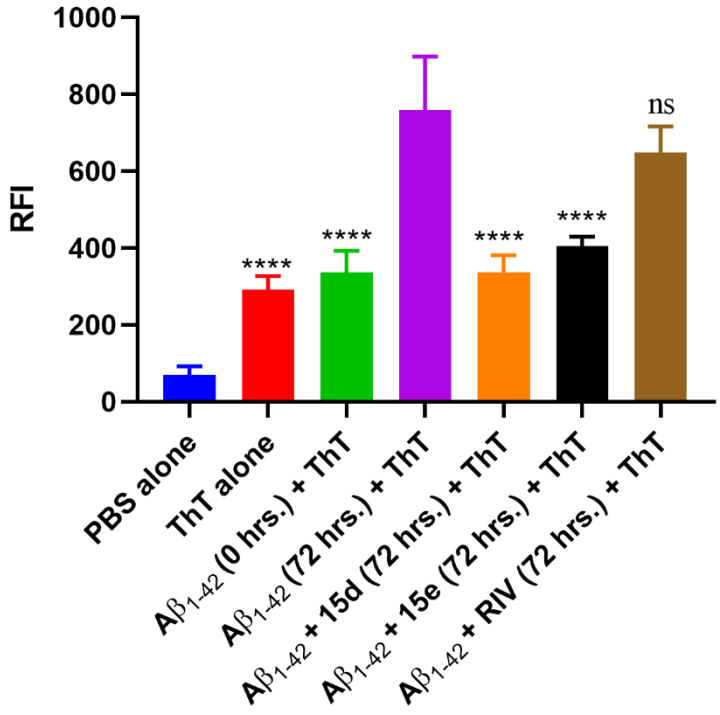

Figure 4.37: Inhibition of self-induced $A\beta_{1-42}$ aggregation in the presence of **15d** or **15e.** $A\beta_{1-42}$ monomer (6.25 µM, final concentration) in the presence of **15d** (1.512 µM). Incubate the mixture for 72 hrs. followed by adding ThT (50 µM) at 37 °C for 30 min at 300 rpm in an

Eppendorf thermomixer. ****p < 0.0001, ns = nonsignificant vs $A\beta_{1-42}$ + ThT (72 hrs.). The experiment was carried out in duplicate data and analyzed by one-way ANOVA followed by Dunnett's multiple comparison test.

Subsequently, we conducted transmission electron microscopy (TEM) imaging to investigate the inhibition of $A\beta_{1-42}$ in the presence of compounds **15d** or **15e**, maintaining a 1:4 molar ratio. As illustrated in **Figure 4.38**, $A\beta_{1-42}$ samples exhibited distinct morphological differences in the absence and presence of compounds **15d** or **15e**. Specifically, $A\beta_{1-42}$ and **RIV** samples revealed the presence of oligomers and small fibers, while amorphous structures were observed in the presence of compounds **15d** or **15e**. This observation suggests compounds **15d** and **15e** effectively impede $A\beta_{1-42}$ aggregation.

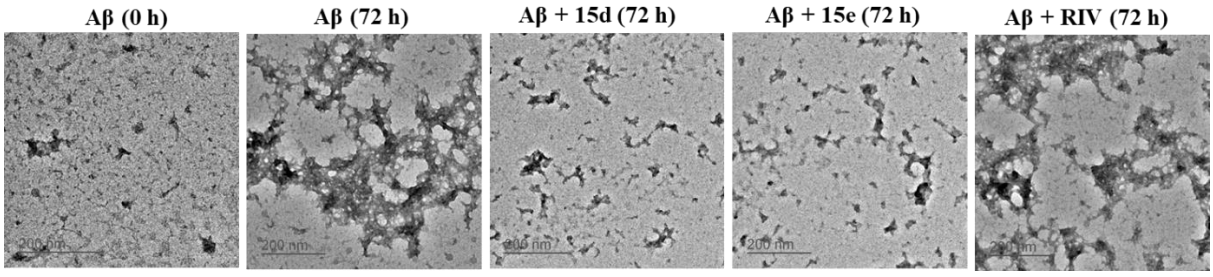

Figure 4.38: Morphological evaluation of $A\beta_{1-42}$ by TEM imaging in the absence and presence of compounds **15d** or **15e**.

4.6.11. Computational investigation of 15d and 15e interaction with $A\beta_{1-42}$ fibrils

Utilizing computational tools such as molecular docking and molecular dynamics (MD) simulations, we investigated the binding interactions of **15d** and **15e** with the $A\beta_{1-42}$ protofibril. Molecular docking analysis explored the binding sites and interaction profiles between these small molecules **15d** and **15e** with $A\beta_{1-42}$ protofibrils (PDB ID 2BEG), utilizing a customized version of Autodock Vina. Notably, both molecules exhibited binding at multiple sites. For further investigation, we selected the pocket with the highest frequency of docked conformations; intriguingly, these pockets also displayed the lowest docking scores.

15d demonstrated interactions with chain E and chain D residues of protofibrils, scoring -7.3 kcal/mol, while **15e** interacted with chain A, chain B, and chain C, scoring -7.6 kcal/mol. Furthermore, **15d** engaged in a π–π stacking interaction with Phe19 of chain E and formed three aromatics hydrogen bonds with Phe19 (chain D), Val18 (chain D) and Leu17 along with hydrophobic interactions involving residues Leu17, Val18, and Phe19 from chains B, C, D, and E **(Figure 4.39a and Figure 4.39c).** Conversely, **6e** exhibited a hydrogen bond interaction with Val36 of chain C and aromatic hydrogen bonds with Phe19 (chain B) and Phe20 (chain A), as well as hydrophobic interactions with residues Phe19, Phe20, Ala21, Val36, and Leu34 from chains A and B, and with Val36 from chain D and Phe19 from chain C **(Figure 4.39b and Figure 4.39d).** Overall, the molecular docking study indicated that both molecules predominantly interacted with chains B, C, D, and E residues of protofibrils through π–π stacking, hydrogen bonds, and hydrophobic interactions.

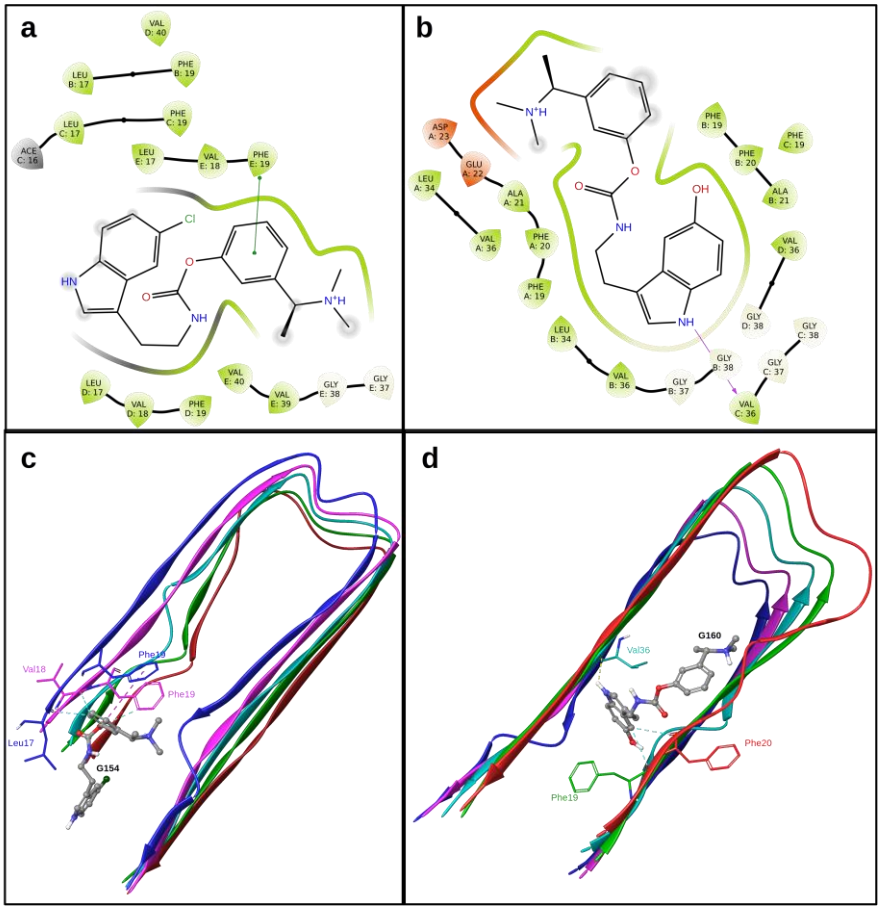

Figure 4.39: (a) 2D interaction diagram of **15d**. A hydrogen bond is shown in the magenta arrow. (b) 2D interaction diagram of **15e**. π–π stacking is shown in a green line. (c) Binding site of **15d** with interacting residues. (d) The binding site of **15e** with interacting residues. Chains A-E shown in red, green, teal, magenta, and blue, respectively. The dotted lines represent hydrogen bonds, π–π stacking, and aromatic hydrogen bonds in yellow, magenta, and sky blue, respectively.

Our docking studies suggested that **15d** and **15e** could modulate the aggregation of $A\beta_{1-42}$ protofibrils via hydrophobic interactions, π–π stacking, and hydrogen bonding. Subsequently, molecular dynamics simulations of protofibril−**15d**, protofibril−**15e**, and protofibrils were conducted for 300 ns at 310 K. The MM-GBSA approach was utilized to calculate the binding free energy between the ligands and the protofibrils, with binding energies computed for the entire trajectory at 100 ps intervals **(Figure 4.40c).**

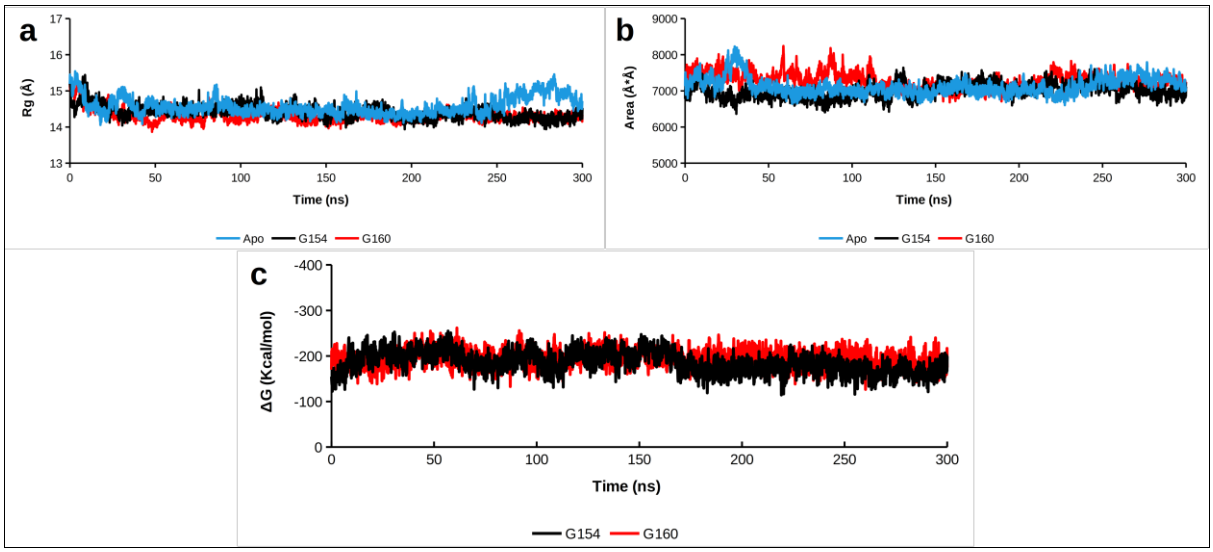

Figure 4.40. (a) The radius of Gyration (b) SASA and (c) Mmgbsa calculated over the trajectories.

The total binding energy for the protofibril−**15d** complex was -185.877 ± 24.081 kcal/mol, whereas for protofibril−**15e**, it was -193.995 ± 19.406 kcal/mol. Analysis of individual residue contributions revealed that residues Phe19 from chains A and E, and Leu34

from chains A and B primarily contributed to the binding interaction between **15d** and the protofibril. Additionally, residues Ile32, Phe20, Leu17, and Val18 from chain A significantly contributed to the binding **15d** to the protofibril **(Figure 4.40a).** In the case of the protofibril-**6e** complex, primary contributors included residues Phe20 (chains A, B, and C), Phe19 (chains A and B), and Ile32 (chain A), while residues Ala21 (chains A and B), Leu34 (chain D), and Asp23 (chain A) showed significant contributions to the binding of **6e** to the protofibril **(Figure 4.40b).** Analysis of the binding free energy from the MD trajectory using the MM-GBSA method indicated efficient interactions of **15d** and **15e** with the protofibrils. Moreover, the per residue decomposition energy highlighted that the majority of critical interacting residues contributing to the final binding energy belonged to chains A and B of the protofibril.

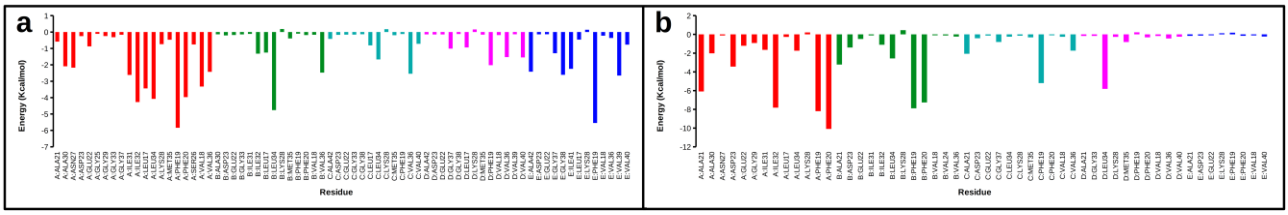

Figure 4.41: Free-energy contribution of critical residues from different chains (highlighted in different colors) of protofibril to (a) **15d** and (b) **15e**.

4.6.12. Evaluation of neuroprotection ability of 15d, 15e, and RIV in AD drosophila model

4.6.12.1. Therapeutic effects of 15d, 15e and RIV on OregonR^{+} and an AD model of drosophila

The successful utilization of biological similarities, referred to as orthologies, between humans and Drosophila has been particularly effective in advancing research on neurodegenerative diseases, with a specific focus on AD (203). The functional components of the brain, namely neurons, exhibit notable similarity to their human counterparts in terms of morphology, synaptic intercommunications, and biochemical signatures. These resemblances

in both function and structure enable fruit fly models of human disease to supplement rodent paradigms across biophysical, molecular biological, neurobiological, and behavioral dimensions (204).

Different concentrations of **15d**, **15e**, and RIV were tested on OregonR+ flies to determine LD_{50}. For **15d,** control at 10 µM, 20 µM, and 40 µM, 100%, 103%, 78%, and 9% flies eclosed, respectively. The 40 µM of **15d** showed high toxicity of 9% flies eclosed. For **15e**, at 10 µM, 20 µM, and 40 µM, 108%, 103%, and 20% flies eclosed, respectively. At 40 µM, **15e** exhibited toxicity with 20 % eclosed flies. **RIV** at 50 µM, 100 µM, 200 µM, and 400 µM showed 108%, 95%,73%, and 29% eclosed flies, respectively (**Figure 4.42I**). The rest of the progenies in each case died at various pupal stages.

In assessing eye phenotypes in $A\beta_{1-42}$ expressing flies, OregonR+ flies on normal food showed 100% normal eyes, while untreated AD flies displayed 40% mild and 60% severe rough eye phenotypes. Administering **15d** at 10 µM and 20 µM to AD flies resulted in 50% mild, 13% severe, 36% rescued, and 36%, 23%, and 40% eye phenotypes. For **15e** at 10 µM, 36% mild, 20% severe, rescue 43%, and at 20 µM, 43% mild, and 16% severe, rescued 40% were observed. RIV at 50 µM showed 43% mild, 23% severe, and 33% rescued, and 100 µM showed 40% mild, 26% severe, and 33% rescued eye phenotypes. Overall, **15d** (20 µM), **6e** (10 and 20 µM), and **RIV** (50 µM) demonstrated the potential to protect against the rough eye phenotype in AD flies (**Figure 4.42II and 4.42III**).

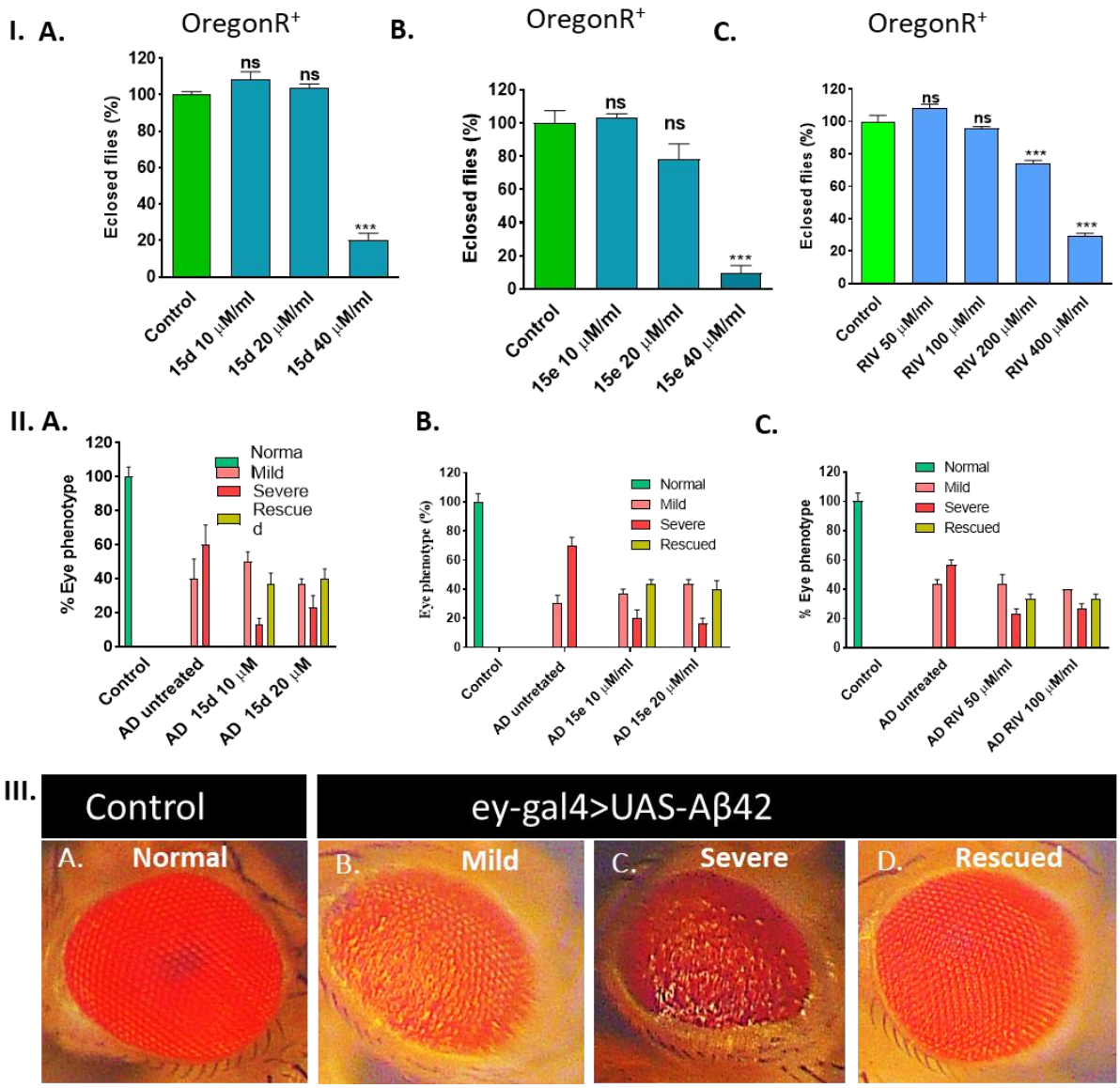

Figure 4.42: Represents the examination of **15d**, **15e**, and **RIV** drugs on OregonR^{+} and AD flies. **I.** Represents the dose determination of **15d**, **15e**, and **RIV** drugs using wild-type flies**.** The One-way ANOVA test is ascribed as significance ***$p<0.0001$, ***$p<0.0001$, $p<0.0001$ **II.** Illustrates the quantitative examination of the eye phenotype of AD flies after administration of **15d**, **15e**, and **RIV** drugs. **III.** Shows the eye phenotype of control and AD flies after administration of the above-mentioned drugs.

4.6.12.2. Evaluation of 15d, 15e, and RIV on the mitochondrial and cellular oxidative stress in the AD drosophila model

Using the MitoSOXTM Red superoxide indicator, untreated AD 3rd instar larval eye imaginal discs exhibited 2-2.5 times higher superoxide levels than the control. Treatment with **15d** at 10 µM and 20 µM normalized superoxide levels, while at 10 µM, a 1.25-fold increase was observed. For **15e**, 10 µM and 20 µM concentrations showed similar superoxide levels to the control. **RIV** at 50 µM reduced superoxide levels closer to the control, while at 100 µM, levels were almost similar to the control. These findings demonstrate the potential of **15d, 15e**, and **RIV** in modulating oxidative stress in AD larval eye imaginal discs **(Figure 4.43).**

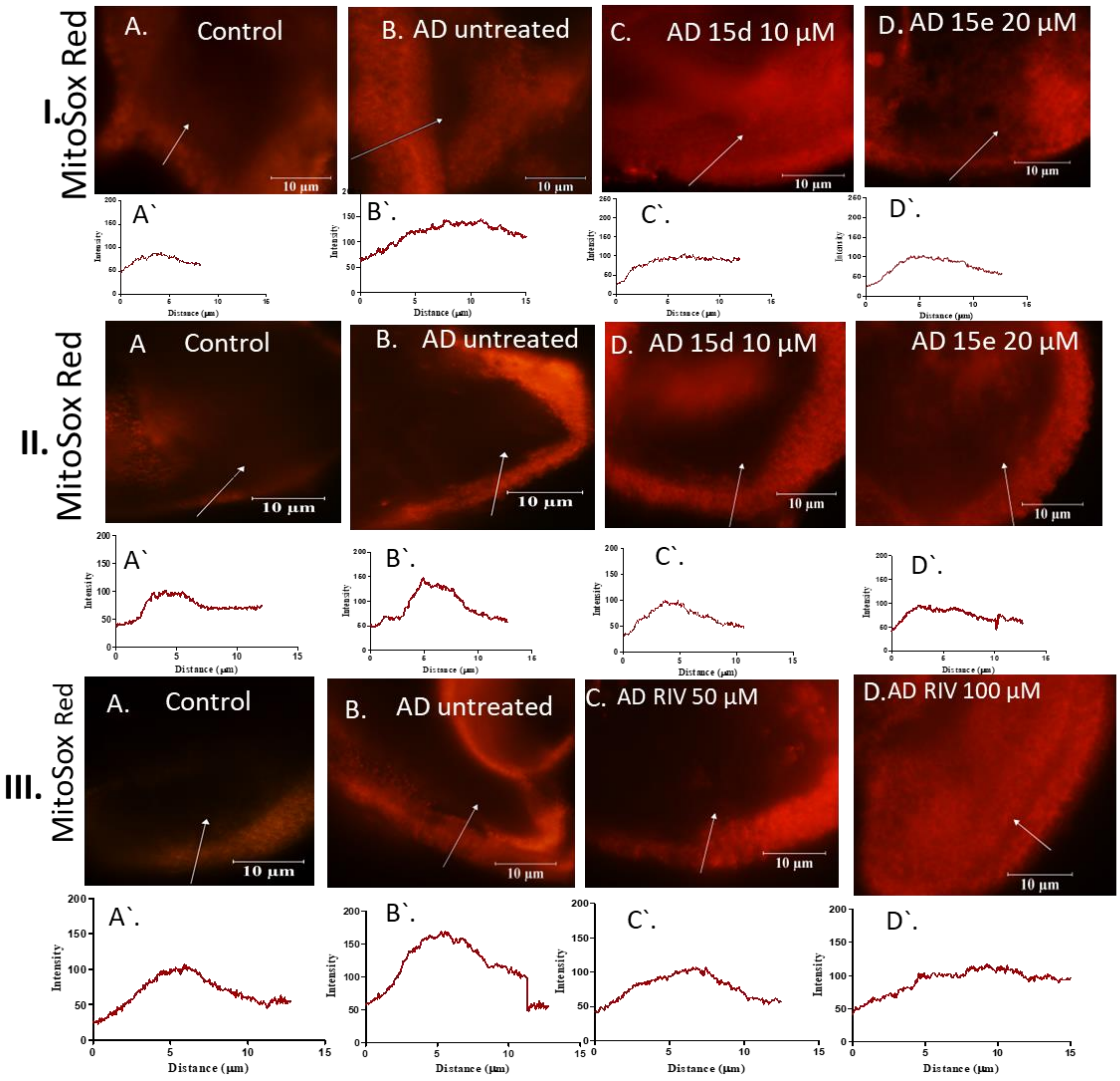

Figure 4.43: Mitochondrial superoxide (ROS) level measurement in Oregon^{+} and $A\beta_{42}$ expressing eye imaginal discs of Drosophila. Fluorescence images of 3rd instar larval eye imaginal discs showing MitoSOX^{TM} Red staining. **I. (A)** Control, **(B)** AD untreated, **(C)** AD treated with **15d** 10 µM, D. **15d** 20 µM, **II.** A. Control, B. AD untreated, **C**. AD treated with **15e** 10 µM, **D. 15e** 20 µM, **III.** A. Control, B. AD untreated, C. AD treated with **RIV** 50 µM, D. **RIV** 100 µM. Respective line graphs showing the MitoSOX^{TM} Red fluorescence intensity in each group's 3rd instar larval eye imaginal disc.

Using H2DCFDA, total cellular ROS levels were examined in OregonR+ and untreated/ treated AD larval eye imaginal discs. Untreated AD larvae showed 4.0 to 4.6-fold higher ROS levels than the control. Treatment with **15d** at 10 µM and 20 µM increased ROS by 1.8-fold, while 1.3-fold exhibited optimal ROS levels. For **15e**, concentrations of 10 µM and 20 µM reduced ROS almost to control levels. **RIV** at 50 µM reduced ROS to control levels, while at 100 µM, levels were 1.5-fold higher. These results suggest that **15d** (10 and 20 µM), **15e** (10 and 20 µM), and **RIV** (50 µM) effectively mitigate oxidative stress in the AD model of Drosophila. Notably, mitochondrial superoxide levels were observed to increase more than cellular ROS levels in AD larval eye imaginal discs. Treatment with **15d, 15e**, and **RIV** significantly reduced oxidative stress in the discs **(Figure 4.44).**

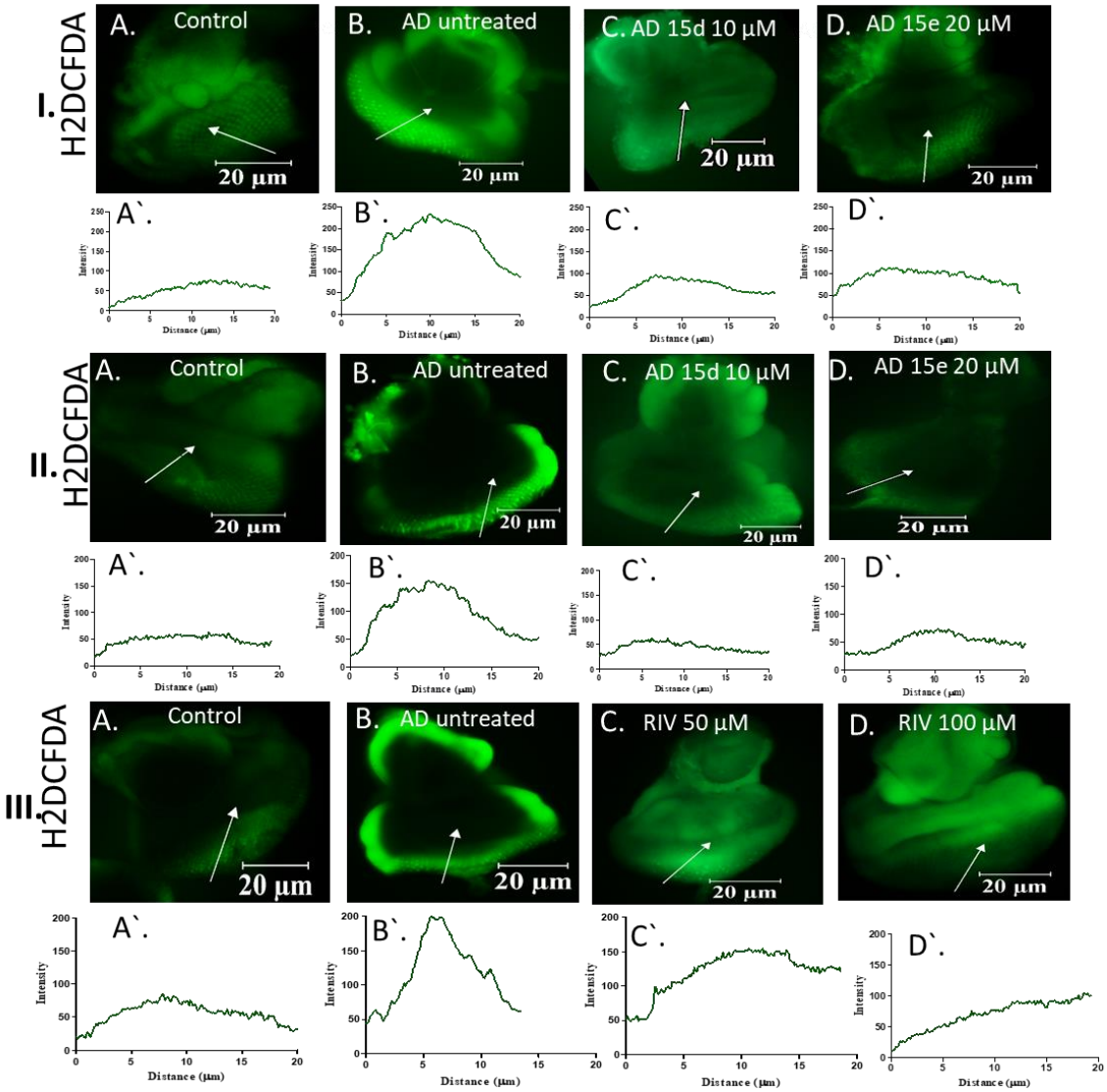

Figure 4.44: Measurement of total cellular ROS level in OregonR^{+} and Aβ_{42} expressing eye imaginal discs of Drosophila. Fluorescence images of 3rd instar larval eye imaginal discs showing H2DCFDA staining. **I.** A. Control, B. AD untreated, C. AD treated with **15d** 10 µM, D. **15d** 20 µM, **II.** A. Control, B. AD untreated, C. AD treated with **15e** 10 µM, D. **15e** 20 µM **III.** A. Control, B. AD untreated, C. AD treated with **RIV** 50 µM, D. **RIV** 100 µM. Respective line graphs show the H2DCFDA fluorescence intensity in each group's 3rd instar larval eye imaginal discs.

4.6.13. Acute toxicity study

The assessment of the safety profile is a crucial aspect in the development of novel drugs. The compounds **15d** and **15e**, identified as potent multifunctional anti-Alzheimer's agents, underwent evaluation in Swiss albino mice at a single dosage of 175 mg/kg, (*per oral*). After a 14-day post-administration, all mice in their respective groups exhibited continued survival without indicating excessive weight gain, abnormal behavior, convulsions, tremors, or diarrhoea, indicative of acute toxicity **(Figure 4.45).**

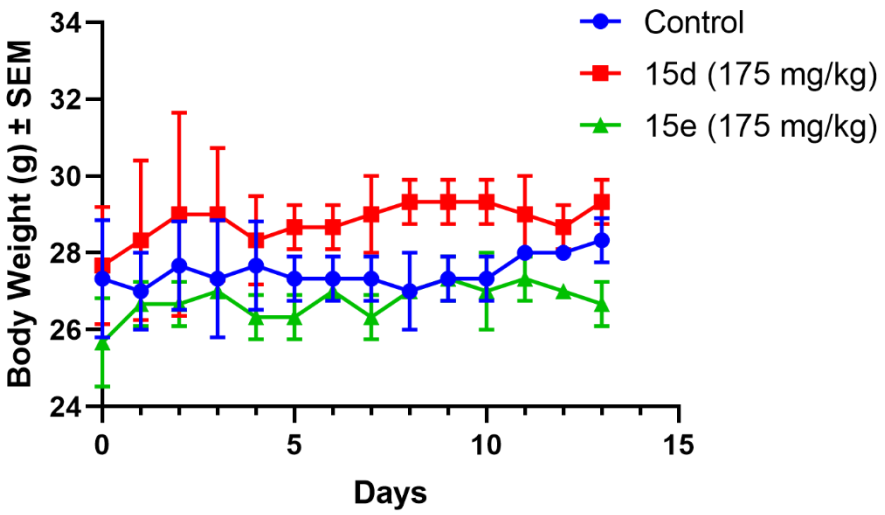

Figure 4.45: The graph represents the average daily body weight of each group of mice over 14 days of drug administration with a dosage of **15d** and **15e** at 175 mg/kg. The data are resented as mean ± SE.

4.6.14. Evaluation of in-vivo efficacy of 15d and 15e in reversing scopolamine-induced cognitive deficits through the Morris water maze test

4.6.14.1. Behavioral measurements

The successful development of a therapeutic agent for AD is expected to greatly improve cognitive function in affected individuals. The MWM experiment is a comprehensive tool for assessing various behavioral changes related to spatial and working memories, cognitive maps, and place learning (205, 206). This test is widely regarded as a

robust gold standard for evaluating compounds' therapeutic potential for treating AD. To further confirm the potential of **15d** and **15e** as promising therapeutic candidates for AD, we investigated their effectiveness in the MWM at 0.3 AD 0.5 mg/kg administered orally (*p.o.*). The Morris water maze test assessed spatial memory and learning in mice with scopolamine-induced dementia. Following ten days of scopolamine treatment, the mice underwent a five-day training period, during which the time taken to reach the platform (escape latency) was recorded and plotted against the training days. The escape latency times for the fifth day are shown in **Figure 4.46A**. It was observed that mice in the disease control group took longer to find the platform than those in the control group. However, mice treated with the test drugs showed a gradual reduction in escape latency over the five-day training period, significantly improving their performance compared to the disease control groups. On the sixth day, the platform was removed, and a probe test was conducted. The amount of time spent in the platform quadrant was measured as an indicator of memory retention **(Figure 4.46B).** The test group animals spent more time in the platform quadrant than the disease control groups, suggesting improved memory retention at doses as low as 0.3 and 0.5 mg/kg compared to RIV at 3 mg/kg.

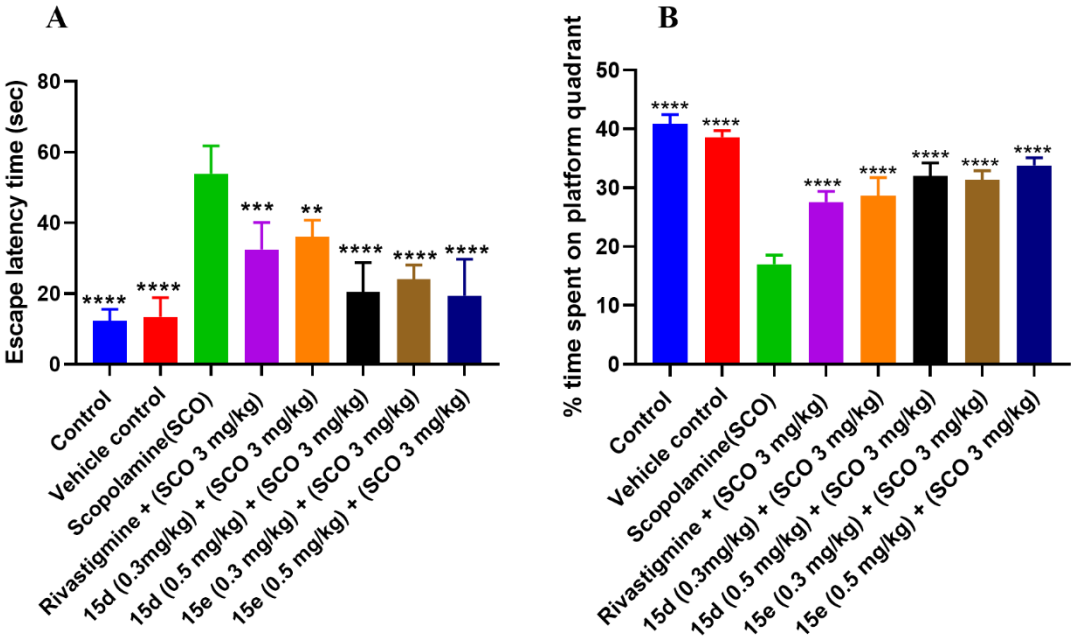

Figure 4.46: Performance of mice in Morris water maze. A. Escape latency of mice in control, disease control, standard control, **15d** and **15e** groups on Day 5 in MWM; B. Probe test on Day 6 in MWM; All data are expressed as the mean ± SEM (n = 5), **** $p < 0.0001$, ***$p < 0.0004$, **$p < 0.0018$ vs. scopolamine. (One-way ANOVA followed by Dunnet's multiple comparison test).

4.6.14.2. Neurochemical profiling and assessment of antioxidant activity

Ex vivo investigations were conducted on the treated subjects to explore the effects of **15d** and **15e** on AChE, BChE, and antioxidant activity. The evaluation of AChE and BChE activity in the brain was done using a modified version of Ellman's colorimetric technique. As depicted in **Figures 4.47A and 4.47B**, the administration of scopolamine significantly elevates the activity of AChE and BChE compared to the control group receiving the vehicle. However, the **RIV**, **6d** and **6e** groups substantially reduced the heightened AChE and BChE activity. These findings suggest that **15d** and **15e** effectively alleviate cholinesterase activity within the brain.

The ex-vivo antioxidant potential of **15d** and **15e** was assessed using various biochemical markers, including superoxide dismutase (SOD), catalase (CAT), and malondialdehyde (MDA). In **Figure 4.47C**, the scopolamine-treated mice exhibited a significant decrease in SOD levels. Intriguingly, **RIV** administration led to a moderate increase in SOD levels. Notably, the administration of lead compounds **15d** and **15e** effectively restored the diminished SOD levels observed in the scopolamine-treated animals. Moreover, significant enhancements in CAT activity within the brain supernatant were evident in the **15d** and **15e** treatment groups (depicted in **Figure 4.47D**), whereas slight changes in the **RIV** treatment groups. Conversely, the levels of MDA showed a corresponding reduction in **15d** and **15e** (shown in **Figure 4.47E**), compared to the scopolamine-treated group. These findings indicate the robust *in-vivo* potential of compounds **15d** and **15e** as ChE inhibitors and agents with antioxidant activities.

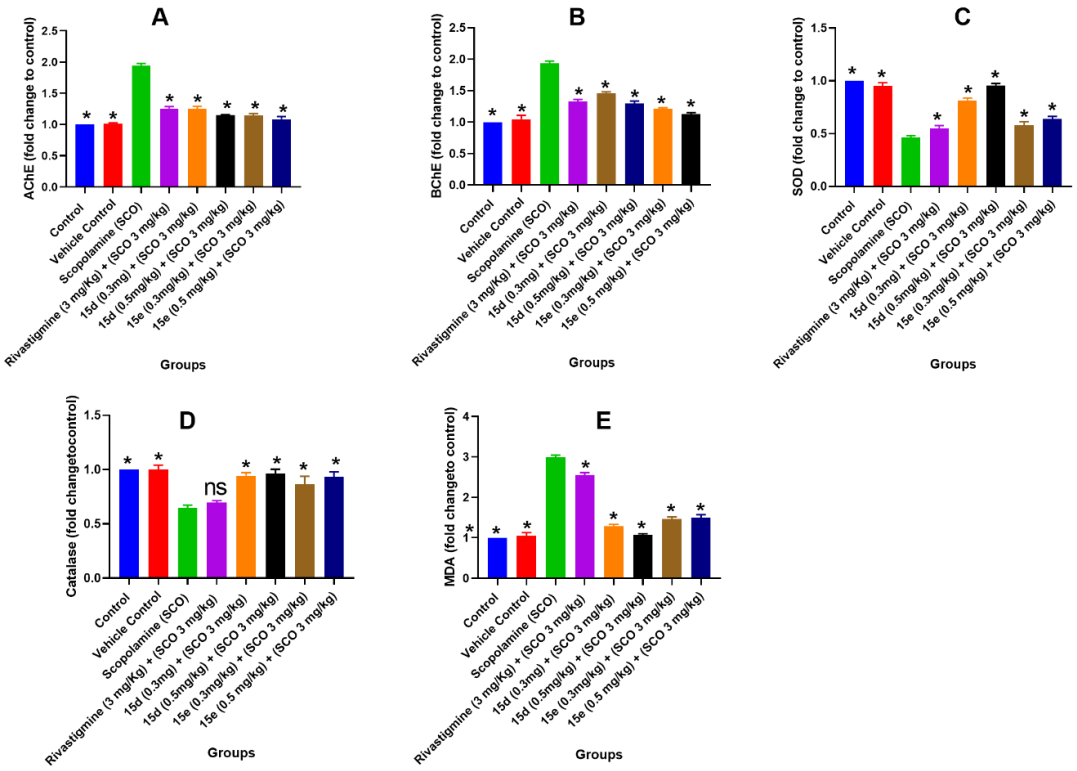

Figure 4.47: Effect of RIV, **15d** and **15e** on various neurochemical parameters such as AChE, BChE, SOD, CAT and MDA. **A) 15d** and **15e** regulate elevated AChE activity, suggesting cholinergic function regulation. **B) 15d** and **15e** significantly reduce BChE activity induced by scopolamine, inhibiting BChE activity. **C) 15d** and **15e** enhances SOD levels, displaying antioxidant effects. **D) 15d** and **15e** reduces MDA levels, mitigating oxidative damage. **E) 15d** and **15e** influences CAT activity, countering oxidative stress. Data are expressed as mean ± SEM (n = 5), *p < 0.0001, ns = nonsignificant vs. scopolamine group (One-way ANOVA followed by Dunnet's multiple comparison test).

4.6.14.3. Evaluation of various markers of neuroprotection through RT-PCR analysis

RT-PCR analysis was performed with the RNA isolated from the hippocampi of the mice. The critical memory markers, such as brain-derived neurotrophic factor (BDNF) and tropomyosin receptor kinase B (TRKB) receptor for BDNF, are essential for neuronal growth and plasticity (207). BDNF is also considered to be important in learning and memory function. BDNF and TRKB gene expression are reduced significantly in the scopolamine-treated mice compared to normal control animals, whereas both genes were upregulated in the treatment groups. CAMP-responsive element binding protein 1 (CREB1), C-FOS, and NR4A2 are essential transcription factors responsible for the formation of synaptic and neurotrophic proteins. CREB1, C-FOS, and NR4A2 levels also declined in the disease group (**Figure 4.48**) but were reversed by the administration of **15d** and **15e**. GAP43 and PSD95 are markers responsible for neuronal growth and plasticity. The treatment drugs have attenuated the decline of plasticity markers in scopolamine-treated animals **(Figure 4.48).** Protein kinase A (PKA) and matrix metalloproteinase 9 (MMP9) are key components of the extracellular matrix that contribute to long-term memory underlying synaptic plasticity. Both

PKA and MMP9 were downregulated in the disease control group, wherein the expression was enhanced by administering **15d** and **15e**.

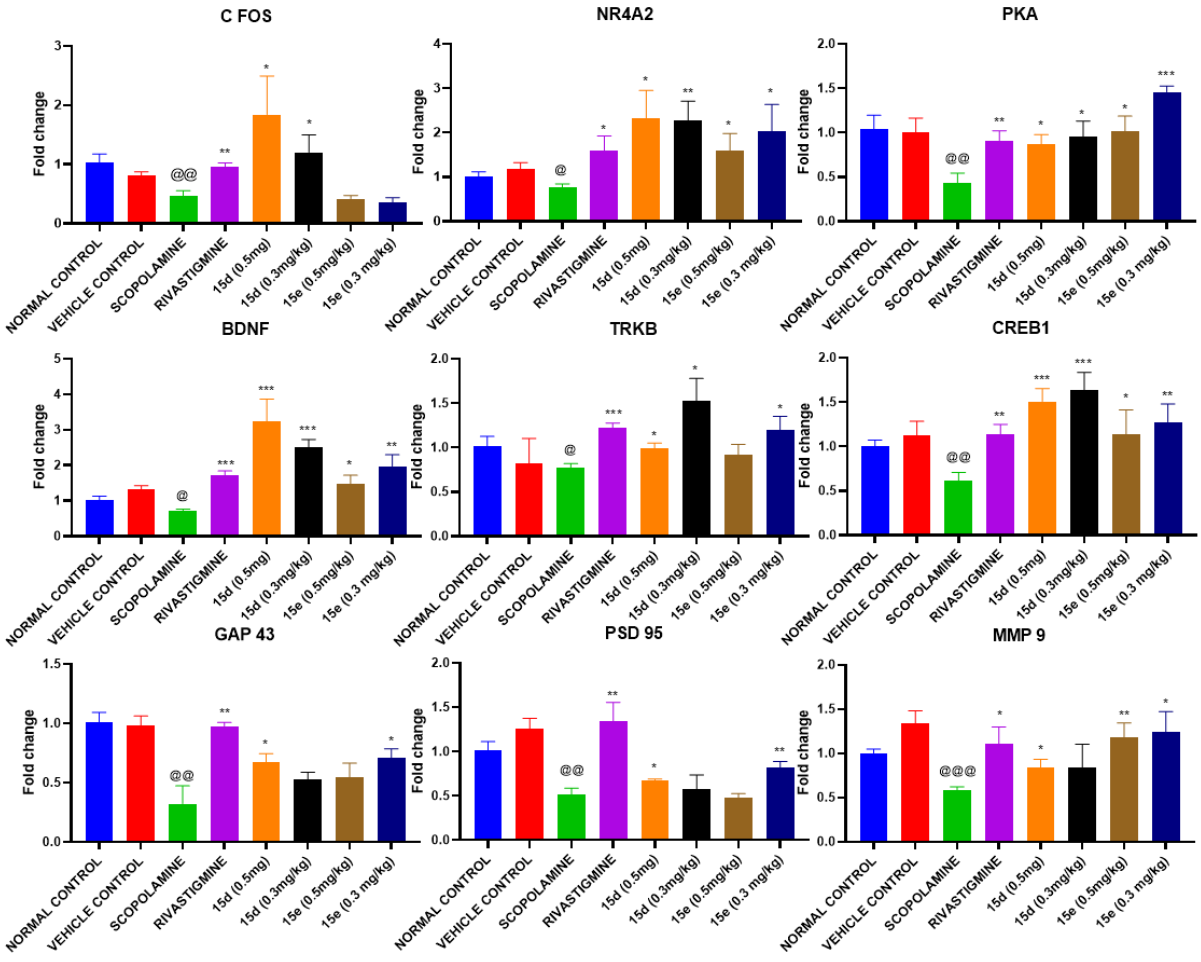

Figure 4.48: RT-PCR analysis of memory markers. Graphs represent fold change in gene expression normalized with GAPDH of mice in different treatment groups: Normal control, vehicle control, scopolamine, RIV, **15e** 0.5 mg, **15e** 0.3 mg, **15d** 0.5 mg, **15d** 0.3 mg. Results are shown as mean ± SEM (n=5). Comparisons between groups were made using a student's T-test. P value < 0.05 is considered statistically significant. *p < 0.05, 0.01 ≥**p ≥ 0.001, ***p < 0.001. @ Normal control Vs Scopolamine. * Scopolamine Vs RIV, **15e** 0.5 mg, **15e** 0.3 mg, **15d** 0.5 mg, **15d** 0.3 mg.

4.6.15. ADMET Prediction

Assessing the absorption, distribution, metabolism, excretion, and toxicity (ADMET) properties is essential to the initial screening phase when developing novel drug candidates for different diseases, including AD. To assess the ADMET properties of the synthesized derivatives, an in-silico screening was performed using the admetSAR tool, and the findings are presented in **Table 16**. The in silico ADMET properties of two established AChE inhibitors, DPZ and RIV, were also evaluated to validate the accuracy of the ADMET prediction protocol. All synthesized compounds met the criteria outlined by Lipinski's rule of five, which suggests favorable drug-like properties. These criteria include a molecular weight (MW) below 500, a limited number of hydrogen bond donors (HB donors) and acceptors (HB acceptors), a logarithm of the partition coefficient (log P) below 5, and a restricted number of rotatable bonds. Furthermore, the permeability study revealed that most tested compounds, including **15d, 15e,** and RIV, could cross the blood-brain barrier (BBB).

Table 16. Physical properties and ADMET prediction of the compounds

Comp.	**Mol.Wt** †	**ClogP***	**TPSA**[1]	**HBA**[2]	**HBD**[3]	**RBs**[4]	Caco-2[-]	BBB[+]
15d	385.89	4.32	53.6	3	2	6	-	+
15e	367.45	2.77	73.83	4	3	6	-	+
Riv	250.34	2.09	32.78	3	0	4	+	+

All values were calculated using online software **admetSAR** except TPSA & ClogP (ChemDraw). † Daltons, *Calculated logarithm of the octanol-water partition coefficient, [1] Topological polar surface area, [2]Hydrogen-bond acceptor, [3]Hydrogen-bond donor, [4]Rotatable bonds, [-]Caco-2 Permeability, [+]Blood-Brain Barrier.